Core-collapse supernovae: reduced nuclear networks and equations of state

Kernkollaps-Supernovae: reduzierte Kernnetzwerke und Zustandsgleichungen
Zur Erlangung des Grades eines Doktors der Naturwissenschaften (Dr. rer. nat.)
Genehmigte Dissertation von Gerard Navó Perez aus El Masnou, Spain
Tag der Einreichung: 16. Oktober 2023, Tag der Prüfung: 6. November 2023

1. Gutachten: Prof. Dr. Almudena Arcones
2. Gutachten: Prof. Dr. Miguel Ángel Aloy
Darmstadt, Technische Universität Darmstadt

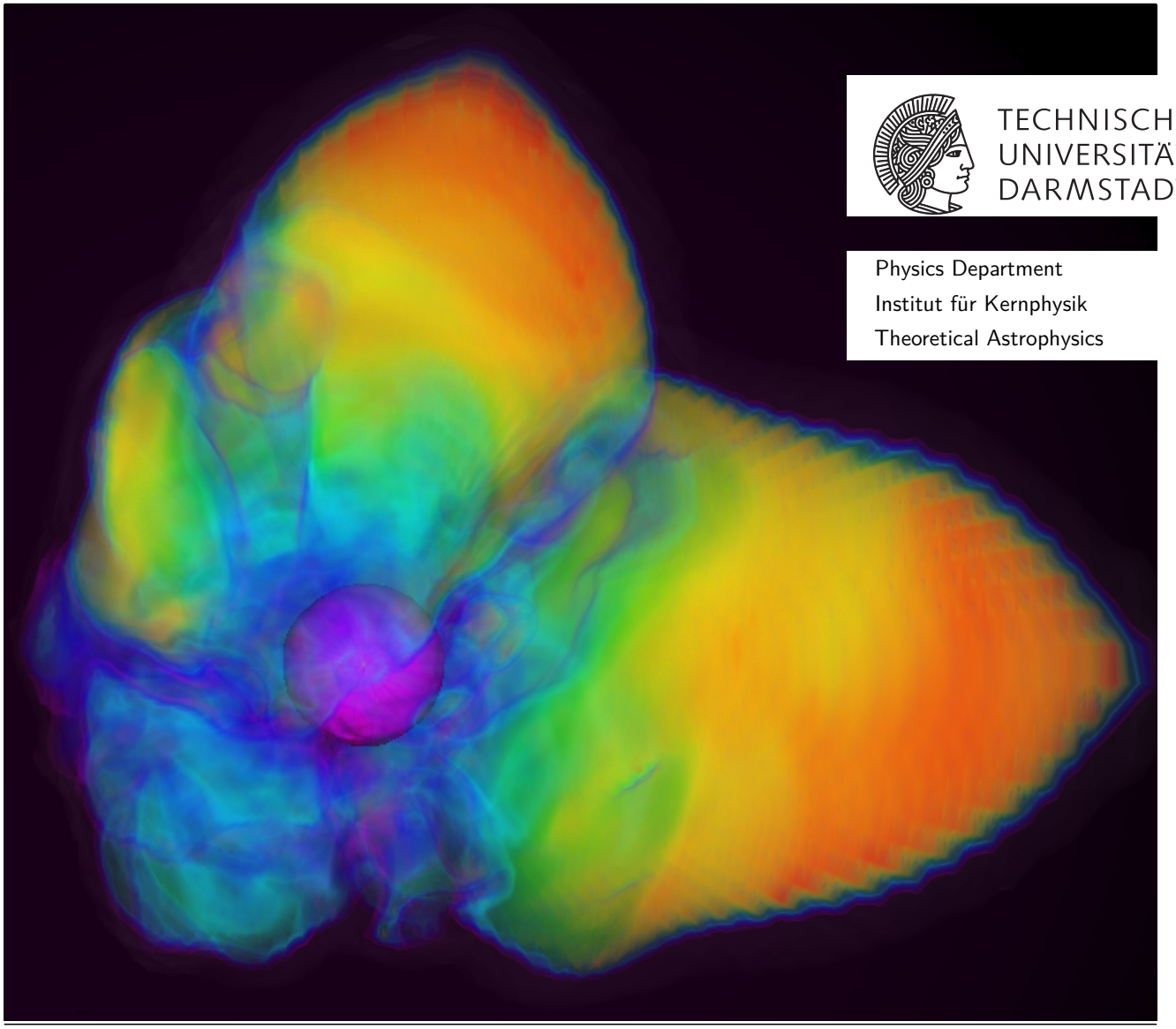

TECHNISCHE UNIVERSITÄT DARMSTADT

Physics Department
Institut für Kernphysik
Theoretical Astrophysics

Core-collapse supernovae: reduced nuclear networks and equations of state
Kernkollaps-Supernovae: reduzierte Kernnetzwerke und Zustandsgleichungen

Accepted doctoral thesis by Gerard Navó Perez

Date of submission: 16. Oktober 2023
Date of thesis defense: 6. November 2023

Darmstadt, Technische Universität Darmstadt

Bitte zitieren Sie dieses Dokument als:
URN: urn:nbn:de:tuda-tuprints-276871
URL: http://tuprints.ulb.tu-darmstadt.de/27687
Jahr der Veröffentlichung auf TUprints: 2024

Dieses Dokument wird bereitgestellt von tuprints,
E-Publishing-Service der TU Darmstadt
http://tuprints.ulb.tu-darmstadt.de
tuprints@ulb.tu-darmstadt.de

Als meus pares Marià i Antonia

Abstract

Massive stars end their life in violent explosive events that are triggered by the collapse of the iron core, the so-called core-collapse supernovae (CCSNe). CCSNe host a large variety of thermodynamic conditions, from cold low-density regions in the external layers of the collapsing star to the hot and very dense nascent proto-neutron star (PNS). Nuclear physics is a key ingredient to determine the evolution of CCSNe. At high densities, the strong interaction governs the equation of state (EOS), which has large impact on the dynamics. Nevertheless, the EOS of dense matter is not fully understood. Numerical simulations are crucial to understand, and explore, the mechanisms involved in the explosion. Thus, we use CCSNe simulations as laboratories to study the impact of several nuclear matter properties on the dynamics of the PNS and the explosion. At low densities, nuclear reactions describe the nucleosynthesis that takes place in the events, which play an essential role in the chemical evolution of the universe. Unfortunately, CCSN simulations are very computationally expensive and, therefore, they need to employ approximations. At low densities, they often consider a very simplified nuclear composition.

In the first part of the thesis, we investigate the impact of the composition and the energy released by nuclear reactions at low temperatures. We implement two reduced nuclear reactions networks and study their impact in the simulation. The largest evolves the main species synthesized during the explosion. We perform one- and two-dimensional simulations where we test the networks and study the effects on the dynamics of the explosion and the nucleosynthesis. We find that sufficiently large reduced nuclear networks are necessary for more accurate feedback of the nuclear energy generation, neutrino absorption, and nucleosynthesis.

In the second part of the thesis, we study the effects of nuclear matter properties in CCSNe. We perform one-dimensional models using several EOSs that systematically vary the slope parameter, symmetry energy, incompressibility, and the density exponent of the energy density functional. We find that a higher slope parameter produces a slower PNS contraction, a less energetic shock, and a less compact remnant. In addition, our results suggest that a low incompressibilty causes a faster collapse, much higher central densities at bounce, and is less likely to revive the shock.

Finally, we show the early evolution stage of a state-of-the-art 3D CCSN simulation including a reduced nuclear reaction network, that will become a benchmark for future sytematic studies in one and two dimensions. We describe its main characteristics and conclude that it will produce a successful explosion.

Zusammenfassung

Massereiche Sterne beenden ihr Leben in gewaltigen explosiven Ereignissen, die durch den Kollaps des Eisenkerns ausgelöst werden, den so genannten Kernkollaps-Supernovae (CCSNe). CCSNe weisen eine große Vielfalt an thermodynamischen Bedingungen auf, von kalten Regionen mit geringer Dichte in den äußeren Schichten des kollabierenden Sterns bis hin zum heißen und sehr dichten entstehenden Proto-Neutronenstern (PNS). Die Kernphysik ist ein Schlüsselelement zur Bestimmung der Entwicklung von CCSNe. Bei hohen Dichten bestimmt die starke Wechselwirkung die Zustandsgleichung (EOS), die einen großen Einfluss auf die Dynamik hat. Dennoch ist die EOS von dichter Materie nicht vollständig verstanden. Numerische Simulationen sind entscheidend für das Verständnis und die Erforschung der an der Explosion beteiligten Mechanismen. Daher verwenden wir CCSNe-Simulationen als Laboratorien, um die Auswirkungen verschiedener Kernmaterieeigenschaften auf die Dynamik des PNS und der Explosion zu untersuchen. Bei niedrigen Dichten beschreiben Kernreaktionen die Nukleosynthese, die in den Ereignissen stattfindet und die eine wesentliche Rolle bei der chemischen Entwicklung des Universums spielt. Leider sind CCSN-Simulationen sehr rechenintensiv, weshalb sie auf Näherungen zurückgreifen müssen. Bei niedrigen Dichten gehen sie oft von einer sehr vereinfachten Kernzusammensetzung aus.

Im ersten Teil der Arbeit untersuchen wir die Auswirkungen der Zusammensetzung und der durch Kernreaktionen bei niedrigen Temperaturen freigesetzten Energie. Wir implementieren zwei reduzierte Kernreaktionsnetzwerke und untersuchen ihre Auswirkungen in der Simulation. Das größte entwickelt die wichtigsten nuklearen Spezies, die während der Explosion synthetisiert werden. Wir führen ein- und zweidimensionale Simulationen durch, in denen wir die Netzwerke testen und die Auswirkungen auf die Dynamik der Explosion und die Nukleosynthese untersuchen. Wir stellen fest, dass ausreichend große reduzierte Kernnetzwerke für eine genauere Rückkopplung der Kernenergieerzeugung, der Neutrinoabsorption und der Nukleosynthese erforderlich sind.

Im zweiten Teil der Arbeit untersuchen wir die Auswirkungen der Eigenschaften der Kernmaterie in CCSNe. Wir führen eindimensionale Modelle mit verschiedenen EOS durch, die systematisch den Steigungsparameter, die Symmetrieenergie, die Inkompressibilität und den Dichteexponenten des Energiedichtefunktionals variieren. Wir stellen fest, dass ein höherer Steigungsparameter eine langsamere PNS-Kontraktion, einen weniger energiereichen Schock und einen weniger kompakten Überrest erzeugt.

Darüber hinaus deuten unsere Ergebnisse darauf hin, dass eine niedrige Inkompressibilität einen schnelleren Kollaps, viel höhere zentrale Dichten beim Kollaps und eine geringere Wahrscheinlichkeit der Wiederbelebung des Schocks verursacht.

Schließlich zeigen wir das frühe Entwicklungsstadium einer hochmodernen 3D-CCSN-Simulation mit einem reduzierten Kernreaktionsnetzwerk, das als Maßstab für zukünftige sytematische Studien in einer und zwei Dimensionen dienen wird. Wir beschreiben die Hauptmerkmale dieser Simulation und kommen zu dem Schluss, dass sie eine erfolgreiche Explosion hervorbringen wird.

Contents

List of Figures

List of Tables

1 Introduction

The concept nova comes from Latin and was coined by the astronomer Tycho Brahe in the sixteenth century when a supposedly new star appeared in the sky. However, it was not until 1931 when Walter Baade and Fritz Zwicky came up with the term *Supernova* (SN) during their lectures (Baade & Zwicky, 1934), in order to distinguish especially bright transients and differentiate them from fainter novae. As many other topics in science, SNe aroused the interest of scientist from ancient civilizations with the first observations at naked eye. Nevertheless, it has not been until more recent days, with the development of new physics and techniques, that we started to draw a more complete picture of SNe beyond they being bright transients that appear in our sky.

The first confirmed record of a SN date back from the year 185 CE. A group of Chinese astronomers observed a very bright star appeared in the sky that was visible eight months at naked eye (e.g., Clark & Stephenson, 1982). The brightest SN event ever recorded took place in the year 1006 CE, which was recorded by astronomers from across Asia and Europe (Murdin & Murdin, 1985). They noted that its brightness was one-quarter the brightness of the Moon. In 1573, Tycho Brahe published his observations and showed that SNe were stationary, i.e., they had a constant parallax, and, therefore, were formed far beyond the Moon. This was a very important breakthrough since it was against the Aristotelian tradition, which thought that the celestial vault was invariant, and, therefore, that SN were produced somehow in the atmosphere. Later, the invention of the telescope increased the number of observations since it made possible the detection of SNe from other galaxies. However, it has been more than 300 years without directly detecting an event taking place in the Milky Way. Despite this, there are evidences that Cassiopea A was actually the remnant of an explosion that was probably not noticed due to the high amount of dust (e.g., Fabian et al., 1980). Currently, it is the brightest radio source beyond the solar system (see Figure 1.1).

More recently, in the early 1930s, Walter Baade and Fritz Zwicky postulated that the SN were the result of an explosion triggered by the gravitational collapse of ordinary stars (Baade & Zwicky, 1934). Nowadays, we know this sub-type of SN as the so-called core-collapse SN (CCSN). In addition, after the discovery of the neutron (Chadwick, 1932), they suggested neutron stars (NS) to be the remnants of such events. With Burbidge et al. (1957), the community focused in the origin of the elements in the universe. The fusion in stars produce species up to the iron group,

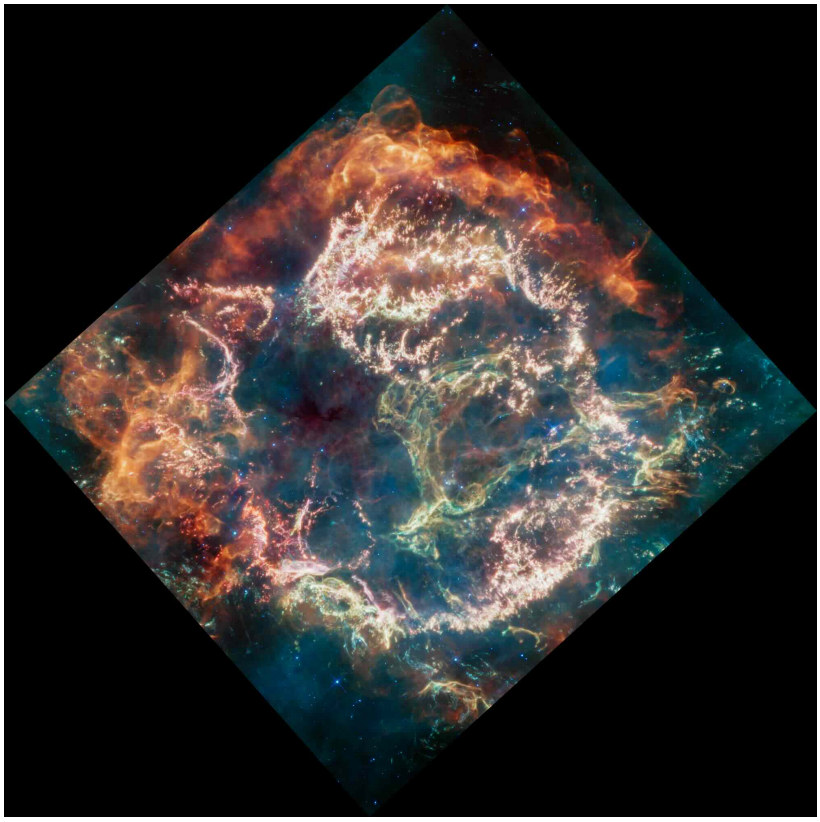

Figure 1.1: Mid-infrared image of Cassiopea A obtained with the James Webb Telescope (NASA et al., 2023).

where the binding energy per particle is minimum. Thus, heavier elements cannot be produced in stars, and CCSNe were postulated as possible candidates to host heavier element nucleosynthesis and became a hot topic.

In order to study the nucleosynthesis that takes place in CCSNe, it is key first to understand the mechanisms involved in the explosion. Thus, the first hydrodynamic simulations were performed in the 1960s considering spherical symmetry (Colgate & Johnson, 1960; Colgate et al., 1961). They observed that after the collapse of the core, in a timescale of less than a second, nuclear densities are reached and a shock wave was produced that started to propagate outwards. However, the shock was losing part of its energy and eventually stalled, failing to produce an explosion. Years later, Bethe & Wilson (1985a) postulated the neutrino-delayed mechanism based on Colgate & White (1966), where they introduced the idea that the neutrinos deposit the missing energy to the shock to revive. The observation of the SN1987A event provided evidences that neutrinos were playing a key role to revive the explosion

(e.g., see review Arnett et al., 1989). In addition, it unveiled that the explosion was not spherically symmetric, which led to the first multi-dimensional simulations (e.g., Herant et al., 1994; Burrows et al., 1995; Janka & Mueller, 1995). They shed light into the explosion mechanism, showing that multidimensional effects like, e.g., convection and hydrodynamic instabilities, are key for the shock expansion.

Over the years, simulations have become more reliable with the inclusion of new developments from theory, experiments, and observations. However, the puzzle is far from being completed due to the large amount of ingredients (i.e., physics) involved. Some of them are, e.g., neutrino transport (e.g., Mezzacappa et al., 2020a), general relativistic gravity treatment (e.g., Kuroda et al., 2012), multidimensionality (e.g., Burrows et al., 2020), or nuclear physics inputs such the equation of state (EOS) of dense matter (e.g., Yasin et al., 2020). In this thesis, we perform state-of-the-art simulations of the first $1.5 - 2\,\mathrm{s}$ of evolution, which are the key for the engine to set the explosion. We focus on two different density and temperature regimes in the simulation. At low temperatures and densities, we investigate the treatment of nuclear reactions and composition. At high densities, we study the impact of different nuclear matter properties.

One of the aims of this work is to show the impact nuclear reactions have on the dynamics of the explosion and its nucleosynthesis. To do so, we first improve the treatment of the composition in the state-of-the-art Aenus-Alcar code (Just et al., 2015; Obergaulinger & Aloy, 2017) at low temperatures by implementing a nuclear reaction network to track the species within the hydrodynamic simulation. We show the results from a total of 16 one- and two-dimensional models. In addition, we explore the first milliseconds of evolution of a 3D simulation with this new feature.

CCSNe are considered laboratories where we can perform experiments at conditions that are not reproducible in the Earth. In this thesis, we explore the impact of different nuclear matter properties on the explosion mechanism and its remnant. We carried out the study employing new EOSs of dense matter that consider up-to-date nuclear physics constraints (Huth et al., 2021).

This thesis is structured as follows. In Chapter 2, we begin with the theoretical overview of CCSNe . In Chapter 3, we introduce the simulation framework in which we perform our study. We explain the implementation of the reduced network module in Aenus-Alcar in Chapter 4, and study the effect of the composition treatment in Chapter 5. In Chapter 6, we show the impact of different nuclear matter properties in the explosion. Finally, we show the first stages of evolution of the state-of-the-art 3D model in Chapter 7.

2 Core-collapse supernovae

Massive stars ($M \gtrsim 8\,\mathrm{M}_\odot$) usually end their life in core-collapse supernovae (CCSN), explosive events that are triggered by the collapse of the iron core. They release several solar masses of products synthesized during the stellar evolution and the explosion itself into the interstellar medium (ISM). Thus, they play a critical role in the chemical history of the universe and have been matter of study for many decades.

In order to investigate the mechanisms involved, radiation-hydrodynamic simulations have been performed, following different evolutionary stages from collapse to shock breakout. In addition, observations have helped to constrain the characteristics of the stellar evolution prior the explosion, the explosion itself, as well as its remnants. However, the whole puzzle is still far from being completed.

In this section, we introduce the main mechanisms involved from the late stellar evolution stages to the remnant of the explosion, following Burrows (1990); Carroll & Ostlie (2007); Janka et al. (2007); Janka (2012, 2017); Müller (2020); Burrows & Vartanyan (2021).

2.1 Final stage of a massive star

The fate of stars depends on how massive they are. They spend most of their lives burning hydrogen, on the so-called main sequence. At this stage, stars are in hydrostatic equilibrium, where the gas thermal pressure is in balance with the gravitational pull. In the main sequence, massive stars burn the hydrogen into helium in convective cores through the CNO cycle, which employs carbon, nitrogen, and oxygen as catalysts.

After $\sim 10\,\mathrm{Myr}$, the hydrogen fuel in the core is near to be consumed[1]. However, the core is not hot enough for helium to ignite ($T \sim 0.03\,\mathrm{GK}$). Therefore, the rate at which nuclear energy is released decreases and the hydrostatic equilibrium is temporarily broken. This leads the total energy of the star to decrease as well, since energy is being emitted from the surface. The gravitational energy becomes more negative and the star contracts. In addition, from the virial theorem, half of the gravitational energy variation is transformed into thermal energy, i.e. an increase in temperature. The contraction halts when the temperature is high enough for helium burning ($T \sim 0.2\,\mathrm{GK}$).

[1]The precise value depends on the mass the star has at the beginning of the main sequence.

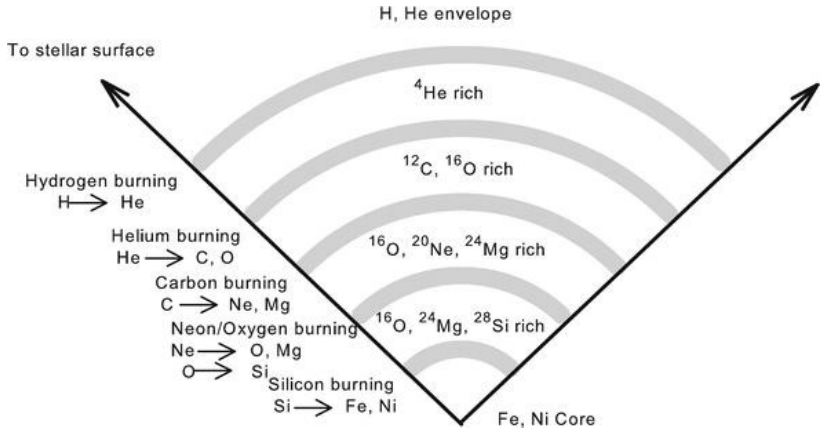

Figure 2.1: Schematic view of the onion-like structure of a massive star at the end of its life. In the left, an illustrative diagram showing the burning reactants and products at each shell. Figure from Peters & Hirschi (2013)

The accumulated helium in the core burns into carbon and oxygen, mostly via triple-α reactions. The helium core is surrounded by a hydrogen-burning envelope. Each burning sequence is preceded and followed by a contraction of the core, which further increases the temperature. When the next core burning starts, the contraction ceases because of the new source of energy. In addition, the time scale shortens progressively, since the energy per baryon released by the nuclear reactions decreases when approaching the iron peak. After $\sim 1\,\mathrm{Myr}$, the helium core is exhausted. Subsequently, when the temperatures reach $T \sim 0.8\,\mathrm{GK}$, the core ignites carbon burning, leading within $\sim 2000\,\mathrm{yr}$ to an oxygen-neon core. This ongoing sequence of nuclear reactions produce an onion-layered shell of elements that undergo fusion (see Figure 2.1). Finally, at temperatures of $T \sim 3 \cdot 10^9\,\mathrm{K}$, silicon burning produces an iron-group core, with species such $^{54}\mathrm{Fe}$, $^{56}\mathrm{Fe}$, and $^{56}\mathrm{Ni}$. This takes place in a timescale of several days.

At this point, nuclear reactions are not efficient anymore because the maximum binding energy per baryon is reached. Hence, the core grows by accumulating the adjacent iron-group products of the silicon burning taking place in the surrounding layer. Meanwhile, in absence of burning in the core, the hydrostatic equilibrium is maintained thanks to the electron degeneracy pressure. When the core reaches the Chandrasekhar limit, $M_{\mathrm{ch}} \sim 1.45\,\mathrm{M}_\odot$, the degeneracy pressure of electrons cannot hold the gravitational pull and collapses.

2.2 Collapse, bounce, and shock formation

When the core of a massive star reaches M_{Ch}, the degeneracy pressure of electrons cannot keep the hydrodynamic balance with gravity. At this point, the matter collapses supersonically. The densities progressively increase, which causes the electrons to reach higher Fermi energies. Because of this, electron captures by nuclei and protons become important and make the matter more neutron rich,

$$e^- + (A, Z+1) \rightarrow \nu_e + (A, Z), \tag{2.1}$$

$$e^- + p \rightarrow \nu_e + n. \tag{2.2}$$

The neutrinos released stream off freely and carry away a significant amount of energy from the collapsing star, which accelerates the contraction (left panel of Figure 2.2). Furthermore, this neutrino loss leads to a decrease of the total lepton number of the system, the so-called deleptonization.

It also reduces the electron fraction, defined as the electron to baryons ratio[2]:

$$Y_e \equiv \frac{n_e}{n_{\mathrm{p}} + n_{\mathrm{n}}} = \frac{n_{\mathrm{p}}}{n_{\mathrm{p}} + n_{\mathrm{n}}}, \tag{2.3}$$

where n_e, n_{p}, and n_{n} are the number densities of electrons, protons, and neutrons present in the matter. Electron capture decreases the degeneracy pressure and, together with photodisintegrations and β-decays in the Fe-group, results in an acceleration of the collapse. The further collapse contracts the core to several hundreds of kilometers within less than half a second. As a consequence, the density and temperature in the center keep increasing. At densities of $\rho \sim 10^{12}\,\mathrm{g\,cm^{-3}}$, neutrinos cannot escape anymore because of coherent scattering on nuclei,

$$\nu + (A, Z) \rightarrow \nu + (A, Z). \tag{2.4}$$

The time between collisions with matter decreases below the time of the infall and, therefore, neutrinos get trapped, stopping the deleptonization. At this point, the collapse becomes homologous, i.e., the velocity increases linearly with radius (see right panel of Figure 2.2 for a schematic representation).

Eventually, the contracting core reaches nuclear saturation density, $\rho_0 \sim 10^{14}\,\mathrm{g\,cm^{-3}}$, at which there is a phase transition from inhomogenous (nucleons, alphas, and nuclei) to homogenous (pure nucleons) nuclear matter. This increases the pressure drastically and consequently, reduces the infall velocity of the homologous core. Nucleons are so densely packed that the strong interaction, repulsive in short-range, halts the collapse in the so-called bounce. At this point, a sound wave is formed (shock) surrounding the homologous core. Meanwhile, matter is still supersonically infalling into it. In the center, the proto-neutron star (PNS) starts to form (left panel of Figure 2.3).

[2] it can interchangeably be defined as the ratio of protons to baryons because of charge neutrality

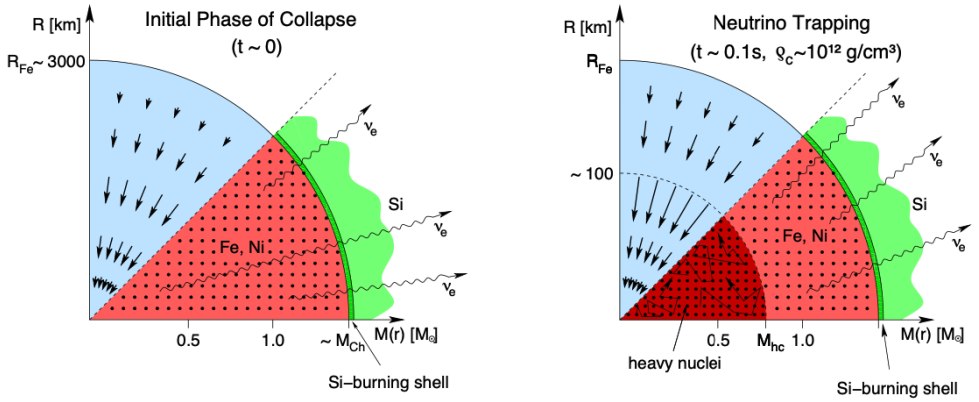

Figure 2.2: Schematic representation of the collapsing phases in a CCSN. Vertical axis depicts radial distance and horizontal axis mass coordinate. The upper half of the panels show the dynamic conditions. Arrows represent the velocity field. The lower half show the nuclear processes involved. Figures 2.3 and 2.4 follow the same schematic representation at later times. Figure adapted from Janka et al. (2007)

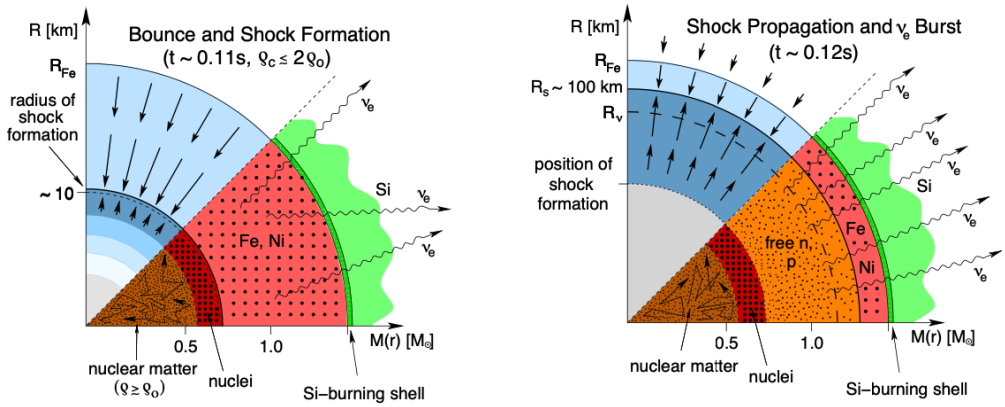

Figure 2.3: Schematic representation of the bounce, the shock formation and propagation, and the neutrino burst. Figure adapted from Janka et al. (2007)

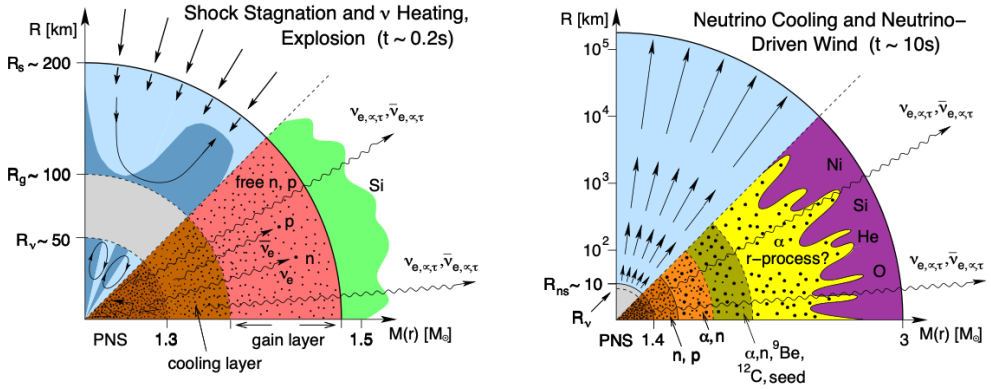

Figure 2.4: The left panel shows an schematic representation of dynamical and nuclear processes when the shock is stalled. The right panel depicts the processes when the explosion is already triggered. Figure obtained from Janka et al. (2007)

2.3 Neutrino-driven delayed explosion

After the bounce, the freshly formed shock starts to propagates outwards. It loses part of its energy dissociating the nuclei, from the outer infalling layers, into free neutrons and protons. In addition, in a timescale of several milliseconds, electron captures by free protons produce a vast amount of neutrinos. When the shock breaks out off the neutrinosphere (R_ν, the radius at which neutrinos are able to stream away), these thermally decouple and are set free in the so-called neutrino burst (see right panel of Figure 2.3), with very high luminosities $L_\nu \sim 10^{53}\,\mathrm{erg\,s^{-1}}$. As pointed out previously, this reduces the Y_e as a result of the high neutrino emission. The shock eventually loses enough energy to prevent it from propagating further and stagnates at radius $R \sim 200\,\mathrm{km}$ (see left panel of Figure 2.4).

Meanwhile, the PNS keeps accreting the surrounding material and contracting to $R_{\mathrm{PNS}} \sim 50\,\mathrm{km}$. The inner part of the PNS has densities beyond ρ_0. As mentioned above, at such densities neutrinos are trapped since their mean free path is smaller than the radius of the PNS. On the other hand, the PNS mantle has lower densities ($\sim 10^{11}\,\mathrm{g\,cm^{-3}}$) and is rich in free nucleons from the nuclei dissociated by the shock. While it shrinks, part of its internal energy is radiated via neutrinos. It cools mainly through electron captures on free nucleons (Equation (2.2)), as well as pair processes,

$$e^- + e^+ \rightarrow \nu + \bar{\nu}. \tag{2.5}$$

The radiated neutrinos carry away energy from the PNS and cool it down. As shown in the left panel of Figure 2.4, at this point the neutrinosphere is located close to the PNS surface. In addition, the neutrino emission leads to lepton number gradients in

the PNS mantle, causing convection.

Since neutrinos have small cross-sections, they barely interact with baryonic matter, i.e., outside the PNS at low densities. However, part of the neutrinos emitted by the PNS ($1\,\%$) are absorbed by free nucleons,

$$\nu_e + n \rightarrow e^- + p, \tag{2.6}$$

$$\bar{\nu}_e + p \rightarrow e^+ + n, \tag{2.7}$$

behind the shock, in the so-called gain region, which inner boundary is defined as the gain radius ($R_{\rm g}$). The energy deposited, $\sim 10^{50} - 10^{51}\,{\rm erg\,s^{-1}}$, increases the pressure in the gain region and eventually causes the shock to revive. This is the so-called delayed neutrino-heating mechanism, first proposed by Bethe & Wilson (1985b) and based on the idea that neutrinos should provide energy for the explosion, suggested by Colgate & White (1966).

The successful revival of the shock depends on competition between the neutrino heating and advection timescales in the gain layer (e.g., Burrows & Goshy, 1993). The former is defined as the time that it takes neutrinos to unbind the matter in the gain region,

$$t_{\rm heat} = \frac{|E_{\rm tot}^{\rm gain}|}{Q_\nu^{\rm gain}}, \tag{2.8}$$

where $E_{\rm tot}^{\rm gain}$ is the total energy, (i.e., including gravitational, internal, and kinetic) and $Q_\nu^{\rm gain}$ the net neutrino energy deposition in the gain layer. The advection timescale is defined as the time that takes the flow to accrete from $R_{\rm shock}$ to $R_{\rm g}$,

$$t_{\rm adv} \sim \frac{M_{\rm gain}}{\dot{M}}, \tag{2.9}$$

where $M_{\rm gain}$ is the mass encompassed in the gain region and $\dot{M}$ is the accretion rate through the shock. The necessary, but not sufficient, condition for the shock to revive is that the heating timescale is shorter than the advection one, i.e., $t_{\rm heat} < t_{\rm adv}$. Otherwise, the shock is not revived and the core eventually collapses to a black hole (BH) (see Section 2.5). In addition, due to the neutrino heating, the gain region develops profiles that are unstable against non-radial flows such convection, the standing accretion shock instability (SASI) (e.g., Blondin et al., 2003; Blondin & Mezzacappa, 2007), and high entropy plumes due to buoyant Rayleigh-Taylor instability (e.g., Kifonidis et al., 2003). These enhance the neutrino heating, providing the necessary energy to expand the shock at velocities of $v \sim 10^9 {\rm cm\,s^{-1}}$ in fractions of a second and trigger the explosion. After $\sim 1\,{\rm day}$, the shock reaches the most external hydrogen layer and breaks out (e.g., Wongwathanarat et al., 2017; Sandoval et al., 2021).

The PNS cools by emitting neutrinos while contracting. At the same time, it continues accreting shocked matter that has not been gravitationally unbound. The

random dynamics of these convection and accretion streams in the vicinity of the PNS can lead to relatively late ($t \sim 1\,\mathrm{s}$), low-Y_e, outflows (e.g., Navó et al., 2023). Eventually, the region above the PNS reaches very low densities (see Figures 2.4 and 2.5). At this point, neutrino energy deposition into the accreting matter can lead to high entropy, supersonic, laminar outflows, so-called neutrino driven winds that can last several seconds (Duncan et al., 1986).

2.4 CCSN Nucleosynthesis

CCSNe play an important role in the galactic chemical evolution. These events eject a large amount of material into the ISM. Part of the ejecta has been synthesized in the course of millions of years in the different stages of the stellar burning. However, a significant amount of the isotopes present in the ejecta is produced during the explosion. In this section, we present the basics of CCSN nucleosynthesis that is necessary to understand this work. We follow the recent reviews Martínez-Pinedo et al. (2016); Wanajo et al. (2018); Arcones & Thielemann (2023); Wanajo (2023).

Neutrinos and electron fraction

The electron fraction is changed by weak reactions, i.e., positron captures, β^-, and electron neutrino absorption on neutrons (Equation (2.6)) as well as electron captures (Equation (2.2)), β^+, and electron antineutrino absorption on protons (Equation (2.7)) (e.g., Arcones et al., 2010). Within CCSNe, especially neutrino properties are of importance. To get a deeper understanding of their influence, it is interesting to look at the equilibrium value of the electron fraction caused by neutrino absorption only, which is achieved if matter is long enough affected by (anti-)neutrinos. In this case, Y_e reaches an equilibrium which can be approximately expressed in terms of the luminosity of both neutrino flavors (L_{ν_e}, $L_{\bar{\nu}_e}$), and their average energy (ε_{ν_e}, $\varepsilon_{\bar{\nu}_e}$) (e.g., Qian & Woosley, 1996; Arcones & Thielemann, 2012; Just et al., 2021),

$$Y_{e,\mathrm{eq}} \simeq \left[1 + \frac{L_{\bar{\nu}_e}(\varepsilon_{\bar{\nu}_e} - 2\Delta + 1.2\Delta^2/\varepsilon_{\bar{\nu}_e})}{L_{\nu_e}(\varepsilon_{\nu_e} + 2\Delta + 1.2\Delta^2/\varepsilon_{\nu_e})}\right]^{-1}, \tag{2.10}$$

where $\Delta = m_n - m_p = 1.293\,\mathrm{MeV}$ is the mass difference between neutron and proton. If neutrino and antineutrino energies are similar, the electron fraction increases since the neutron-proton mass difference favors neutrino absorption reaction. Thus, to have neutron-rich conditions in the ejecta, neutrino and antineutrino energies must fulfill (Qian & Woosley, 1996; Martínez-Pinedo et al., 2016; Arcones & Thielemann, 2023):

$$\varepsilon_{\bar{\nu}_e} - \varepsilon_{\nu_e} \gtrsim 4\Delta - \left[\frac{L_{\bar{\nu}_e}}{L_{\nu_e}} - 1\right](\varepsilon_{\bar{\nu}_e} - 2\Delta) \sim 5\,\mathrm{MeV}. \tag{2.11}$$

Otherwise, if this condition is not fulfilled, Y_e in the ejecta increases. Notice that, the majority of the CCSN ejecta may never reach the previously shown equilibrium

value. Nevertheless, it shows the influence of electron (anti-)neutrinos on the neutron-richness and it is a therefore interesting quantity to trace.

Nucleosynthesis evolution

After bounce, post-shock matter is neutron-rich ($Y_e \sim 0.4$) as electron captures dominate in these high-density conditions (e.g., Arcones et al., 2010; Martin et al., 2018). Within the first hundreds of milliseconds after bounce ($t \sim 300\,\mathrm{ms}$ in Figure 2.5), the shock is very hot ($T_{\mathrm{shock}} > 10\,\mathrm{GK}$) and photodissociates the nuclei into neutrons, protons, and α-particles.

At $T \gtrsim 6\,\mathrm{GK}$, fusion reactions and photodisintegrations are in so-called nuclear statistical equilibrium (NSE). In NSE, all strong forward and reverse reactions are in equilibrium. This state is often expressed in terms of a chemical equilibrium between all nuclei and the composition for a thermodynamic state is therefore fully determined by using charge neutrality, mass conservation, and the so-called Saha equation (for more details, see Section 3.4.1 and, e.g., Hix & Thielemann 1999; Iliadis 2015, or, for an alternative approach using reaction equilibria see Clayton 1968).

The shocked region expands and cools down, eventually leaving NSE conditions in a short time-scale (see Figure 2.5). When matter drops out of NSE ($T \sim 6\,\mathrm{GK}$), for typical densities, the most abundant heavy isotope is the one with the highest binding energy at a given Y_e, e.g., the double magic number nuclei $^{48}\mathrm{Ca}$ for $Y_e \sim 0.4$ and $^{56}\mathrm{Ni}$ when $Y_e \sim 0.5$. When the system leaves NSE, it enters the regime of quasi-statistical equilibrium (QSE). When this happens, three-body reactions are slower than two-body reactions. This leads to the formation of several nuclei sub-clusters that are not in equilibrium anymore. Often, at least three clusters are assumed: light nuclei, Si-group, and Fe-group (Hix et al., 2007; Parete-Koon et al., 2008).

The final composition at the end of the QSE stage strongly depends on the neutron-richness of the ejected matter. This is highly influenced by neutrinos. Usually, neutrino and antineutrino luminosity, as well as their average energies, are quite similar. Thus, Equation (2.11) is not fulfilled, and electron neutrino absorption dominates over antineutrino absorption. The high number of neutrinos in the gain layer are absorbed by free neutrons and hence, for typical neutrino properties found in modern CCSN simulations, increase the electron fraction to $Y_e \sim 0.4 - 0.6$ (see Equation (2.10) and Wanajo et al. (2018)), depending on the $\varepsilon_{\bar{\nu}_e} - \varepsilon_{\nu_e}$ that has been subjected.

Therefore, most of the ejected matter hosts symmetric conditions ($Y_e \sim 0.5$). As a consequence, alpha-particles are the most abundant species (see Figure 2.5). This is the so-called α-rich freeze out (Woosley & Hoffman, 1992). The abundant α-particles synthesize significant fractions of α-elements from the uncompleted Si-burning, such as $^{32}\mathrm{S}$, $^{36}\mathrm{Ar}$, $^{40}\mathrm{Ca}$, and $^{44}\mathrm{Ti}$. This process is commonly referred to as the α-process (Woosley & Hoffman, 1992). The heaviest nucleus synthesized by the involved sequence of α captures lies around $^{56}\mathrm{Ni}$, since the Coulomb barrier increases with Z. The creation of heavier nuclei requires more neutron-rich conditions as neutron

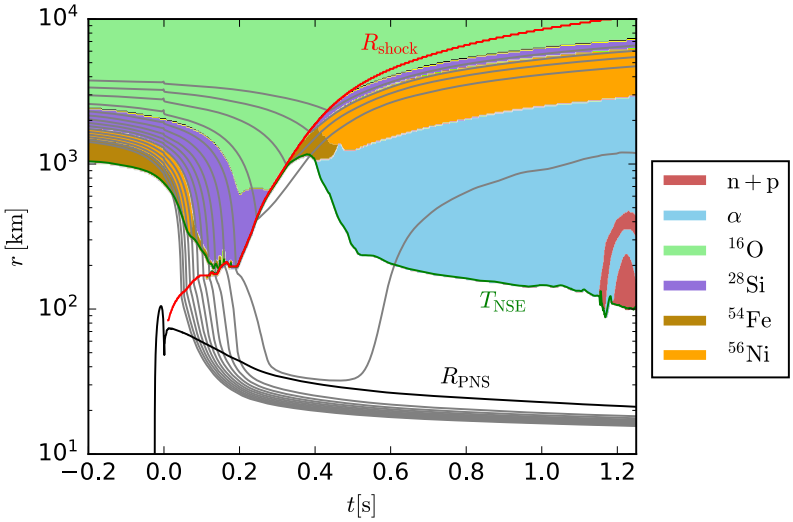

Figure 2.5: Characteristic mass shell evolution of a representative CCSN model. Grey lines correspond to trajectories of mass shells from $1.45\,\mathrm{M}_\odot$ to $1.70\,\mathrm{M}_\odot$. The red line depicts the shock radius, the black line shows the proto-neutron star radius, and the green line the temperature at which matter leaves NSE conditions. The different colors depict the most abundant specie in the region which is not in NSE.

captures are not affected by the Coulomb barrier. Hence, for slightly neutron-rich conditions, neutron-captures allow the formation of trans-iron species up to $A \sim 90$.

If the electron fraction at the end of QSE is $Y_e > 0.5$, free protons become also more abundant than heavy nuclei. Furthermore, antineutrino absorption on free protons release neutrons that are captured by neutron-deficient species. The succession of these reactions makes possible the production of $A > 64$ isotopes, e.g., ^{92,94}Mo and ^{96,98}Ru. This process is the so-called νp-process (e.g., Fröhlich et al., 2006; Pruet et al., 2006; Wanajo, 2006). However, although it can be the main production channel for some light p-rich species, it is a subdominant process in neutrino-heated ejecta.

After $t \sim 1\,\mathrm{s}$, the shock has lost part of its energy and cooled to $T \sim 2\,\mathrm{GK}$. At these radii, explosive oxygen burning takes place, and (α, γ) on ^{16}O, ^{20}Ne, and ^{24}Mg are the dominant reactions in the ^{16}O rich layer. After several seconds, the shock reaches the outermost mass shells (He and H). They are essentially ejected without significant changes in their composition.

Finally, there is also mass ejection from the vicinity of the PNS, through the outflows coming from accretion and convection streams and the aforementioned ν-driven winds. Since the matter surrounding the PNS is neutron-rich ($Y_e \gtrsim 0.3$), literature in the past considered ν-driven winds candidates for r-process nucleosynthesis due to

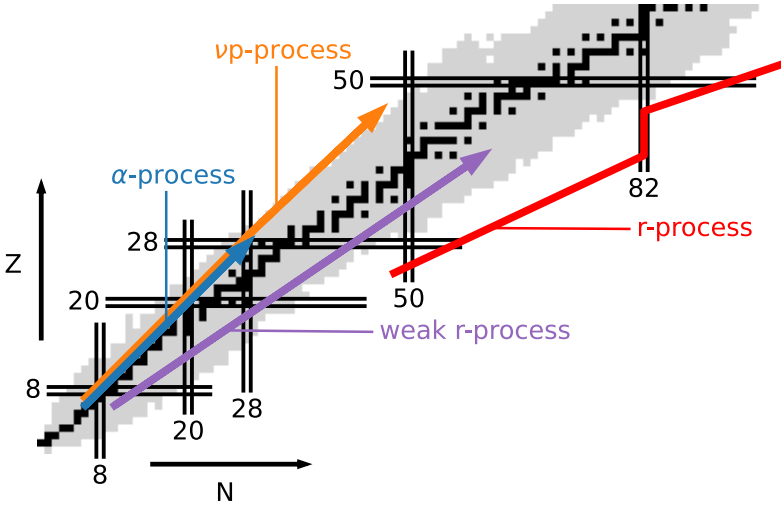

Figure 2.6: We schematically depict the paths that the main nucleosynthesis processes follow in CCSNe. Stable isotopes in black. We add part of the r-process path for completeness. Courtesy of Max Jacobi.

the high entropy that they involved (e.g., Woosley & Hoffman, 1992; Woosley et al., 1994).

The rapid neutron-capture process or r-process is the mechanism that synthesizes half of the heaviest isotopes in the universe. It takes place in environments with large neutron fluxes, where the timescales of neutron-captures are shorter than that of β-decays, allowing to synthesize very neutron rich species far from stability (see Figure 2.6). Therefore, it involves high neutron-to-seed ratio of $Y_n/Y_{\rm seed} \gtrsim 100$ (e.g., Freiburghaus et al., 1999).

Standard CCSN events, which we describe in this chapter, do not fulfill this condition (for a review see, e.g., Arcones & Thielemann, 2012). Neutrinos diffusing from the PNS are absorbed by neutrons and increase the Y_e of the matter, and hence avoid a full r-process signature (Wang & Burrows, 2023). However, in the presence of strong magnetic fields and rotation, the conditions necessary for the r-process to operate can be reached (e.g., Reichert et al., 2021). In these events, the magnetic pressure play an important role on driving the explosion (e.g., Obergaulinger & Aloy, 2020), and, thus, matter is not so exposed to neutrino fluxes that break neutron-rich conditions (see Obergaulinger & Reichert, 2023, for a recent review). In the aforementioned innermost regions, standard CCSNe present $Y_n/Y_{\rm seed} \lesssim 1$ (e.g., Arcones & Bliss, 2014; Bliss et al., 2018). Although, as mentioned, these conditions do not reproduce a full r-process signature, it allows for the production of first r-process peak nuclei such, e.g., ^{84}Se, and lighter heavy species up to $A \sim 90 - 100$ (e.g., Eichler et al., 2017; Wanajo,

2023). Thus, standard CCSNe host the so-called weak r-process (e.g., Arcones & Bliss, 2014), depicted in Figure 2.6.

2.5 Remnants

When the explosion sets in, a PNS is left behind, which continues cooling by diffusing neutrinos during several seconds until the neutron star (NS) is born (e.g., Pons et al., 1999). These are very compact objects of $R_{\rm NS} \sim 12\,{\rm km}$ and $M_{\rm NS} \sim 1.4\,{\rm M}_\odot$. The maximum mass of a PNS/NS before collapsing to a BH highly depends on the equation of state (EOS) of nuclear matter (see Section 3.3), which essentially relates pressure, density, temperature, and Y_e from the different nuclear physics inputs. Hence, due to the high densities and pressures involved, these astrophysical sites also provide a great laboratory to test the nuclear matter properties. This soon captured the attention from the nuclear physics community and contributed to interest in the topic (e.g., Lattimer & Swesty, 1991; Shen et al., 1998; Hempel et al., 2012; Steiner et al., 2013; Schneider et al., 2017).

If the shock fails to revive, the supernova explosion does not take place. The shock continues stalled and the PNS keeps accreting matter. Eventually, it reaches its maximum mass and collapses to a BH (e.g., O'Connor & Ott, 2011). These events can be characterized by the absence of electromagnetic counterpart. Moreover, not always a NS is born after a successful revival of the shock. In case of a very weak explosion, shocked matter can fall back and accrete to the PNS after several seconds. If the PNS overcomes the maximum mass, it collapses to a BH. In rotating massive stars ($M \gtrsim 30\,{\rm M}_\odot$), the central BH can accrete matter with enough angular momentum to form an accretion disk, forming a so-called collapsar. The geometry arising from the accretion disk leads to the formation of jets along the rotational axis, which are suggested to be sources of γ-ray bursts (GRBs) (see, e.g., Woosley, 1993; MacFadyen & Woosley, 1999), energetic flashes of $\gtrsim 100\,{\rm keV}$ that can last from fractions of seconds (short GRBs) to seconds (long GRBs).

2.6 Observables

CCSNe explosions are multi-messenger astronomical sites that can be observed through their electromagnetic (EM) counterpart, their neutrino signal, and potentially by their gravitational wave (GW) emission. As in any other field, observations constrain theory and help to develop more accurate theoretical models.

The EM counterpart is the most important evidence from CCSN that we can observe from Earth. It can constrain multiple properties of the event such, e.g., the distance, the explosion energy, the yields, or the progenitor structure (e.g., Barker et al., 2022). The time evolution of luminosity emitted by the photosphere of the ejecta is the so-called light curve (LC). When the shock reaches the outermost layers of the star,

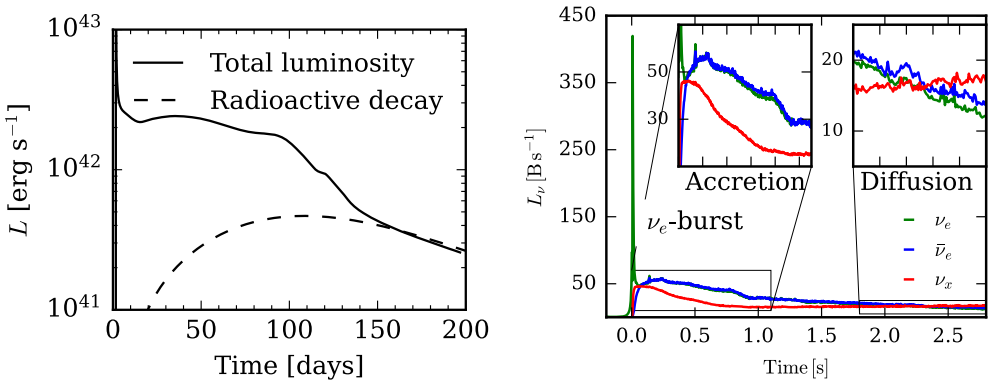

Figure 2.7: The left panel shows an example of a synthesized CCSN LC, courtesy of Finia Jost. The plateau phase is powered by H recombination in the ejecta. After $\sim 90\,\mathrm{days}$, the recombination ends and the LC is powered by radioactive decays. Right panel shows an example of the emitted neutrino luminosity from a 1D CCSN model. $1\,\mathrm{B} = 10^{51}\,\mathrm{erg\,s^{-1}}$.

the ejecta expand and start to cool down. When the temperature drops enough, recombination in the H shell takes place and powers the first $\sim 100\,\mathrm{days}$ after shock breakout (e.g., Morozova et al., 2015; Curtis et al., 2021). The photosphere recedes in mass coordinates and cools down slowly. In this phase, the LC forms a plateau (see left panel of Figure 2.7). After that, the photosphere hits the He layer and the recombination ceases since He recombines at much higher temperature. At this point, the decay of $^{56}\mathrm{Ni}$ towards $^{56}\mathrm{Fe}$ becomes the main contribution to the LC (e.g., Arnett, 1980). Some stars experience strong winds during their evolution that release a big part of the outermost H- and He-rich layer (e.g., Woosley et al., 2002). In this case, recombination does not contribute and the LC is fully dominated by the decay of the radioactive isotopes (e.g., Morozova et al., 2015).

The successful observation of a CCSN LC depends on numerous factors, such as, e.g., the intrinsic luminosity of the event, the presence of dust, or the sensitivity of the telescope. Most of the observed LCs come from events that take place at a distance of $10-100\,\mathrm{Mpc}$, and usually are detectable for, at least, $\sim 100-150\,\mathrm{days}$ (e.g., Barbarino et al., 2015; Zampieri, 2017; Szalai et al., 2019).

As stated in the previous sections, neutrinos play a key role in the explosion. In contrast to the LC, neutrino emission is dominant at much earlier times, and their luminosity decays in a timescale of seconds. Short after the bounce, neutrinos become transparent and the neutrino burst is produced. A large amount of ν_e are emitted with an energy of $\epsilon_\nu \sim 10-20\,\mathrm{MeV}$ and produce a very bright peak luminosity, of the order of several $10^{53}\,\mathrm{erg\,s^{-1}}$ (right panel in Figure 2.7). After that, accretion streams onto the hot PNS produce a significant number of ν_e and $\bar{\nu}_e$ in charged current reactions.

Nevertheless, L_{ν_e} decreases an order of magnitude and, thus, a detection in this phase is more challenging. After $\sim 1\,\mathrm{s}$, the luminosity is powered mainly by diffusion from the PNS and becomes much fainter. Despite the large amount of neutrinos released in the explosion, there has only been one detection of neutrinos from CCSNe that dates back to 1987 (e.g., Arnett et al., 1989). Kamiokande II (Hirata et al., 1987), IMB (Bionta et al., 1987), and Baksan (Alekseev et al., 1987) registered a total of 25 neutrinos from SN1987A, which took place in the Large Magellanic Cloud, $\sim 55\,\mathrm{kpc}$ away. In the near future, new generation neutrino detectors such, e.g., HyperKamiokande (Abe et al., 2021), and DUNE (Abi et al., 2021), should be able to observe more accurately any signal coming from a galactic CCSN. It is expected that they will be able to detect of the order of several thousands of neutrinos in a galactic event and infer the luminosity evolution and, perhaps, even the spectra.

GWs in CCSNe are generated by non-spherical matter motions like, e.g., convection and the SASI in the post-shocked region, and buoyancy in the PNS interior (for reviews see, e.g., Kotake & Kuroda, 2017; Abdikamalov et al., 2021). Thus, they can provide useful information of the PNS structure. Unfortunately, there has not been any confirmed detection of GWs coming from CCSNe (Abbott et al., 2020; Szczepańczyk et al., 2023), since the current GW detectors have sensitivity to only detect an uncommon galactic event (Abbott et al., 2016).

The community is eager to witness a galactic CCSN event that would trigger a very important multimessenger observation and will be a milestone in the field. Hopefully, it will be soon.

3 CCSNe simulations in Aenus-Alcar

CCSNe simulations are of vital importance for understanding the mechanisms of the explosion. Simulations follow the evolution from the collapsing iron core until several seconds after bounce. To do so, they evolve the hydrodynamic equations in a discretized grid, and include all of the physics involved in the event as faithfully as possible, e.g., neutrino transport and interactions, (general relativistic) gravity, or EOS of dense matter.

The first hydrodynamical simulations were performed in spherical symmetry by Colgate & Johnson (1960); Colgate et al. (1961). In recent years, significant advances have been reported in multidimensional simulations (e.g., Lentz et al., 2015; Janka et al., 2016; Roberts et al., 2016; O'Connor & Couch, 2018; Obergaulinger & Aloy, 2020; Burrows et al., 2020; Kuroda et al., 2020; Sandoval et al., 2021; Nakamura et al., 2022), impact of magnetic fields (e.g., Mösta et al., 2015; Obergaulinger et al., 2018; Bugli et al., 2021; Varma et al., 2022), pre-supernova models (e.g., Müller et al., 2017; Fields & Couch, 2021; Yoshida et al., 2021; Vartanyan et al., 2021), neutrino transport (for an extended review, see Mezzacappa et al., 2020a) and reactions (e.g., Balasi et al., 2015, and references therein), high-density equations of state (EOS) (e.g., Schneider et al., 2019; Yasin et al., 2020) or nucleosynthesis calculations (e.g., Eichler et al., 2017; Wanajo et al., 2018; Curtis et al., 2019; Sieverding et al., 2020; Witt et al., 2021; Reichert et al., 2021). 3D state-of-the-art CCSN models are very computationally expensive and take months to simulate hundreds of milliseconds. Thus, CCSN simulations often consider simplified or approximated treatments to make them faster, e.g., one- and two-dimensional simulations, simplified neutrino treatment, simplified gravity, or simplified nuclear reactions treatment.

In this chapter we introduce the main aspects necessary to lay the groundwork for performing state-of-the-art CCSNe simulations in the absence of magnetic fields. We employ the Aenus-Alcar code (Just et al., 2015; Obergaulinger & Aloy, 2017) to perform the simulations. Therefore, we review its main characteristics that are important for this study. In Section 3.1, we derive the hydrodynamic equations and present how they are numerically modeled. In Section 3.2, we introduce the neutrino treatment and focus on the two-moment approach. We derive the Helmholtz EOS, and introduce the EOSs of dense matter in Section 3.3. Finally, present the treatment of the composition in Section 3.4.

3.1 Hydrodynamics

3.1.1 Euler equations

In this section, we derive the Euler equations of hydrodynamics following Weinberg (2007); Ryden (2011).

We start from the distribution function $f(\vec{x}, \vec{v}, t)$, which is the probability of finding a particle of gas at a time t at the position $\vec{x}$ with the velocity $\vec{v}$. Integrating over phase space, we obtain the total number of particles N,

$$\int \int f(\vec{x}, \vec{v}, t) \mathrm{d}^3x \mathrm{d}^3v = N. \tag{3.1}$$

If N is conserved,

$$\frac{\partial f}{\partial t} + \sum_i \left(\dot{x}_i \frac{\partial f}{\partial x_i} + \dot{v}_i \frac{\partial f}{\partial v_i} \right) = \left(\frac{\mathrm{d}f}{\mathrm{d}t} \right)_{\mathrm{c}}. \tag{3.2}$$

Applying $v_i = \dot{x}_i$ and $g_i = \dot{v}_i$, we obtain the Boltzmann equation,

$$\frac{\partial f}{\partial t} + \sum_i v_i \frac{\partial f}{\partial x_i} + \sum_i g_i \frac{\partial f}{\partial v_i} = \left(\frac{\mathrm{d}f}{\mathrm{d}t} \right)_{\mathrm{c}}, \tag{3.3}$$

where the RHS is the so-called collision term that accounts for the forces between particles. We can multiply Equation (3.3) both sides by the mass m and integrate over d^3v,

$$\frac{\partial}{\partial t} \int m f \mathrm{d}^3v + \sum_i \frac{\partial}{\partial x_i} \int m f v_i \mathrm{d}^3v + m \int \sum_i \frac{\partial}{\partial v_i} (g_i f) \mathrm{d}^3v = \int m \left(\frac{\mathrm{d}f}{\mathrm{d}t} \right)_{\mathrm{c}} \mathrm{d}^3v \tag{3.4}$$

The first term is $\frac{\partial \rho}{\partial t}$, the second term $\sum_i \frac{\partial}{\partial x_i}(\rho \langle v_i \rangle) \equiv \vec{\nabla} \cdot (\rho \vec{u})$ and the third term vanishes following the divergence theorem and assuming $f = 0$ when $v \to \infty$. Local mass conservation prevents particles from being created or destroyed at a given place, only shifting them in velocity space, which is why the RHS disappears. Hence, we finally obtain:

$$\frac{\partial \rho}{\partial t} + \vec{\nabla} \cdot (\rho \vec{u}) = 0, \tag{3.5}$$

which is the mass continuity equation. Analogously, one can follow a similar procedure to obtain the continuous equations for all conserved quantities in the system, such the momentum ($\vec{p} = m\vec{v}$), the energy ($e = mv^2$), the electron fraction (ρY_{e}), and the partial densities of the different species (ρX_k):

$$\frac{\partial \vec{p}}{\partial t} + \vec{\nabla} \cdot \left(\vec{p}\vec{u} + P \overleftrightarrow{I} - \overleftrightarrow{\pi} \right) = \vec{Q_{\mathrm{M}}}, \tag{3.6}$$

$$\frac{\partial e}{\partial t} + \vec{\nabla} \cdot ((e + P)\vec{v} - \overleftrightarrow{\pi}\vec{v}) = \vec{v}\vec{Q_{\mathrm{M}}} + Q_{\mathrm{E}}, \tag{3.7}$$

$$\frac{\partial \rho Y_{\rm e}}{\partial t} + \vec{\nabla} \cdot (\rho Y_{\rm e} \vec{u}) = Q_{\rm N}, \tag{3.8}$$

$$\frac{\partial (\rho X_k)}{\partial t} + \vec{\nabla} \cdot (\rho X_k \vec{v}) = \rho S_{X_k}, \tag{3.9}$$

where P is the gas pressure, $\overleftrightarrow{I}$ is the identity matrix, and $\overleftrightarrow{\pi}$ is the viscous stress tensor, which for ideal hydrodynamics vanishes. $\vec{Q_{\rm M}}$ and $Q_{\rm E}$ are the hydrodynamic source terms responsible for the change of fluid momentum and gas internal energy, respectively. $Q_{\rm N}$ is the source term due to weak reactions, see Section 3.2.1. S_{X_k} is the source that takes into consideration changes from one species to another. Gravity ($\vec{f}_{\rm G} = -\rho \vec{\nabla} \varphi$) is the most relevant external force, i.e. the main contribution to $Q_{\rm M}$. The gravitational potential (φ) is obtained applying the Poisson's law from the density,

$$\vec{\nabla}^2 \varphi = 4\pi\rho. \tag{3.10}$$

In Aenus-Alcar, the potential has some corrections terms following Marek et al. (2006) to approximately mimic the effects of general relativity. The main contribution to $Q_{\rm E}$ is the energy deposited by neutrinos, which are the responsible to trigger the explosion. In addition, as we will see in Chapter 5, at lower densities and temperatures the energy released in nuclear reactions is also significant.

Equations (3.5) to (3.9) constitute a system of partial differential equations that is closed applying an extra equation, the equation of state (EOS), which relates pressure and density (see Section 3.3).

3.1.2 Numerical modeling

The Euler equations introduced in the previous section constitute an hyperbolic system that is solved under the so-called finite volume (FV) approach (see, e.g., LeVeque, 2002). For simplicity, in this section we briefly describe the method for the 1D case. A generalization to multi-D by dimensional splitting is, in principle, straightforward. It consist on discretize the spatial domain into N cells, and evolving in time the integral of the conserved variables over these volumes. These values are updated in small timesteps (Δt) by computing the advection flux at the grid intercells.

For simplicity, the grids are usually ortogonal, e.g, cartesian, spherical or cylindrical. In each grid zone i, at $t^n = n\Delta t$, the integral mean value of the conserved variable u_i^n is computed and assigned to the center of the cell (x_i),

$$u_i^n = \frac{1}{\mathcal{V}_i} \int_{\mathcal{V}_i} u(\vec{x}, t^n)\, {\rm d}V, \tag{3.11}$$

where $\mathcal{V}_i$ is the volume of the $i-{\rm th}$ cell. Since u is a conserved variable, the integral mean value u_i^n can only change the next timestep (t^{n+1}) due to fluxes at the cell boundaries ($i - 1/2$ and $i + 1/2$) with a form similar to

$$u_i^{n+1} = u_i^n - \frac{\Delta t}{\Delta x}(F_{i+1/2}^n - F_{i-1/2}^n), \tag{3.12}$$

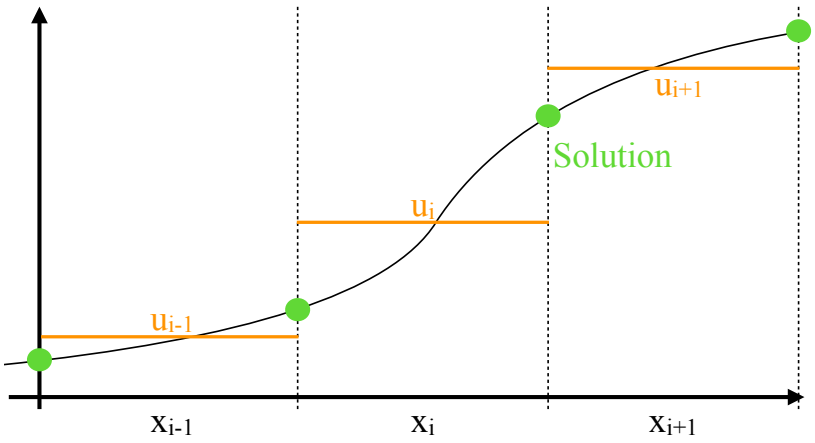

Figure 3.1: Representation of the reconstruction and the Riemann problem. The integral mean values, e.g., u_i, and u_{i+1}, need to be reconstructed at the cell interface $x_i + \Delta x_i/2$. Then, an approximate Riemann solver is applied to obtain the solution at this point (green) and to mimic the desired physical quantity (black solid line).

where $F^n_{i+1/2}$ is the flux at the intercell $i + 1/2$ at t^n. This leads to a piecewise constant system which, of course, is not physically accurate (as seen in Figure 3.1). Therefore, hydrodynamic codes need first to reconstruct the conserved variables in the intercells through polynomials, in order to obtain the fluxes for both coinciding grid zones. The reconstruction has to fulfill consistency, accuracy and stability constrains (as detailed in, e.g, LeVeque, 2002) to capture shocks and strong gradients as well as obtaining a good approximation in smooth regions. Commonly, state-of-the-art CCSNe codes employ higher-order reconstruction methods such WENO (see, e.g., Shu, 1998) or MP (Suresh & Huynh, 1997). Once the fluxes from both coinciding cells are reconstructed, we encounter a discontinuity separating them in the intercell. This defines the Riemann problem,

$$F^n_{i+1/2} = \begin{cases} F^n_{i+1/2}(u_i) & \text{if } x < x_i + \Delta x_i/2 \\ F^n_{i+1/2}(u_{i+1}) & \text{if } x > x_i + \Delta x_i/2 \end{cases}, \tag{3.13}$$

which solution consists of a finite sets of waves travelling at constant speeds that provide the resulting advection flux. Ideally, at each cell edge, an exact Riemann solver is applied (Godunov, 1959), which takes into account all of the resulting shock and rarefaction waves from a shock tube problem in order to find the resulting advection flux. However, an exact Riemann solver is computationally tough to implement. Therefore, approximate solvers are used instead, e.g. HLL (Harten et al., 1983), Lax-Friedrichs (see, e.g, LeVeque, 1992), which only consider a small portion of the full

characteristic information, i.e., a reduced set of characteristic waves. These methods must fulfill consistency with the integral conservation and the entropy condition ($\Delta s \geq 0$). Therefore, to guarantee stability, they need to add some diffusion (e.g, LeVeque, 1992, 2002).

When the advection flux is finally computed, the hydrodynamic system is solved using an ordinary differential equation (ODE) integrator and evolved to the next timestep t^{n+1}. The flux calculation requires a constant state at the intercells. Therefore, the fastest wave resulting from the solution of the Riemann problem cannot propagate more than one cell within one timestep. This is the CFL condition (Courant et al., 1928), which is necessary to ensure consistency and convergency. Thus, the timestep Δt is limited by,

$$\Delta t_i = \mathrm{CFL}\frac{\Delta x_i}{c_i}, \tag{3.14}$$

where $\mathrm{CFL} \leq 1$, Δx_i is the cell width, and c_i is the velocity of the fastest wave.

3.2 Neutrino scheme

3.2.1 Two-moment neutrino transport

Neutrinos are a key input for core-collapse supernovae simulations, since they transport the energy from the hot PNS to the shock and, therefore, trigger the explosion. The evolution of neutrinos it is determined by solving the relativistic Boltzmann transport equation for their particle distribution function ($f(x^\mu, p^\alpha)$), from Equation (3.1), $\mathcal{F}$ in the coming equations. Following Lindquist (1966); Cernohorsky & van Weert (1992),

$$p^\alpha \left[\frac{\partial \mathcal{F}_\nu}{\partial x^\alpha} - \Gamma^\beta_{\alpha\gamma} p^\gamma \frac{\partial \mathcal{F}_\nu}{\partial p_\beta}\right] = C[\mathcal{F}_\nu]. \tag{3.15}$$

The left hand side of the equation is the directional derivative of f along the phase flow. The right hand side corresponds to the collision term, which describes the change in N due to scattering, emission, or absorption. It can be expressed in the form,

$$\epsilon^{-1} C(\mathcal{F}) = \kappa_\alpha(\mathcal{F}^{(0)} - \mathcal{F}) + \kappa_s \left[\int \frac{\mathrm{d}^2\Omega'}{4\pi}\Phi(\cos\Theta')\mathcal{F}' - \mathcal{F}\right] + C_{\mathrm{pair}} + C_{\mathrm{non-iso}} \tag{3.16}$$

where κ_a is the absorption opacity, κ_s corresponds to the isoenergetic scattering opacity, $\mathcal{F}^{(0)}$ is the Fermi-Dirac distribution function at local thermodynamic equilibrium and $\int \frac{\mathrm{d}^2\Omega'}{4\pi}\Phi(\cos\Theta') = 1$. C_{pair} and $C_{\mathrm{non-iso}}$ are the collision terms that account for pair-processes and non-isoenergetic scattering, respectively. They are built employing the so-called angular kernel approximations (e.g., Bruenn, 1985; Rampp & Janka, 2002; Just et al., 2018), which use Legendre polynomial expansion in the scattering angle. For simplicity, in the following derivation we consider only the two first terms from Equation (3.16).

As one may notice, Equation (3.15) lives in the seven-dimensional space, which makes it very costly to evolve. Hence, approximations are often made in order to reduce the dimensionality of the system without compromising the accuracy in excess (for an extended review, see Mezzacappa et al., 2020b). AENUS-ALCAR neutrino transport scheme (introduced in Just et al., 2015) employs a two-moment neutrino transport (e.g., see Cernohorsky & van Weert, 1992) with an algebraic Eddington factor closure (e.g., the so-called M1 closure, first introduced by Levermore, 1984; Dubroca & Feugeas, 1999). This method takes advantadge of the Eddington approximation to obtain the first moments of the monochromatic intensity $\mathcal{I}$, which relates to the neutrino distribution function through

$$\mathcal{I}(\vec{x},\vec{n},\epsilon,t) = \left(\frac{\epsilon}{hc}\right)^3 c\mathcal{F}(\vec{x},\vec{p},\epsilon,t). \tag{3.17}$$

where $\epsilon \equiv |\vec{p}|c$ and $\vec{n} \equiv \vec{p}/|\vec{p}|$ indicate the momentum coordinates.

The zeroth, first, and second moment, i.e., the monochromatic energy density ($E(\epsilon)$), flux density ($F^i(\epsilon)$) and pressure tensor ($P^{ij}(\epsilon)$), read

$$cE(\epsilon) = \int \mathrm{d}\Omega\, \mathcal{I}, \tag{3.18}$$

$$F^i(\epsilon) = \int \mathrm{d}\Omega\, \mathcal{I}\, n^i, \tag{3.19}$$

$$cP^{ij}(\epsilon) = \int \mathrm{d}\Omega\, \mathcal{I}\, n^i n^j, \tag{3.20}$$

By using these moments, the full angular dependence of the system is removed and hence, the radiation evolution equations are simpler to solve numerically. The source terms of the transport equation, $C^{(0)}$ and $C^{(1),i}$ are the zeroth and first angular moments, respectively, of the collision term (Equation (3.16)),

$$C^{(0)} = c\kappa_a(E^{\mathrm{eq}} - E) \tag{3.21}$$

$$C^{(1),i} = -c(\kappa_a + \kappa_s)F^i, \tag{3.22}$$

where E^{eq} is the equilibrium energy density associated with the Fermi-Dirac distribution. When energy integrated, they relate to the source terms for the hydrodynamic equations:

$$Q_{\mathrm{E}} = -\sum_{\text{species}} \int_0^\infty C^{(0)}\, \mathrm{d}\epsilon, \tag{3.23}$$

$$Q^i_{\mathrm{M}} = -\frac{1}{c^2}\sum_{\text{species}} \int_0^\infty C^{(1),i}\, \mathrm{d}\epsilon, \tag{3.24}$$

$$Q_{\mathrm{N}} = -m_{\mathrm{B}} \int_0^\infty \left[\left(\frac{C^{(0)}}{\epsilon}\right)_{\nu_e} - \left(\frac{C^{(0)}}{\epsilon}\right)_{\bar{\nu}_e}\right] \mathrm{d}\epsilon \tag{3.25}$$

The two-moment approximation implies that the series of angular moments to which the transport equation is developed, is truncated at the second moment. Therefore, it needs to be given by some approximation. AENUS-ALCAR includes several algebraic Eddington factor ($\chi^{ij} \equiv P^{ij}/E$) closures which consider different approximations: the Minerbo closure (Minerbo, 1978), its generalized version by Cernohorsky & Bludman (1994), the aforementioned M1, and the obtained by Janka (1991). All of them have to fulfil the boundary cases of the diffusion limit and free-streaming limit. In the first case, the neutrino-matter interactions are significant and $\mathcal{I}(\vec{x}, \vec{n}, \epsilon, t)$ can be considered isotropic. For the second case, neutrino-matter interactions are negligible and, therefore, $\mathcal{I}(\vec{x}, \vec{n}, \epsilon, t)$ is maximally anisotropic and neutrinos propagate in one direction, i.e., without scattering.

3.2.2 Neutrino-matter interactions in Aenus-Alcar

AENUS-ALCAR includes the most important neutrino-matter interactions (Just et al., 2015; Obergaulinger & Aloy, 2020):

(i) Electron flavor neutrino absorption by free nucleons and nuclei

$$\nu_e + n \rightarrow e^- + p \tag{3.26}$$

$$\bar{\nu}_e + p \rightarrow e^+ + n \tag{3.27}$$

$$\nu_e + (A, Z) \rightarrow e^- + (A, Z+1) \tag{3.28}$$

(ii) Electron and positron captures by free nucleons and nuclei

$$p + e^- \rightarrow n + \nu_e \tag{3.29}$$

$$n + e^+ \rightarrow p + \bar{\nu}_e \tag{3.30}$$

$$(A, Z+1) + e^- \rightarrow (A, Z) + \nu_e \tag{3.31}$$

(iii) Isoenergetic scattering of neutrinos and antineutrinos off free nucleons and nuclei

$$\nu + n, p \rightarrow \nu + n, p \tag{3.32}$$

$$\nu + (A, Z) \rightarrow \nu + (A, Z) \tag{3.33}$$

(iv) Inelastic scattering of neutrinos and antineutrinos off electrons and positrons

$$\nu + e \rightarrow \nu + e$$

(v) Pair processes production

$$e^- + e^+ \rightarrow \nu + \bar{\nu} \tag{3.34}$$

$$N + N \rightarrow N + N + \nu + \bar{\nu}. \tag{3.35}$$

The source terms of the transport equation (see Equations (3.21) and (3.22)) incorporate absorption, emission, and scattering through the respective opacities, κ_a and κ_s, as well as the approximate expansions that include (iv) and (v) (Just et al., 2018). In this work, the absorption of neutrinos by free nucleons and nuclei will be of particular relevance because these processes are the only ones that change the electron fraction of the matter. Therefore, we briefly describe the absorption opacities treatment in AENUS-ALCAR, which is based on Cernohorsky & van Weert (1992). We can decompose κ_a among the different contribution from each absorption processes (Equations (3.26) to (3.28)),

$$\kappa_a = \kappa_{a,\nu n} + \kappa_{a,\bar{\nu} p} + \kappa_{a,\nu A}. \tag{3.36}$$

The absorption opacity from neutrino absorption by free neutrons is

$$\kappa_{a,\nu n} = n_n \sigma_{\nu n}(\epsilon)\theta(E^{\mathrm{eq}}_{e^-}, E^{\mathrm{eq}}_{\nu}). \tag{3.37}$$

where n_n is the free neutron particle density, $\sigma_{\nu n}(\epsilon)$ is the $\nu_e - n$ cross section and θ is a blocking factor for stimulated absorption and emission, which depends on the equilibrium energy density associated with the electron and neutrino distribution functions. Analogously, the absorption opacity from antineutrino absorption by free protons reads

$$\kappa_{a,\bar{\nu} p} = n_p \sigma_{\bar{\nu} p}(\epsilon)\theta(E^{\mathrm{eq}}_{e^+}, E^{\mathrm{eq}}_{\bar{\nu}}). \tag{3.38}$$

The term accounting for the neutrino absorption by nuclei is subdominant with respect the former two. Following Bruenn (1985), it gets a similar form as Equations (3.37) and (3.38),

$$\kappa_{a,\nu A} \propto n_A \sigma_{\nu A}(\epsilon, N_Z, N_N)\theta(E^{\mathrm{eq}}_{e^-}, E^{\mathrm{eq}}_{\nu}), \tag{3.39}$$

for each nucleus A included in the composition. Under the aforementioned approach, the cross-sections are proportional to the number of neutrons (N_n) and protons (N_p) the nuclei (Z, N) have,

$$\sigma_{\nu A} \propto N_p(Z), N_n(N), \tag{3.40}$$

$$N_p(Z) = \begin{cases} 0, & \text{if } Z < 20 \\ Z - 20, & \text{if } 20 < Z < 28 \\ 8, & \text{if } Z > 28 \end{cases} \tag{3.41}$$

$$N_n(N) = \begin{cases} 6, & \text{if } N < 34 \\ 40 - N, & \text{if } 34 < N < 40 \\ 0, & \text{if } N > 40 \end{cases} \tag{3.42}$$

The system is discretized into the N_{v} finite volume cells described in Section 3.1.2, and a grid in the energy space composed by N_ϵ energy bins. The set of moment equations is solved for each energy bin and for each species since the source terms depend on the energy and species of neutrinos. Therefore, the multidimensional

($N_{\rm dim}$), multi-group radiation transport scheme solves a total of $N_{\rm species} \times N_\epsilon \times (N_{\rm dim}+1)$ equations.

Finally, Aenus-Alcar solves the transport equations in the co-moving frame, i.e., co-moving with the fluid and at a speed v with respect to the lab frame. As stated in Just et al. (2015), the collision part of Equation (3.15) is less challenging to compute in this frame. However, sometimes, one may need to transform to lab frame. This is the case, for example, when the neutrino luminosity needs to be provided. The transformation between frames is easier for the frequency-integrated than the spectral moments. They are defined as,

$$\{\bar{E}, \bar{F}^i, \bar{P}^{ij}\} = \int \mathrm{d}\epsilon \{E, F^i, P^{ij}\}. \tag{3.43}$$

Thus, the transformation, at $\mathcal{O}(v/c)$, reads

$$\bar{E}_{\rm lab} = \bar{E} + \frac{2}{c^2} v_j \bar{F}^j, \tag{3.44}$$

$$\bar{F}^i_{\rm lab} = \bar{F}^i + v^i \bar{E} + v_j \bar{P}^{ij}, \tag{3.45}$$

$$\bar{P}^{ij}_{\rm lab} = \bar{P}^{ij} + \frac{1}{c^2}(v^i \bar{F}^j v^j \bar{F}^i). \tag{3.46}$$

3.2.3 Heating factor

One-dimensional (1D) simulations, i.e., assuming spherical symmetry, lack of non-radial deformations that enhance the neutrino energy deposition in the gain layer. Therefore, the neutrino energy heating in the gain region is not enough to revive the shock and the explosion is not triggered. Hence, 1D CCSNe simulations usually employ an artificial term to reproduce successful explosions (see, e.g., Woosley & Weaver, 1995; Thielemann et al., 1996; Perego et al., 2015; Couch et al., 2020).

Aenus-Alcar includes a heating factor (*HF*) that enhances the neutrino heating in the gain layer (see e.g., Witt, 2020, for a similar approach):

$$Q_\nu^{\rm gain, HF} = HF \cdot Q_\nu^{\rm gain}, \tag{3.47}$$

where $Q_\nu^{\rm gain}$ is the neutrino energy deposition $Q_{\rm E}$ (see Equation (3.23)) in the gain region. Hence, the neutrino heating is applied to the energy source term of the hydrodynamic equations (Equation (3.7)).

The fact that the heating factor does not modify any of the source terms of the neutrino transport equations ($C^{(0)}$ and $C^{(1),i}$) is a strength of the method, in addition to its simplicity. Because of this, it does not modify $Q_{\rm N}$ (see Equation (3.23)), which is the source term for the Y_e conservation equation (Equation (3.8)). Thus, the heating factor does not affect the Y_e, which would lead to unphysical changes in the nucleosynthesis.

3.3 Equation of State in CCSNe

As stated in Section 3.1, the EOS provides the closure to the hydrodynamic equations relating the conserved variables (e.g., density or total energy density) with thermodynamic quantities such pressure or thermal energy. Furthermore, the EOS describes the relation between macroscopic thermodynamic quantities such pressure, density, and temperature from the fundamental interaction between particles (Section 3.3.1). CCSNe include a broad range of thermodynamic conditions (see Section 3.3.2). Below nuclear saturation densities, the physics are well known and a Helmholtz EOS can be used (see Section 3.3.3). However, beyond ρ_0, the strong interaction dominates and the many-body problem arises (e.g., Oertel & Providência, 2018). Thus, CCSNe are of great interest for the nuclear physics community since they are laboratories to test the properties of dense matter (see Section 3.3.4).

3.3.1 Statistical mechanics

Statistical mechanics studies the possible microstates of the system, known as ensemble. In the canonical ensemble, one fixes the number of particles N, the volume V, and the temperature T. The energy E is variable, i.e., the system can exchange heat with a reservoir in thermal equilibrium. The probability P_n for a microstate n with energy E_n is:

$$P_n = \frac{\Omega_R(E_T - E_n)}{\Omega_T(E_T)}, \tag{3.48}$$

where Ω_R is the number of eigenstates of the reservoir with energy E_R, $E_T = E_n + E_R$ is the total energy, and Ω_T is the total number of microstates. Assuming $E_T \gg E_n$,

$$\ln P_n \approx \ln \Omega_R(E_T) - E_n \frac{\partial}{\partial E_T} \ln \Omega_R(E_T) - \ln \Omega_T(E_T). \tag{3.49}$$

From the relation

$$\beta = \frac{1}{k_\mathrm{B} T} = \frac{\partial}{\partial E_T} \ln \Omega_R(E_T), \tag{3.50}$$

where k_B is the Boltzmann constant, we obtain the probability for the system to be in the microstate n:

$$P_n = \frac{1}{Z} e^{-\beta E_n}. \tag{3.51}$$

Z is the sum of all possible microstates of the system, the so-called partition function,

$$Z(\beta) = \sum_n e^{-\beta E_n}. \tag{3.52}$$

The derivative of its logarithm over β relates with the internal energy, i.e. average energy:

$$U = \langle H \rangle = \frac{1}{Z} \sum_n \langle n|H|n\rangle e^{-\beta E_n} = \frac{1}{Z} \sum_n E_n e^{-\beta E_n} = -\left(\frac{\partial}{\partial \beta} \ln Z\right)_{V,N}. \tag{3.53}$$

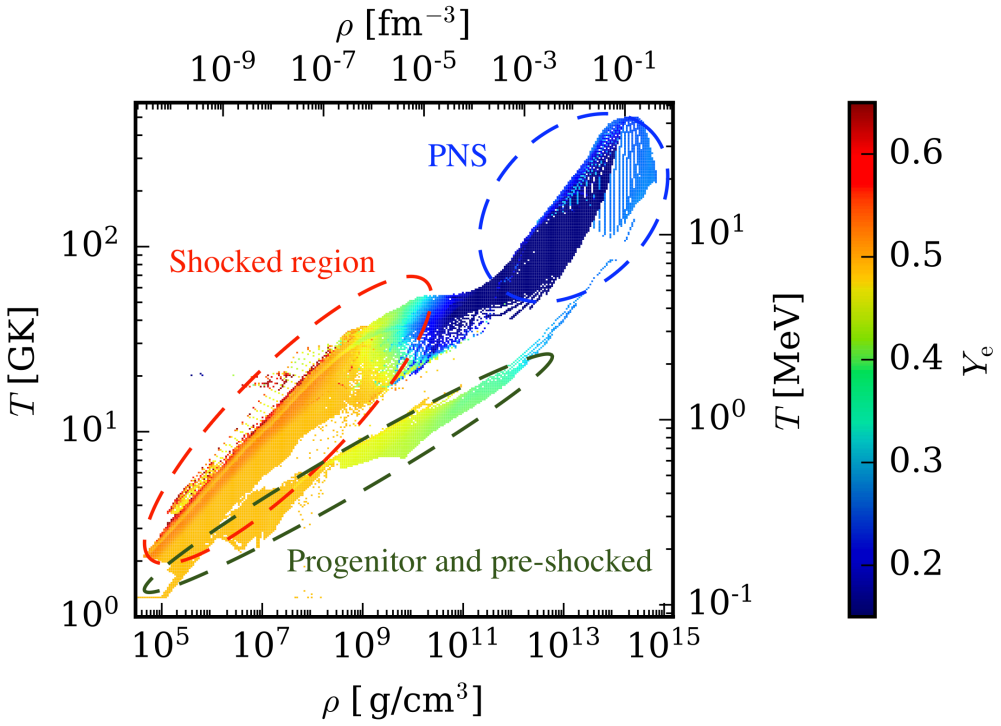

Figure 3.2: Thermodynamic conditions reached in a representative CCSN simulation. Colorcoded the Y_e at a given $\rho - T$ condition.

Using the thermodynamic identity

$$\left(\frac{\partial(\beta F)}{\partial \beta}\right)_{V,N} = U, \tag{3.54}$$

we obtain a relation with the Helmholtz free energy F, from which all thermodynamic quantities can be derived,

$$F(\beta, V, N) = -\frac{1}{\beta} \ln Z(\beta). \tag{3.55}$$

For example, the pressure P, the entropy S, and the chemical potential μ read

$$P = -\left(\frac{\partial F}{\partial V}\right)_{T,N} \quad S = -\left(\frac{\partial F}{\partial T}\right)_{V,N} \quad \mu = -\left(\frac{\partial F}{\partial N}\right)_{T,V}. \tag{3.56}$$

3.3.2 Thermodynamic conditions in CCSNe

The thermodynamic conditions in CCSNe are very diverse (see Figure 3.2). As mentioned in Section 2.2, the inner part of the core eventually reaches ρ_0 and the matter

experiences a phase transition from inhomogeneous to homogeneous matter. In this region, the PNS is formed and achieves very high densities, up to $\rho \sim 10^{15}\,\mathrm{g\,cm^{-3}}$, and temperatures, $T > 100\,\mathrm{GK}$. On the outskirts, the matter gets heated by the shock and the densities tend to decrease. Overall, we observe temperatures and densities that encompass several orders of magnitude. Thus, to build EOSs that are suitable for all these conditions simultaneously is very challenging, since the different EOSs are usually devoted to a specific regime and only employ the most relevant physics.

The EOS considers baryons, leptons, and radiation in local thermal equilibrium. Neutrinos are only trapped inside the PNS, and, therefore, EOS do not include them. This is one of the reasons why CCSN simulations employ a neutrino transport scheme (see Section 3.2).

3.3.3 Helmholtz EOS

At low densities, i.e., $\rho \lesssim 10^{11}\,\mathrm{g\,cm^{-3}}$, the system consists of inhomogeneous matter and the strong interaction can be neglected. In this regime, matter can be described by a so-called Helmholz EOS (see, e.g., Timmes & Arnett, 1999; Timmes & Swesty, 2000), which considers a plasma made of ions, electrons, positrons, and radiation:

$$F = F_{\mathrm{ion}} + F_{\mathrm{e^-}} + F_{\mathrm{e^+}} + F_{\mathrm{rad}}, \tag{3.57}$$

The ion contribution is treated as an ideal gas:

$$P_{\mathrm{ion}} = N_{\mathrm{ion}} k_{\mathrm{B}} T, \quad E_{\mathrm{ion}} = \frac{3}{2}\frac{P_{\mathrm{ion}}}{\rho}, \tag{3.58}$$

where N_{ion} is the ion number density.

The radiation contribution considers blackbody emission in local thermodynamic equilibrium:

$$P_{\mathrm{rad}} = \frac{4}{3}\frac{\sigma T^4}{c}, \quad E_{\mathrm{rad}} = \frac{3P_{\mathrm{rad}}}{\rho}. \tag{3.59}$$

Finally, the free electron and positron contributions are considered as a non-interacting Fermi gas. For a complete derivation see, e.g., Timmes & Arnett (1999); Timmes & Swesty (2000). For example, P_{e^-} and E_{e^-} take the form

$$\begin{aligned} P_{e^-} &\propto (k_{\mathrm{B}}T)^{5/2}\left[F_{3/2}(\mu,T) - \frac{1}{2}k_{\mathrm{B}}TF_{5/2}(\mu,T)\right], \\ E_{e^-} &\propto \frac{(k_{\mathrm{B}}T)^{5/2}}{\rho}\left[F_{3/2}(\mu,T) - k_{\mathrm{B}}TF_{5/2}(\mu,T)\right]. \end{aligned} \tag{3.60}$$

$F_{3/2}(\mu,T)$ and $F_{5/2}(\mu,T)$ are Fermi-Dirac integrals, which are costly to solve. Thus, CCSNe simulations use tables in which these contributions are already provided.

AENUS-ALCAR used to employ a Helmholtz EOS at densities $\rho \leq \rho_{\mathrm{th}} \sim 10^{7-8}\,\mathrm{g/cm^3}$. In Section 4.3.3, we introduce a novel, and more complex, transition that substitutes the density criterion for a temperature one.

3.3.4 EOS of dense matter

Beyond nuclear saturation density, the matter is homogeneous or uniform, i.e., it is made of neutrons and protons, and electrons. In this density regime, the density is defined as the sum of neutrons and protons, $n = n_n + n_p$. We can expand the energy per particle E/A in terms of an assymetry parameter β. Following, e.g., Huth et al. (2021):

$$\beta = \frac{n_n - n_p}{n}, \tag{3.61}$$

$$\frac{E}{A}(n, \beta) = \frac{E}{A}(n, 0) + S(n)\beta^2 + \mathcal{O}(\beta^3) \tag{3.62}$$

$\beta = 0$ corresponds to symmetric nuclear matter (SNM), and $\beta = 1$ to pure neutron matter (PNM). $S(n)$ is the symmetry energy, which is defined as

$$S(n) \equiv \frac{E}{A}(n, 1) - \frac{E}{A}(n, 0) \tag{3.63}$$

In addition, we can further expand E/A around the nuclear saturation density (n_0):

$$\eta = \frac{n - n_0}{3n}, \tag{3.64}$$

$$\frac{E}{A}(\eta, \beta) = -B + \frac{1}{2}K\eta^2 + (E_{\rm sym} + L\eta)\beta^2 + \mathcal{O}(\eta^3) + \mathcal{O}(\beta^3). \tag{3.65}$$

B is the binding energy of SNM. $E_{\rm sym}$ is the symmetry energy coefficient (see Figure 3.3). L is the slope parameter, and K the incompressibility:

$$L = 3n_0 \left.\frac{\partial S}{\partial n}\right|_{n_0} = \frac{3}{n_0}P(n_0, \beta = 1), \quad K = 9n_0^2 \left.\frac{\partial^2 E/A}{\partial n^2}\right|_{n_0,\beta=0} = 9 \left.\frac{\partial P}{\partial n}\right|_{n_0,\beta=0} \tag{3.66}$$

The parameters introduced above characterize nuclear matter properties. They can be constrained by theoretical calculations based on chiral effective field theory (EFT) (e.g., Hebeler et al., 2013; Tews et al., 2013), nuclear experiments such measuring the neutron skin of the lead (Reed et al., 2021) or heavy ion collision experiments (e.g., Le Fèvre et al., 2016), and observations of astrophysical processes such gravitational waves (GW) (Abbott et al., 2017) or pulsars (Antoniadis et al., 2013; Miller et al., 2019; Raaijmakers et al., 2020).

However, they are not able to characterize the full range of thermodynamic conditions discussed in Section 3.3.2. Hence, EOS devoted to astrophysical processes are based on phenomenological models. In the following we briefly introduce two of the most widely used in the community. They are provided in tables where the quantities are tabulated as a function of ρ, T, and Y_e. AENUS-ALCAR, in particular, employs these EOS tables for matter at high densities ($\rho > \rho_{\rm th}$).

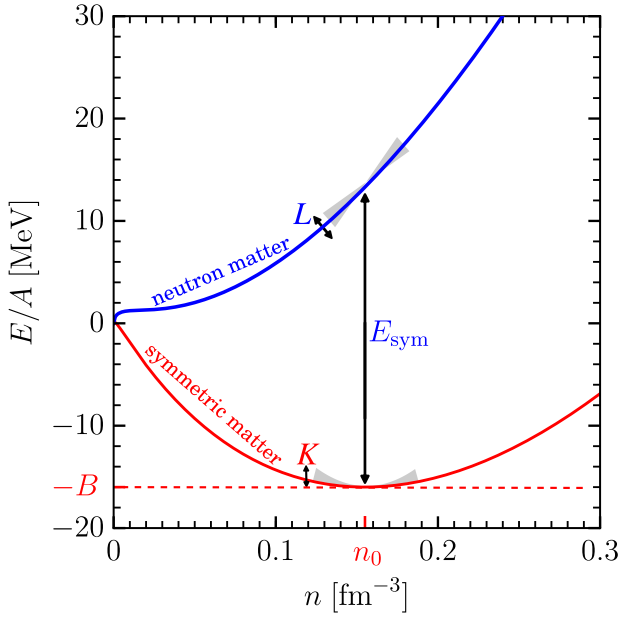

Figure 3.3: Schematic decomposition of E/A on PNM and SNM. In addition, The nuclear matter parameters are represented. Courtesy of Sabrina Huth.

Skyrme models

Skyrme models are based on a non-relativistic, self-consistent mean-field approximation (Skyrme, 1956, 1958). The most popular is the Lattimer-Swesty (LS) EOS (Lattimer & Swesty, 1991). Under this assumption, matter contains free nucleons, electrons, positrons, photons, alpha particles, and commonly a characteristic nucleus, in the so-called single nucleus approximation (SNA). In SNA, the distribution of nuclei in the system is approximated by a single representative nucleus with mass number A and atomic number Z. In addition, the nucleus is described by the liquid drop model first proposed by Gamow (1930). It approaches the nucleus as a drop of an uniformly charged incompressible fluid where the strong interaction keeps its protons and neutrons together.

The energy-density functional (EDF) relates the energy per nucleon of homogeneous nuclear matter to the particle density n and the proton fraction $x = n_p/n$. In the LS EOS, it reads (Lattimer & Swesty, 1991):

$$E(n,x,T) = \sum_t \frac{\hbar^2 \tau_t(n,x,T)}{2m_t^*} + [a + 4bx(1-x)]n^2 + cn^{1+\delta} - x\Delta, \tag{3.67}$$

where the index t indicates the isospin (p or n), τ_t is the nucleon kinetic energy density, and a, b, c, and δ are the Skyrme parameters, which values are fit applying the nuclear

matter properties introduced above. The second term in Equation (3.67) contains the two-body interactions, the third takes into account many-body effects, and the last term considers the mass difference between neutrons and protons. The first term corresponds to the non-relativistic kinetic energy, which includes the thermal contribution to the EOS at finite temperatures. This is well depicted by the thermal index, $\Gamma_{\rm th}$. It has been shown that it can be determined by the density dependent nucleon effective mass m^* (see, e.g., Constantinou et al., 2015a; Yasin et al., 2020).

$$\Gamma_{\rm th} = \frac{5}{3} - \frac{n}{m^*}\frac{\partial m^*}{\partial n}. \tag{3.68}$$

The nucleon effective mass m^* is defined as

$$\frac{\hbar^2}{2m_t^*} = \frac{\hbar^2}{2m_t} + \alpha_1 n_p + \alpha_2 n_n, \tag{3.69}$$

where α_1 and α_2 are fit at saturation density n_0.

In Chapter 6 we show the impact of new EOSs in CCSNe, built with the new effective mass parameterization and the new EDF based on Huth et al. (2021).

Relativistic mean field models

Relativistic mean field (RMF) models are also widely used in the community. They consider the nucleon interaction via mesons exchange (Yukawa, 1935). There are many RMF EOS, which adopt different parameterizations of the RMF Lagrangian (Serot & Walecka, 1986). They include the same constituents as the Skyrme based EOS and also commonly use the SNA approximation. However, they use the Thomas Fermi approximation to describe inhomogeneous matter (Oyamatsu, 1993) . A common used one is the HShen EOS (Shen et al., 1998), which is based on TM1 parameter set (Sugahara & Toki, 1994). In Chapter 5, we perform our simulations with the SFHo EOS (Steiner et al., 2013), whose parameters are constrained by NS mass and radius observations.

3.4 Composition treatment

In the hydrodynamic equations, the partial densities (ρX_k) are conserved variables of the system (Equation (3.9)). In addition, the composition is an input for the opacities (Section 3.2.2) and the EOS (see Section 3.3), while the neutron richness in the environment determines the Y_e of the system. Thus, the composition is an important ingredient for the simulations.

If the temperature is high ($T \gtrsim 0.5\,\mathrm{MeV} \simeq 5.8\,\mathrm{GK}$), the matter is in chemical equilibrium, i.e., the rate of production and destruction of nuclei is equal, and, therefore, the matter is in NSE and the composition is usually calculated in the EOS table

(Section 3.4.1). In contrast, if the temperature drops $T \sim 0.5\,\mathrm{MeV}$, matter cannot be considered in NSE and the nuclear reactions become important. Their impact, as well as their treatment, in CCSNe simulations is studied in Chapter 5. However, as we will show in Chapter 4, taking into account nuclear reactions properly in the simulations is computationally very expensive. Therefore, CCSNe simulations usually employ simplified treatments that take them into account in an approximate way. This was the case in AENUS-ALCAR that, prior to the inclusion of the network module (Chapter 4), used the so-called flashing scheme (Rampp & Janka, 2002). We briefly introduce it in Section 3.4.2.

3.4.1 NSE

If temperatures are high enough ($T \gtrsim 5 - 6\,\mathrm{GK}$), fusion reactions and photodisintegrations are in so called NSE (see, e.g., Hix & Thielemann, 1999; Arcones et al., 2010). Within this equilibrium, the production rate of a specific nuclear species equals its destruction rate and for constant thermodynamic conditions the composition is also constant over time (neglecting weak reactions):

$$(A-Z)N \cdot n + Z \cdot p \rightleftharpoons X(N,Z) + \gamma, \tag{3.70}$$

Where A is the mass number and Z the atomic number of the nucleus $X(Z,A)$. In terms of chemical potentials, it reads

$$\mu_{(Z,A)} = Z\mu_p + (A-Z)\mu_n. \tag{3.71}$$

Assuming Maxwell-Boltzmann statistics, the chemical potential of a nucleus i is

$$\mu_i = m_i c^2 + k_\mathrm{B} T \ln\left(\frac{\rho N_\mathrm{A} Y_i}{G_i}\left(\frac{2\pi\hbar^2}{k_\mathrm{B} T m_i}\right)^{3/2}\right). \tag{3.72}$$

m_i is the mass of the nucleus and G_i is the partition function. Y_i is the abundance, which relates with the mass fraction X_i as

$$X_i = \frac{\rho_i}{\rho} = \frac{n_i}{\rho N_\mathrm{A}} m_i N_\mathrm{A} = Y_i A_i, \tag{3.73}$$

where n_i is the number density.

From Equations (3.71) and (3.72), we obtain the composition in NSE:

$$Y_i = G_i(T)\left(\frac{\rho}{m_u}\right)^{A_i-1}\frac{A_i^{3/2}}{2^{A_i}}\left(\frac{2\pi\hbar^2}{k_B T m_u}\right)^{3(A_i-1)/2} Y_n^{N_i} Y_p^{Z_i} e^{B_i/k_B T} e^{Z_i\mu_{c,p} - \mu_{C,(Z_i,A_i)}} \tag{3.74}$$

In addition, mass and charge must be conserved:

$$\sum_i X_i = 1 \quad \sum_i Y_i \cdot Z_i = Y_e. \tag{3.75}$$

Therefore, from Equation (3.74), in NSE the abundances are direct functions of the density, temperature, and electron fraction (Y_e),

$$Y = Y(\rho, T, Y_e). \tag{3.76}$$

Thus, the NSE composition in the simulation is usually provided in a tabulated form. It is often included within the EOS table (see Section 3.3.4), to replace the much more accurate SNA composition. Hence, in Chapter 5, we employ the SFHo EOS determined in NSE.

3.4.2 Flashing scheme

For the matter that is not in NSE, AENUS-ALCAR uses a version of the so-called flashing scheme to compute the composition. It is used at $\rho \leq \rho_{\rm th}$ and provides the input for the ionic contribution of Helmholtz EOS.

The flashing scheme, introduced in Rampp & Janka (2002), takes into account neutrons, protons, alpha particles (not included in the implementation in AENUS-ALCAR), and a characteristic nucleus. The latter is either ^{28}Si or ^{56}Ni, depending on the thermodynamic conditions, and considering instantaneous burning. When silicon burning occurs at $T \sim 4.5\,\mathrm{GK}$, the silicon mass fraction ($X(^{28}\mathrm{Si})$) is immediately transformed to ^{56}Ni and set to $X(^{28}\mathrm{Si}) = 0$.

While the composition assumed by the flashing scheme is only a rough approximation, this scheme implicitly accounts for the generation or consumption of nuclear energy by the instantaneous burning between the nuclei that is assumed to happen at the threshold temperature.

In Chapter 4, we have included a nuclear reaction network module to describe the composition outside of the NSE regime more accurately.

4 Reduced network implementation in Aenus-Alcar

Nuclear reaction networks (Section 4.1) evolve the abundances of a set of N species by a system of N coupled ordinary differential equations including all the reactions between the species. In CCSNe, it can include of the order of several hundred nuclei (e.g., Woosley & Weaver, 1995; Rauscher et al., 2002). Thus, including nuclear reaction networks in multidimensional CCSNe simulations is very challenging because of the computational cost of evolving them together with the hydrodynamics. Therefore, hydrodynamic simulations usually employ a simple treatment of the composition. A detailed nucleosynthesis can be obtained by post-processing using Lagrangian tracer particles that follow the thermodynamic record of the fluid.

Out of NSE, then, simplified treatments are used. An alternative to the flashing scheme (Section 3.4.2) is to use reduced reaction networks (e.g., Müller, 1986; Hix & Thielemann, 1999; Timmes et al., 2000) in order to track a small set of nuclei together with the hydrodynamics. The nuclei considered are chosen to involve the main reactions that release or consume internal energy and to represent the main contributions to the baryonic part of the pressure and neutrino opacities (Cernohorsky & van Weert, 1992). In practice, α-chains are the most commonly used for this purpose.

In this chapter, we derive the network equations (Section 4.1), and introduce the reduced network code developed by M. Reichert (Reichert, 2016) (Section 4.2). In (Section 4.3), we describe its implementation in Aenus-Alcar. This part is partially adapted from Navó et al. (2023). We start by introducing the networks that we included (Section 4.3.1), and showing their strengths and weaknesses (Section 4.3.2). In Section 4.3.3, we focus on the coupling to the hydrodynamics, and, in Section 4.3.4, we demonstrate its proper performance.

4.1 Nuclear Reaction Network

A nuclear reaction network evolves abundances,and it size depends on the nature of the environment.

4.1.1 Equations

In the following, we derive the set of differential equations that we need to solve to take into account the nuclear reactions present in the medium, which has been extensively discussed in the literature (e.g., Clayton, 1968; Hix & Thielemann, 1999; Hix & Meyer, 2006; Lippuner & Roberts, 2017; Reichert et al., 2023).

We start with the reaction rate r, which is the number of reactions per volume and time. For the reaction $i + j \rightarrow k + l$, it reads

$$r_{i,j} = \frac{1}{1+\delta_{i,j}} n_i n_j \langle \sigma\nu \rangle_{i,j}. \tag{4.1}$$

$\langle \sigma\nu \rangle_{i,j}$ is the velocity averaged cross section, which can be seen as the probability the interaction between i and j has to occur. The term $1 + \delta_{i,j}$ in the denominator is the correction factor to avoid double counting when $i = j$. Analogously, for a three-body interaction, the reaction rate is

$$r_{i,j,k} = \frac{1}{1+\Delta_{i,j,k}} n_i n_j n_k \langle \sigma\nu \rangle_{i,j,k}. \tag{4.2}$$

The reaction rates can be also defined as the time variation of the number densities. For the $i + j \rightarrow k + l$ reaction:

$$r_{i,j} = -\left(\frac{\partial n_i}{\partial t}\right)_\rho = -\left(\frac{\partial n_j}{\partial t}\right)_\rho = \left(\frac{\partial n_k}{\partial t}\right)_\rho = \left(\frac{\partial n_l}{\partial t}\right)_\rho. \tag{4.3}$$

Therefore, the time derivative of the number density of a certain specie i is given by the sum of all reactions that contribute to its production or destruction:

$$\left(\frac{\partial n_i}{\partial t}\right)_\rho = \sum_j N^i_j r_j + \sum_{j,k} \frac{N^i_{j,k}}{1+\delta_{j,k}} r_{j,k} + \sum_{j,k,l} \frac{N^i_{j,k,l}}{1+\Delta_{j,k,l}} r_{j,k,l}, \tag{4.4}$$

where the first term corresponds to photodisintegrations and decays, the second term to two-body reactions and the third term to three-body reactions. Finally, introducing the time derivative of the abundance Y_i,

$$\dot{Y}_i = \frac{\dot{n}_i}{\rho N_\mathrm{A}} - \frac{n_i}{\rho N_\mathrm{A}} \frac{\dot{\rho}}{\rho}, \tag{4.5}$$

we get the set of ordinary differential equations:

$$\dot{Y}_i = \sum_j N^i_j \lambda_j Y_j + \sum_{j,k} \frac{N^i_{j,k}}{1+\delta_{j,k}} \rho N_\mathrm{A} \langle \sigma\nu \rangle_{j,k} Y_j Y_k + \sum_{j,k,l} \frac{N^i_{j,k,l}}{1+\Delta_{j,k,l}} \rho^2 N^2_\mathrm{A} \langle \sigma\nu \rangle_{j,k,l} Y_j Y_k Y_l. \tag{4.6}$$

In addition, we can obtain the energy released by the nuclear reactions making use of $E = mc^2$. The total mass of the system is $m = V \sum_i n_i m_i$, so the energy released is

$$\dot{E} = -V \sum m_i \dot{n}_i. \tag{4.7}$$

Applying Equation (3.73) we get the expression in terms of the abundance variation. It is usually given per unit of volume,

$$\dot{\varepsilon}_{\mathrm{nuc}} = -N_{\mathrm{A}}\rho \sum_i m_i c^2 \dot{Y}_i, \tag{4.8}$$

or per unit of matter,

$$\dot{\varepsilon}_{\mathrm{nuc}} = -N_{\mathrm{A}} \sum_i m_i c^2 \dot{Y}_i. \tag{4.9}$$

In Chapter 5 we study the impact of the nuclear energy generation on the CCSNe evolution.

4.1.2 Numeric integration

If we consider a system with N species, Equation (4.6) constitutes a set of N coupled ordinary differential equations including all the reactions between the species,

$$\frac{\mathrm{d}\mathbf{y}}{\mathrm{d}t} = \mathbf{f}(t, \mathbf{y}). \tag{4.10}$$

It is an initial value problem, which means that $\mathbf{y}(t_0) = \mathbf{y_0}$ must be known. In our case, $\mathbf{y_0}$ correspond to the initial abundances.

The reaction rates included in Equation (4.6) encompass many orders of magnitude, as well as the abundances (e.g., Hix & Thielemann, 1999). Hence, it is common that parts of the system change rapidly in time while others do it in comparison orders of magnitude slower. This broad range of timescales makes the system stiff (e.g., Hix & Thielemann, 1999). Stiff systems are limited by numerical stability rather than accuracy and have to be solved implicitly (for an overview, e.g., see Butcher, 2003; Rapp, 2017). In the following we present the implicit Euler method, one of the simplest yet numerical stable methods.

We can express the change in any function $f(x)$ when x is infinitesimally increased by Δx with a Taylor expansion:

$$f(x - \Delta x) = \sum_{n=0}^{n_{\max}} (-1)^n \frac{1}{n!} \frac{\mathrm{d}^n f}{\mathrm{d}x^n} (\Delta x)^n + \mathcal{O}_{n,\max+1}. \tag{4.11}$$

The Euler method is a first-order method, i.e. $n_{\max} = 1$. Hence,

$$f(x - \Delta x) \approx f(x) - \Delta x \frac{\mathrm{d}f}{\mathrm{d}x}(x). \tag{4.12}$$

We can evaluate Equation (4.12) at $x_{i+1} = x_i + \Delta x$,

$$f(x_i - \Delta x + \Delta x) = f(x_i + \Delta x) - \Delta x \frac{\mathrm{d}f}{\mathrm{d}x}(x_i + \Delta x),$$

$$f(x_i) = f(x_{i+1}) - \Delta x \frac{\mathrm{d}f}{\mathrm{d}x}(x_{i+1}), \tag{4.13}$$

and translate it to our case of interest:

$$\mathbf{y}_{n+1} = \mathbf{y}_n + h\frac{\mathrm{d}\mathbf{y}_{n+1}}{\mathrm{d}t} = \mathbf{y}_n + h\mathbf{f}(t_{n+1}, \mathbf{y}_{n+1}), \tag{4.14}$$

where, t_{n+1} and t_n are two consecutive timesteps $t_{n+1} = t_n + h$. Note that implicit methods imply that the solution in the future timestep $\mathbf{y}_{n+1}$ is present in both sides of Equation (4.14). To solve it, we can put all terms in the same side of the equation,

$$\frac{\mathbf{y}_{n+1} - \mathbf{y}_n}{h} - \mathbf{f}(t_{n+1}, \mathbf{y}_{n+1}) = 0, \tag{4.15}$$

and apply a Newton-Raphson solver to find the root (e.g., Butcher, 2003):

$$\mathbf{y}_{n+1}^{m+1} = \mathbf{y}_{n+1}^{m} - \mathbf{J}^{-1} \cdot \left(\frac{\mathbf{y}_{n+1}^{m} - \mathbf{y}_n}{h} - \dot{\mathbf{y}}_{n+1}^{m} \right), \tag{4.16}$$

where the super-indices m and $m+1$ indicate the Newton-Raphson iteration, $\dot{\mathbf{y}} = \frac{\mathrm{d}\mathbf{y}}{\mathrm{d}t}$, and $\mathbf{J}^{-1}$ is the invert of Jacobian of the system,

$$J_{ij} = \frac{1}{h} - \frac{\partial \dot{y}_{i,n+1}^{m}}{\partial y_{j,n+1}^{m}}, \tag{4.17}$$

which is the most computationally expensive part. This method iterates until a convergence criterion is fulfilled. For example, when the mass conservation is satisfied,

$$\mid 1 - \sum_i X_i \mid < \epsilon \sim 10^{-5} - 10^{-6}. \tag{4.18}$$

4.2 ReNet

RENET (Reichert, 2016) is an adaptable nuclear reaction network code that performs abundance flow calculations for networks of various sizes and complexity levels.

This section is based on Reichert (2016); Navó et al. (2023), where RENET is introduced.

RENET implicitly solves the set of differential equations in a similar way of previous works in the literature (e.g., Müller, 1986; Hix & Thielemann, 1999; Timmes et al., 2000). It employs a first order implicit Euler method as integration scheme (as described in e.g., Hix & Thielemann, 1999; Lippuner & Roberts, 2017). Identically to Lippuner & Roberts (2017), the iterative Newton-Raphson scheme converges when mass conservation is fulfilled (Equation (4.18)). The thermodynamic quantities in the next time step are unknown in in-situ reaction networks, in contrast to post-processing ones. As a result, RENET computes the composition at a constant temperature and density at the current time step. RENET includes the option of using sparse matrices

that help minimise the computing cost of nuclear networks with more than ~ 300 nuclei (e.g., Hix & Thielemann, 1999; Lippuner & Roberts, 2017; Reichert, 2016). Nevertheless, for the reduced reaction networks that will be discussed in this work, solvers for dense matrices are best suited (LAPACK, Anderson et al. (1999)).

ReNet is able to assume species in steady state,

$$\frac{\mathrm{d}Y_i}{\mathrm{d}t} = 0, \tag{4.19}$$

which allows to neglect the differential equation involving these nuclei. This strategy was already applied in other reduced networks such as, e.g., the aprox13 (Timmes, 1999), aprox19 (Weaver et al., 1978), and aprox21 (Paxton et al., 2011). As an example of this approximation, we consider (p,γ) reactions among three nuclei ^{54}Fe, ^{55}Co, and ^{56}Ni (see Figure 4.1 for a schematic representation). The reaction equations are

$$\frac{\mathrm{d}Y(^{54}\mathrm{Fe})}{\mathrm{d}t} = -Y(^{54}\mathrm{Fe})Y(\mathrm{p})\lambda_1 + Y(^{55}\mathrm{Co})\lambda_2 \tag{4.20}$$

$$\frac{\mathrm{d}Y(^{55}\mathrm{Co})}{\mathrm{d}t} = Y(^{54}\mathrm{Fe})Y(\mathrm{p})\lambda_1 - Y(^{55}\mathrm{Co})\lambda_2 - Y(^{55}\mathrm{Co})Y(p)\lambda_3 + Y(^{56}\mathrm{Ni})\lambda_4 \tag{4.21}$$

$$\frac{\mathrm{d}Y(^{56}\mathrm{Ni})}{\mathrm{d}t} = Y(^{55}\mathrm{Co})Y(p)\lambda_3 - Y(^{56}\mathrm{Ni})\lambda_4, \tag{4.22}$$

If now we assume ^{55}Co in steady state, i.e.,

$$\frac{\mathrm{d}Y(^{55}\mathrm{Co})}{\mathrm{d}t} = 0, \tag{4.23}$$

we obtain

$$Y(^{55}\mathrm{Co}) = \frac{Y(^{54}\mathrm{Fe})Y(\mathrm{p})\lambda_1 + Y(^{56}\mathrm{Ni})\lambda_4}{\lambda_2 + Y(\mathrm{p})\lambda_3} \tag{4.24}$$

$$Y(^{54}\mathrm{Fe})Y(\mathrm{p})\lambda_1 = Y(^{55}\mathrm{Co})\lambda_2 + Y(^{55}\mathrm{Co})Y(\mathrm{p})\lambda_3 - Y(^{56}\mathrm{Ni})\lambda_4. \tag{4.25}$$

Inserting Equation (4.25) to Equation (4.20), we get

$$\begin{aligned}
\frac{\mathrm{d}Y(^{54}\mathrm{Fe})}{\mathrm{d}t} &= -Y(^{55}\mathrm{Co})Y(\mathrm{p})\lambda_3 + Y(^{56}\mathrm{Ni})\lambda_4 \qquad (4.26)\\
&= -Y(\mathrm{p})\lambda_3\frac{Y(^{54}\mathrm{Fe})Y(\mathrm{p})\lambda_1 + Y(^{56}\mathrm{Ni})\lambda_4}{\lambda_2 + Y(\mathrm{p})\lambda_3} + Y(^{56}\mathrm{Ni})\lambda_4\\
&= -Y(\mathrm{p})Y(\mathrm{p})Y(^{54}\mathrm{Fe})\frac{\lambda_3\lambda_1}{\lambda_2 + Y(\mathrm{p})\lambda_3} - Y(\mathrm{p})Y(^{56}\mathrm{Ni})\frac{\lambda_3\lambda_4}{\lambda_2 + Y(\mathrm{p})\lambda_3} + Y(^{56}\mathrm{Ni})\lambda_4\\
&= -Y(\mathrm{p})Y(\mathrm{p})Y(^{54}\mathrm{Fe})\frac{\lambda_3\lambda_1}{\lambda_2 + Y(\mathrm{p})\lambda_3} + Y(^{56}\mathrm{Ni})\frac{\lambda_2\lambda_4}{\lambda_2 + Y(\mathrm{p})\lambda_3},
\end{aligned}$$

and analogously for Equation (4.22)

$$\frac{\mathrm{d}Y(^{56}\mathrm{Ni})}{\mathrm{d}t} = Y(\mathrm{p})Y(\mathrm{p})Y(^{54}\mathrm{Fe})\frac{\lambda_3\lambda_1}{\lambda_2 + Y(\mathrm{p})\lambda_3} - Y(^{56}\mathrm{Ni})\frac{\lambda_2\lambda_4}{\lambda_2 + Y(\mathrm{p})\lambda_3}. \tag{4.27}$$

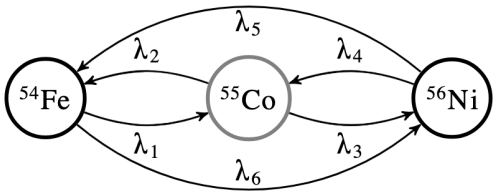

Figure 4.1: Conceptual view of the steady state approximation. The arrows illustrate the different rates (λ_1,λ_2,λ_3,λ_4) involving ^{54}Fe, ^{55}Co and ^{56}Ni. The rates λ_5 and λ_6 are obtained the steady state assumption. (Reichert, 2016)

Equations (4.26) and (4.27) constitute the equations for the $^{54}\mathrm{Fe}(2\mathrm{p},\gamma)^{56}\mathrm{Ni}$ reaction, which implicitly accounts for $^{54}\mathrm{Fe}(\mathrm{p},\gamma)^{55}\mathrm{Co}$ and $^{55}\mathrm{Co}(\mathrm{p},\gamma)^{56}\mathrm{Ni}$ and eliminates the necessary time evolution of $Y_{^{55}\mathrm{Co}}$. The resulting rates can be deduced from Equations (4.26) and (4.27),

$$\lambda_5 = \frac{\lambda_2\lambda_4}{\lambda_2 + Y(\mathrm{p})\lambda_3}, \tag{4.28}$$

$$\lambda_6 = \frac{\lambda_3\lambda_1}{\lambda_2 + Y(\mathrm{p})\lambda_3} \tag{4.29}$$

We applied this procedure to a series of nuclei using the SYMPY Python package to derive the equations and the Jacobian analytically. The latter is necessary because proton or neutron abundances can end up in the denominator when we include all reactions that go through the steady-state nucleus. In this way, we are able to evolve a large region of the nuclear chart without explicitly evolving the abundance of all nuclei.

4.3 ReNet implementation in Aenus-Alcar

4.3.1 Networks included

We implemented two reaction network configurations into AENUS-ALCAR: a 16-α chain (RN16) and a 94-species network (RN94). RN16 is similar to the widely used 19 isotope approximation network from Weaver et al. (1978), which approximately reproduces the nuclear energy generation within CCSNe simulations and therefore provides feedback to the total energy of the system. RN94 is able to track the main species synthesized in the CCSNe (c.f., Eichler et al., 2017; Harris et al., 2017), with Y_e between 0.4 and 0.6. Hence, it allows us to track slightly neutron and proton rich trajectories along stability up to ^{92}Mo. In addition, 148 species are considered in steady state, reproducing a network consisting of 242 nuclei. Therefore, we present, at the time of writing, the most complete network evolved in CCSN simulations with

n	^{1}H	^{4}He	^{12}C	^{16}O	^{20}Ne	^{24}Mg ^{27}Al†	^{28}Si	^{31}P†	^{32}S
^{35}Cl†	^{36}Ar	^{39}K†	^{40}Ca	^{43}Sc†	^{44}Ti	^{47}V†	^{48}Cr	^{51}Mn†	^{52}Fe
^{53}Fe†	^{54}Fe	^{55}Co†	^{56}Ni						

Table 4.1: RN16 Network. List of RN16 nuclei . Steady state nuclei are marked with a dagger.

n	^{1}H	^{4}He	^{12}C	^{16}O	^{20}Ne
^{23}Mg†	^{24}Mg	^{27}Al†	^{28,30}Si	^{27,29}Si†	^{29,31}P†
$^{30-34}$S	^{31,33}S†	^{33,35}Cl†	$^{34-38}$Ar	^{35,37}Ar†	^{37,39}K†
$^{38-42,48-52}$Ca	^{39,41,49,51}Ca†	$^{41,43,49-55}$Sc†	$^{42-56}$Ti	$^{43-55}$Ti†	$^{45-57}$V†
$^{46-58}$Cr	$^{47-57}$Cr†	$^{49-61}$Mn†	$^{50-64}$Fe	$^{51-63}$Fe†	$^{53-67}$Co†
$^{54-70}$Ni	$^{55-69}$Ni†	$^{61-73}$Cu†	$^{60-74}$Zn	$^{59-73}$Zn†	$^{63-77}$Ga†
$^{64-80}$Ge	$^{65-79}$Ge†	$^{67-83}$As†	$^{68-84}$Se	$^{69-83}$Se†	$^{75-85}$Br†
$^{76-86}$Kr	$^{77-85}$Kr†	$^{79-87}$Rb†	$^{80-88}$Sr	$^{81-87}$Sr†	$^{85-89}$Y†
$^{86-90}$Zr	^{87,89}Zr†	^{91}Nb†	^{92}Mo		

Table 4.2: RN94 Network. List of RN94 nuclei . We use the ^{i-j}X notation to account for the species in $\{^{i}X, ^{i+2}X, ..., ^{j}X\}$.

state-of-the-art M1 neutrino transport. The species included in both networks are listed in Table 4.1 and Table 4.2.

4.3.2 RN16 and RN94 performance

In this section we prove the reliability of ReNet. It is based on the Appendix of Navó et al. (2023).

We test RN16 and RN94 in three characteristic CCSNe explosive trajectories: One slightly neutron-rich ($Y_{e,5.8\,\mathrm{GK}} \sim 0.48$), one is symmetric ($Y_{e,5.8\,\mathrm{GK}} \sim 0.50$), and one slightly proton-rich ($Y_{e,5.8\,\mathrm{GK}} \sim 0.51$). We compare them with other two networks. On the one hand, we built a network of ~ 800 species with ReNet, which includes all relevant nuclei up to Ge. Nevertheless, it does not include weak reactions, since in CCSNe the nuclear flow evolves relatively close to stability and β-decays are slow. In the following, we refer to it as the "full network" ReNet. On the other hand, we employ the also full reaction network WinNet (Winteler et al., 2012; Reichert et al., 2023), which is used in many works in the literature (e.g., Winteler et al., 2012; Korobkin et al., 2012; Martin et al., 2015; Eichler et al., 2019; Bliss et al., 2020; Reichert et al., 2021; Ristic et al., 2022).

As expected, WinNet and ReNet show an excellent agreement in the nuclear energy generated and the final abundance pattern (Figure 4.3). In Figure 4.3 we compare the nuclear energy generation for the three different trajectories. For the

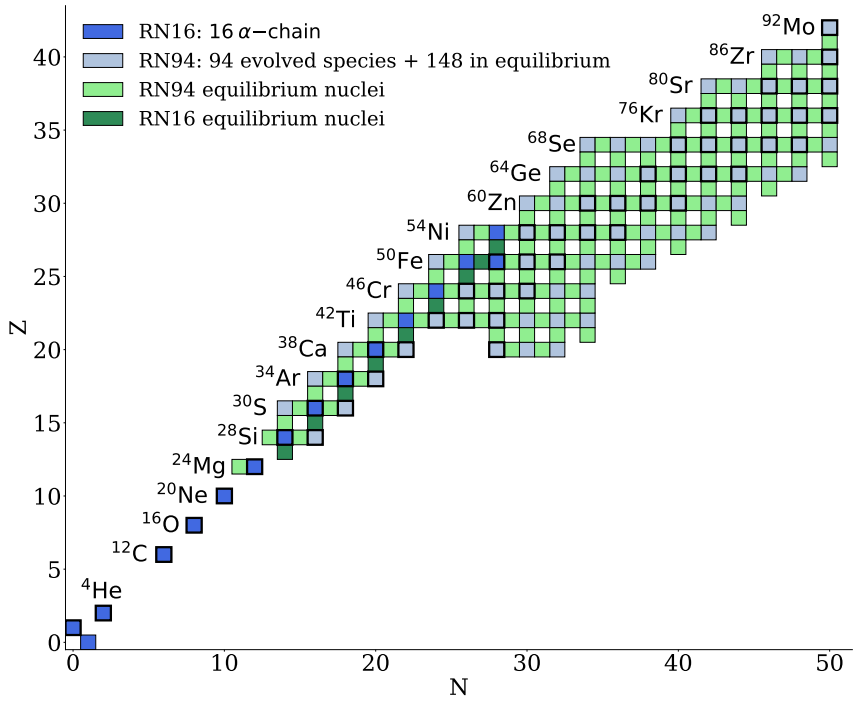

Figure 4.2: Nuclear chart diagram with the species included in RN16 and RN94. Highlighted in black the stable nuclei.

slightly proton rich and the symmetric trajectories, the energy generation of all nuclear reaction networks is in a great agreement. We observe some times where the total nuclear energy released is negative in the full network and in WINNET. However this behavior is not captured at all by RN16, and very roughly by RN94, which only reproduces one of these episodes. This negative released energy comes from a strong contribution of (γ, p) reactions, which are not included in RN16. In RN94 there are (γ, p) reactions included, but restricted to the nuclei considered. Therefore, the differences come from (γ, p) reactions on species that are not included in RN94. Finally, we observe a larger discrepancy of the energy generation of RN16 with respect to the other networks in the slightly neutron rich trajectory, since RN16 forces the nuclear flow to stay in symmetric nuclei. In contrast, the nuclear energy generation in RN94 fully agrees with the full networks, even in the negative energy episodes. This is due the inclusion of the iron group nuclei responsible of it in RN94.

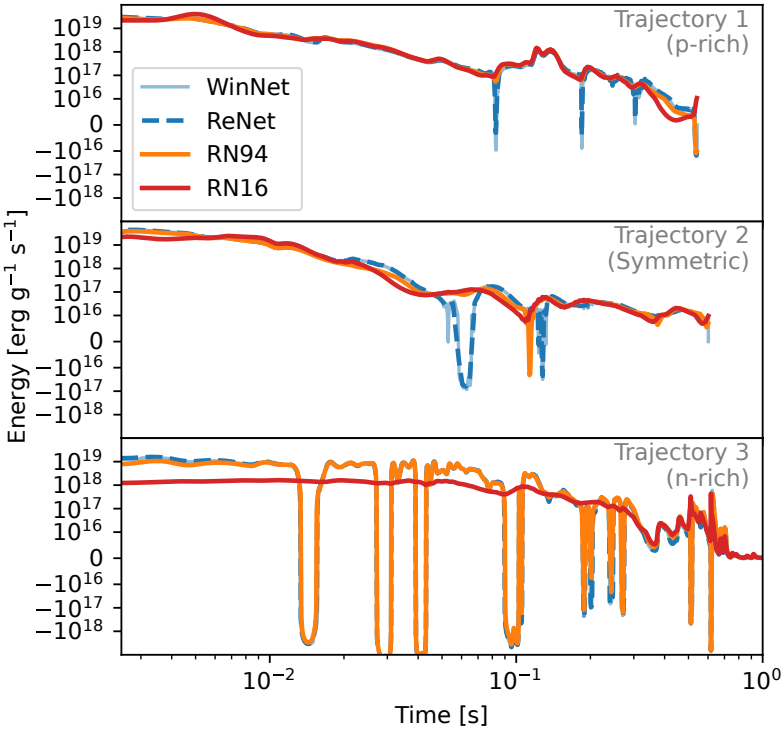

Figure 4.3: Energy generation for two different trajectories. Shown is the generated nuclear energy for four different network architectures. The upper panel shows the energy generation for a slightly proton-rich trajectory ($Y_{e,5.8\,\mathrm{GK}} \sim 0.51$), the middle panel a trajectory with symmetric conditions and the lower panel a slightly neutron-rich one ($Y_{e,5.8\,\mathrm{GK}} \sim 0.48$). The time is relative to the start of the network calculation (i.e., $T = 5.8\,\mathrm{GK}$). Courtesy of Moritz Reichert.

On the other hand, in Figure 4.4 we can observe the final mass fractions obtained with the different networks for the three trajectories. For the slightly proton rich trajectory, the differences in $28 < A < 52$ between RN16 and RN94 arise from the larger amount of nuclei included in the latter, which accounts for the nuclei off the diagonal (see Figure 4.2) such as ^{30}Si or ^{30}S that turn to be quite abundant in this trajectory. Since in RN16 they are not included, the nuclear flow evolves towards more massive symmetric nuclei. This leads to an overproduction of ^{44}Ti of around three orders of magnitude with respect to the full networks. Nevertheless, the final mass fraction of ^{44}Ti in RN94 agrees with a full network within an impressive 0.9%. For this trajectory, the ^{56}Ni produced in the four networks is very similar and below a 3.5% discrepancy.

In the symmetric trajectory RN16 performs better, since the nuclear flow tends to

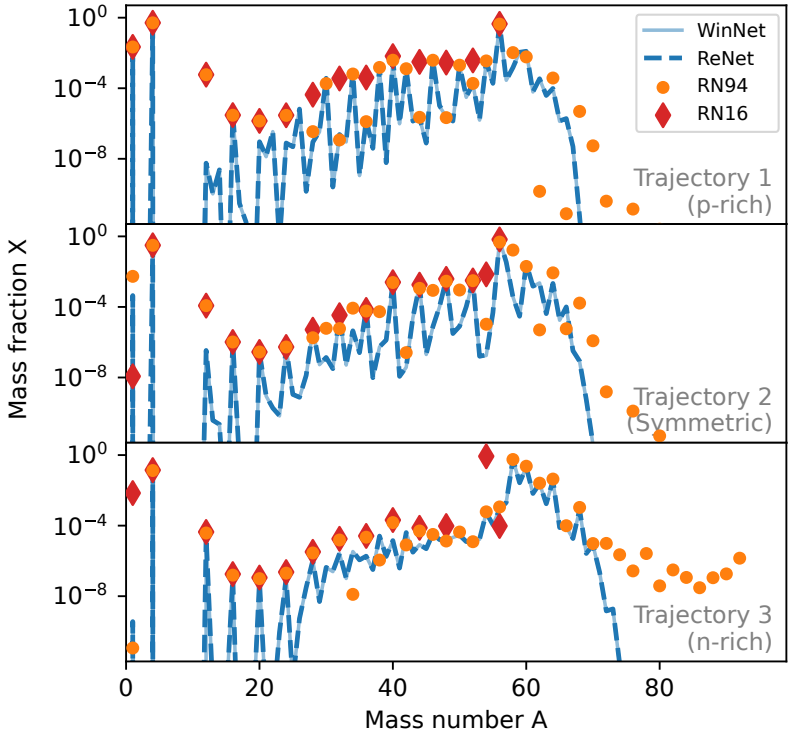

Figure 4.4: Mass fractions versus mass numbers at the end of the simulation for three different trajectories and four different networks. The top panel shows the result for a slightly proton-rich trajectory ($Y_{e,5.8\,\mathrm{GK}} \sim 0.51$), the middle panel a trajectory with symmetric conditions, and the lower panel the result for a slightly neutron-rich one ($Y_{e,5.8\,\mathrm{GK}} \sim 0.48$). Courtesy of Moritz Reichert.

evolve throughout the diagonal. Under these circumstances, ^{44}Ti differs a 3% and ^{56}Ni a 10% in comparison to the full networks. Meanwhile, RN94 show a discrepancy of 35% regarding the final abundances of ^{44}Ti a 22% and ^{56}Ni. The amount of nucleons is well depicted in RN94, while in RN16 is underestimated. As we introduced in Section 3.2, this is relevant for the neutrino opacities.

For the slightly neutron rich trajectory we find a very good agreement of RN94 compared to WINNET and the full network RENET, which reproduces the peak around $A \sim 60$, which includes the most abundant nucleus synthesized in this trajectory, ^{60}Ni. However, we observe how RN94 overproduces nuclei with $A \gtrsim 75$. The exclusion of uneven species in the network probably elude some bottlenecks that would inhibit the further progress of the nuclear flow. Finally, RN94 shows a deviation of 41% in ^{56}Ni and a factor 5 in ^{44}Ti. In contrast, RN16 leads to larger differences due to its reduced amount of species included (factor 8 in ^{44}Ti and 88% in ^{56}Ni). In addition, it shows a

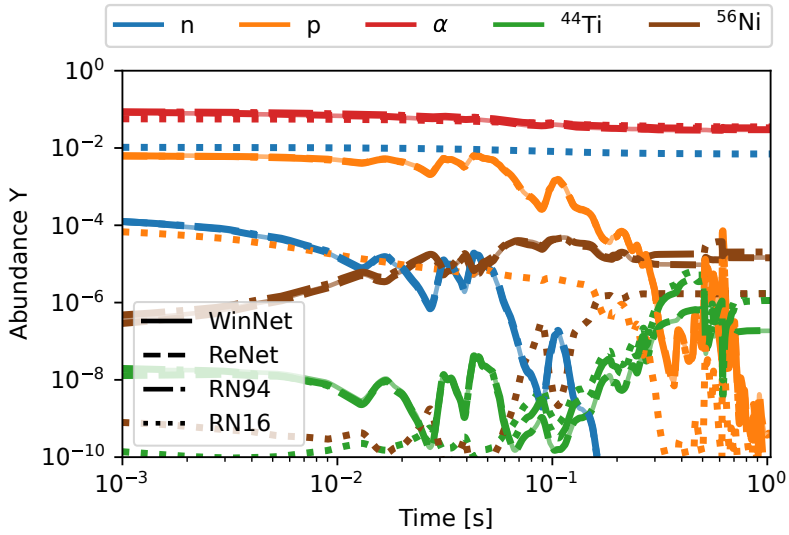

Figure 4.5: Evolution of neutrons, protons, alphas, ^{44}Ti, and ^{56}Ni for a neutron-rich trajectory. Shown are the results for four different reaction networks. Courtesy of Moritz Reichert.

large discrepancy in the neutron mass fraction. Since it basically includes symmetric nuclei, the only way the network can achieve a lower Y_e is by overproducing neutrons. This differences also arise in the NSE composition (Figure 4.5). In the literature, this is partially solved by implementing an extra neutron rich nucleus in the network (e.g., ^{56}Cr in aprox21, Paxton et al. (2011)).

To sum up, RN16 and RN94 are good approximations to a full nuclear network. While they both agree quite well in the energy released in nuclear reactions for slightly proton rich and symmetric matter, RN94 is much more accurate to characterize a slightly neutron rich trajectory since it includes the main relevant species in CCSNe. For the same reason, it produces a more precise nucleosynthesis than RN16, especially in more extreme conditions where matter is not symmetric.

4.3.3 Transition and density-temperature regime

As mentioned in Chapter 3, previous versions of Aenus-Alcar distinguish between two different density regimes. At high densities ($\rho > \rho_{\rm th}$) it employs the EOS of dense matter, and assumes the composition in NSE. At low densities ($\rho \leq \rho_{\rm th}$), it considers the Helmoltz EOS. In this density region, the composition is computed with the approximated flashing scheme (introduced in Section 3.4.2).

When implementing a more sophisticated composition treatment, we observed that the density criteria to distinguish between the EOS (and composition) regimes is far

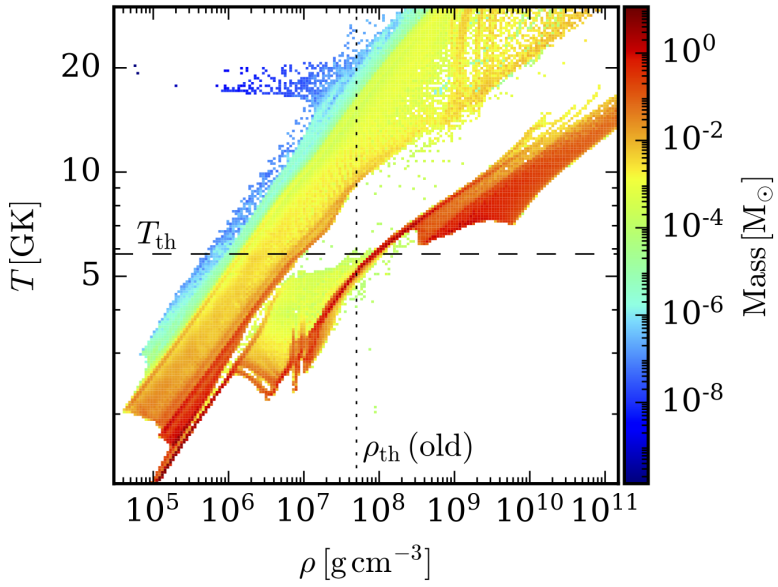

Figure 4.6: Density and temperature achieved in a characteristic CCSN simulation. It focuses on the region of the ρ-T plane close to the transition between the two EOS. The color depicts the amount of mass that fulfilled each (ρ, T) condition in the run. The dashed line indicates the temperature threshold criterion introduced in this work. Finally, the dotted line corresponds to the density threshold criterion present in previous versions of AENUS-ALCAR.

from ideal. Substituting the flashing scheme with the network at low densities does not guarantee that matter is out of NSE. As we show in Figure 4.6, a large number of grid zones that fulfill $\rho \leq \rho_{\rm th}$ are still at high temperatures, and, therefore, the matter there must be considered in NSE. This led to numerical artifacts since the network is not able to perform properly at these temperatures.

To avoid such an inconsistency, we introduced a temperature criteria. Above a certain temperature threshold ($T_{\rm th}$), $T > T_{\rm th} \sim 5 - 6\,{\rm GK}$, we assume the composition in NSE and employ the EOS of dense matter. Otherwise, we call the network together with the subnuclear EOS. Though in principle, the latter case would also apply to very cold zones with densities up to and beyond the nuclear saturation density, in practice this regime (bottom right part of the figure) is not achieved in CCSN and thus of no concern.

In order to prevent discontinuities in the thermodynamic quantities such as the pressure or the internal energy, we interpolate them linearly between the two EOSs in the temperature regime $T_{\rm th} > T > T_{\rm inter}$, where $T_{\rm inter}$ is defined as the lower limit temperature for the interpolation between EOSs (for a schematic representation, see

Figure 5.1). Furthermore, at $T = T_{\rm th}$, the initial values for the network need to be given. Such seeds are provided by an NSE solver which considers the same nuclei as the nuclear reaction network. Once the temperature in a grid cell drops below $T_{\rm th}$, the network module evolves the composition further until the end of the simulation or until the conditions for NSE are reached again.

The energy from the nuclear reactions (Equation (4.8)) is coupled as a source term to the hydrodynamics energy equation, Equation (3.7). In order to avoid thermodynamic inconsistencies, it is done for temperatures $T \leq T_{\rm inter}$. We consider two different ways to include it. On the one hand, the feedback of the nuclear energy from the reaction network is considered at every cell with $T \leq T_{\rm inter}$ (regions II and III in Figure 5.1). On the other hand, the nuclear energy generation is taken into account only after the shock has passed the cell, i.e., in the post-shocked gas (region III). For that purpose, we use a simple shock-detection algorithm. We additionally consider the case with no feedback of the nuclear energy generation from the nuclear reaction network.

4.3.4 Performance of the implementation

In this section, we demonstrate the good functioning of ReNet in Aenus-Alcar by checking the evolution of the nuclear energy generation and the composition in a 1D model we performed.

We used the $20\,M_\odot$ progenitor from Woosley & Heger (2007), and ran the simulation for $1\,\mathrm{s}$ after the bounce (Figure 4.7). At high temperatures ($T > T_{\rm th} = 5.8\,\mathrm{GK}$) we employed the LS220 EOS, and consider matter in NSE. For $T \leq 5.8\,\mathrm{GK}$, we applied the network module. For testing purposes, we used a simplified version of RN92 that used a subgroup of 52 isotopes up to Ge (RN52). Furthermore, we considered the nuclear energy generation when the post-shock region cooled below $T \leq T_{\rm inter} = 5\,\mathrm{GK}$, in order to test the effectiveness of our shock detector. Figure 4.7 demonstrates it works properly, since the nuclear energy generation is activated only in the shocked region when its temperature drops $T \leq T_{\rm inter}$.

In order to check whether the composition and the nuclear energy generation are properly calculated in the simulation (in situ), we compare their evolution to the values obtained in post-processing with Lagrangian trajectories (ex situ). In magenta, we depict the mass shell that we focus on. It first collapses and gets heated by the shock. After that, it expands ,and eventually cools down and leaves NSE. We selected it since most of the unbound matter within the first second follow a similar evolution, and hence it was a very representative example.

We follow the evolution of the nuclear energy generation and the composition when the trajectory leaves NSE ($T \leq 5.8\,\mathrm{GK}$). We show the results of the former in Figure 4.8. We obtain a very similar nuclear energy generation in situ and ex situ. As we have mentioned in the previous section, the transition from NSE to network is specially delicate. We gladly confirm the absence of numerical artifacts and oscillations present in the energy generation.

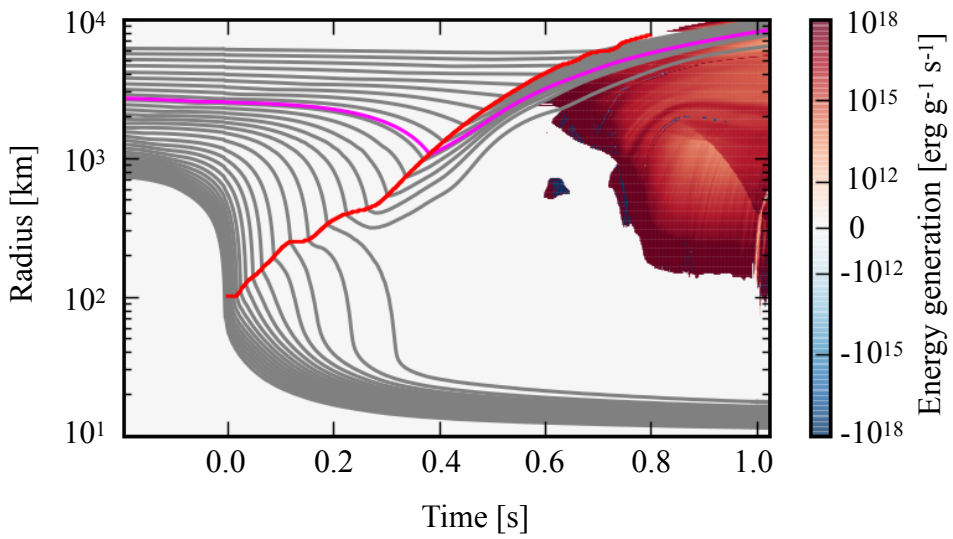

Figure 4.7: Test model where we demonstrate our implementation. Grey lines show mass shell evolution. The red solid line depicts the position of the shock. The coloured region shows the energy released by nuclear reactions. In magenta, the representative trajectory that we focus on to discuss the good performance of RENET in AENUS-ALCAR.

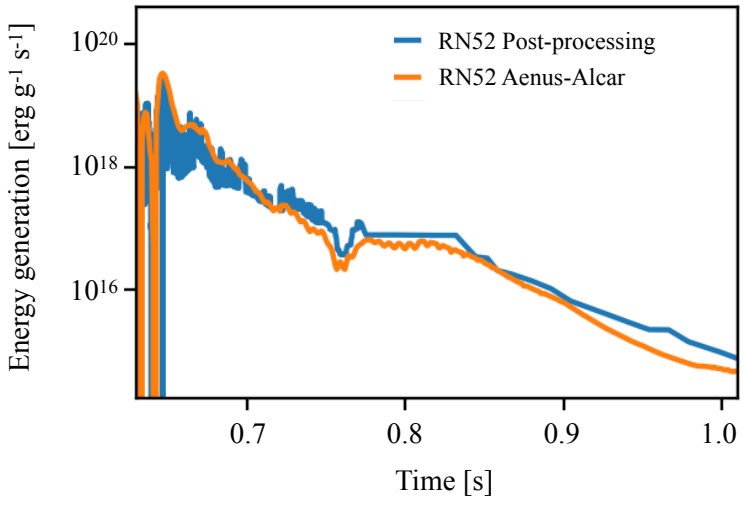

Figure 4.8: Comparison of in situ nuclear energy generation to ex situ.

In Figure 4.9, we show the evolution of the abundances of several species. For comparison, we in addition calculated them with a much more complete network in post-processing, RN789p. Here, $t = 0\,\mathrm{s}$ corresponds to the time when the trajectory leaves NSE. We show the general good agreement between the in situ and the ex situ calculations. In addition, we do not observe numerical artifacts when leaving NSE. However, at late times, in some cases the in situ abundances start to differ a bit. We attribute these differences to the lack of mixing in Lagrangian trajectories and additional numerical diffusion in the simulation.

We conclude that ReNet behaves properly in Aenus-Alcar, and, thus, consider that the implementation has been successful.

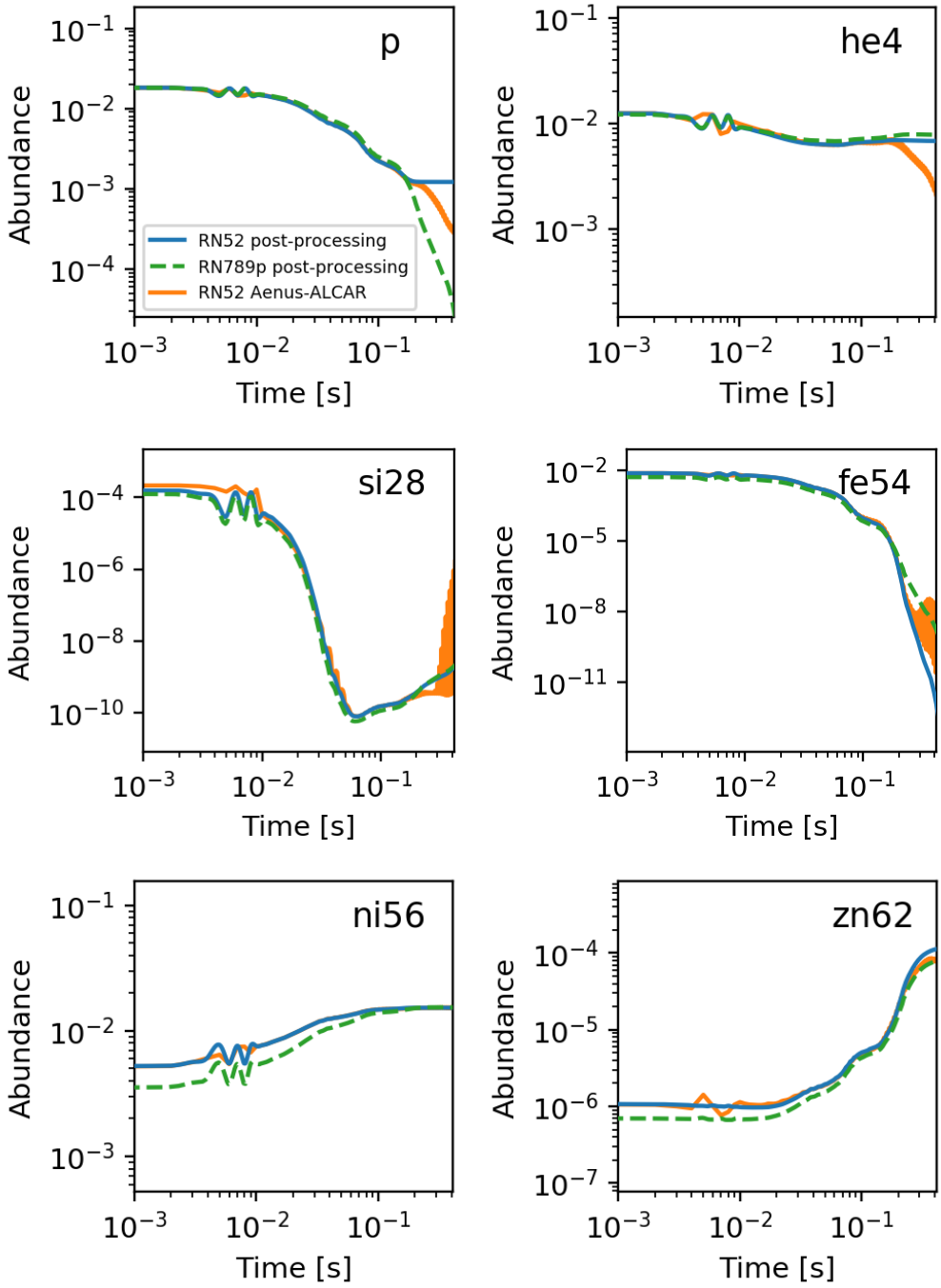

Figure 4.9: Comparison of in situ to ex situ abundances obtained with the same reduced network.

5 CCSNe simulations with reduced nuclear networks

Several groups have employed reduced networks in their works (e.g., Bruenn et al., 2016, 2020; Nakamura et al., 2014; Couch et al., 2015; Harris et al., 2017; Wongwathanarat et al., 2017; Sandoval et al., 2021). Bruenn et al. (2006) mentioned that when including a 14 α-chain in the hydrodynamics, nuclear burning in the oxygen layer deposited extra pressure in the vicinity of the shock and assisted its expansion. Nakamura et al. (2014) performed simulations with a simplified light-bulb neutrino treatment using a 13 isotope α-network to study how the energy released by nuclear reactions affect the dynamics of the explosion. They conclude that energy produced by the infalling material behind the shock could aid the explosion, especially in models with marginal explosions. A large network was included for the first time by Harris et al. (2017) in 2D simulations with accurate ν-transport. They used a 14 α-chain and a 150 isotope network in axisymmetric (2D) models and studied the uncertainties derived from post-processing nucleosynthesis. Their results showed the limitations of using post-processing Lagrangian tracer particles and support including reaction networks in the simulations.

In this chapter, the aforementioned studies motivated us to investigate in detail, in a state-of-the-art CCSN code, how the different treatments of the composition employed in the simulations at low temperatures have an impact in the dynamics of the explosion and the nucleosynthesis outcomes. This chapter is adapted from Navó et al. (2023). In Section 5.1, we introduce the models we have performed. In Section 5.2, we show the impact of the composition treatment in the dynamics of the explosion. In Section 5.3, we study the effects on the nucleosynthesis.

5.1 Models

We have performed simulations ($t_{\rm f} = 1.5\,{\rm s}$) using the solar metallicity $20\,{\rm M}_{\odot}$ mass progenitor from Woosley & Heger (2007). We map its pre-collapse composition to those of our two networks. We consider the EOS transition at $T_{\rm th} = 5.8\,{\rm GK}$[1], given that NSE breaks down around this temperature, and $T_{\rm inter} = 5.0\,{\rm GK}$. Since this work is

[1]We tested several transition temperatures. A higher transition temperature ($T_{\rm th} = 6.5\,{\rm GK}$) does not change the dynamics significantly. When decreasing it ($T_{\rm th} = 5\,{\rm GK}$), the alpha-rich freeze out is not well characterized.

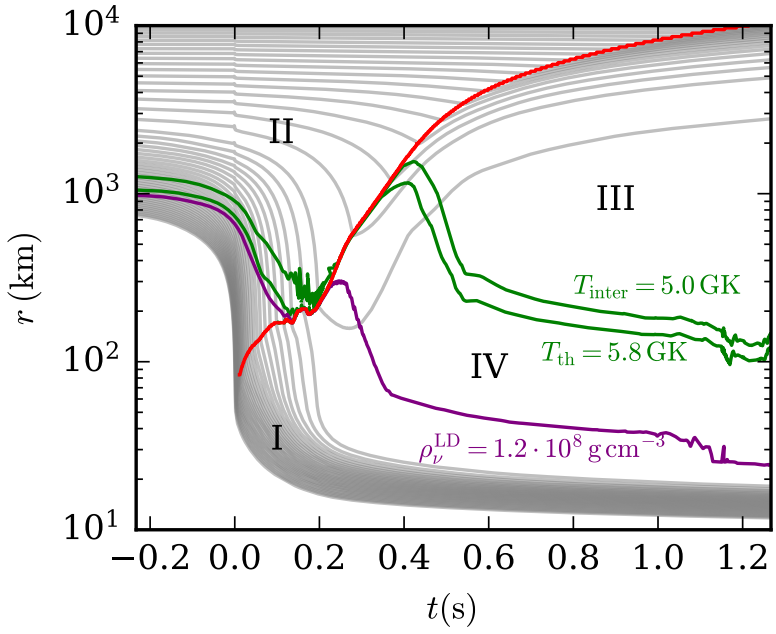

Figure 5.1: Schematic representation of the different regions of interest in this chapter. It shows the mass shell evolution (grey) of a characteristic 1D model. The red line shows the shock evolution. The temperatures involved in the transition between the NSE and the network regimes are depicted in green. The purple line shows the evolution of $\rho_\nu^{\rm LD}$, the density at which we switch off the neutrino absorption in the toy models described in Section 5.1.

focused on the impact of the composition treatment at $T < T_{\rm th}$, all of the models have the same configuration at high temperatures (areas I and IV in Figure 5.1). We apply the SFHo EOS (Steiner et al., 2013) and assume the composition provided by it in NSE. We consider the main neutrino-matter interactions (Just et al., 2015; Just et al., 2018) contributing to the neutrino energy deposition, Q_ν, which is critical for triggering the explosion. As mentioned in Section 3.2.3, spherically symmetric simulations do not explode due to the lack of convection and hydrodynamical instabilities (e.g., Janka, 2012). Therefore, we add an extra heating factor, $HF = 2.8$, in the gain region to launch explosions in all of the 1D. In 2D models we set $HF = 1$ and do not add any additional neutrino heating.

In order to understand the impact of nuclear reaction networks coupled to the hydrodynamics, we have varied the treatment of the composition and nuclear energy generation at $T \leq T_{\rm th}$. Four approaches have been used to describe the composition at low temperatures and densities, where a network is necessary.

- The most crude description is to keep using the high-density (or nuclear) EOS table also at low temperatures. This is commonly done in many supernova simulations that focus on the early explosion phase (e.g., O'Connor & Couch, 2018). The composition in EOS tables consist usually of neutrons, protons, alpha particles, and a representative nucleus. This nucleus is obtained from assuming NSE or from SNA (single nucleus approximation) (see Schneider et al., 2017, for a discussion of the impact of these two treatments). These models are marked as "SFHo" and their composition correspond to NSE.
- The flashing scheme was the improved composition treatment that has been used in the previous studies with ALCAR. In this set of models, for comparison purposes, the version of the flashing scheme employed does not include the nuclear energy implicitly. Therefore, to distinguish it from the original version (Rampp & Janka, 2002), we reference to it as $\mathrm{flashing}^{\dagger}$ and the models are labeled _flsh.
- We use the two reduced networks described in Section 4.3.1. The model names are RN16 and RN94.

The composition obtained with the four approaches is different and influences the final abundances, but also the dynamics. Variations of the abundances of nuclei heavier than alphas have a minor contribution to the pressure since it is dominated by radiation and electrons rather than ions. However, the changes in the amount of neutrons and protons can impact the energy deposited by neutrinos. Therefore, we have also run a few comparison models without the neutrino absorption at low densities, $\rho < 1.2 \cdot 10^8\,\mathrm{g\,cm^{-3}}$ (models with no Q_ν^{LD}), i.e, $Q_\nu = 0$ in regions II, III and IV of Figure 5.1.

Finally, we include also various models to explore the impact of the energy generation by nuclear reactions when using the two reduced networks in 1D and 2D. We consider $\dot{E}_{\mathrm{nuc}}$ in the two ways introduced in Section 4.3: in all regions with with $T < T_{\mathrm{inter}}$ (region II and III in Figure 5.1) where the composition is determined by the reduced networks (models labeled with "E") and alternatively only between $T < T_{\mathrm{inter}}$ and the shock, i.e., only region III (models labeled with "p.s."). We employ these two different $\dot{E}_{\mathrm{nuc}}$ configuration in order to distinguish between the impact in the infalling layers and in the post-shock region. In addition, we run a model with the flashing scheme including its nuclear energy generation (1D_flshE) for comparison.

We perform the 1D simulations using a grid with $n_{\mathrm{r}} = 408$ zones that are logarithmically spaced in radial direction with a central grid width of $\Delta r = 400\,\mathrm{m}$ and a maximum radius of $R_{\mathrm{out}} \simeq 9.05 \cdot 10^5\,\mathrm{km}$. The 2D simulations run on a grid of $n_r = 400$ zones in the radial direction and $n_\theta = 128$ in the angular direction. We consider the employed resolution sufficient to adequately resolve the hydrodynamic quantities (e.g., Obergaulinger & Aloy, 2017). The models computed are listed in Table 5.1. In following sections, we discuss the impact of the composition and nuclear reactions on the dynamics and final abundances.

Model	Comp	$\dot{E}_{\rm nuc}$	$Q_\nu^{\rm LD}$	Dim
1D_flsh_no$Q_\nu^{\rm LD}$	flashing†	no	no	1D
1D_RN16_no$Q_\nu^{\rm LD}$	RN16	no	no	1D
1D_RN94_no$Q_\nu^{\rm LD}$	RN94	no	no	1D
1D_SFHo_no$Q_\nu^{\rm LD}$	NSE	no	no	1D
1D_flsh	flashing†	no	yes	1D
1D_RN16	RN16	no	yes	1D
1D_RN94	RN94	no	yes	1D
1D_SFHo	NSE	no	yes	1D
1D_RN16E	RN16	yes	yes	1D
1D_RN16e	RN16	p.s	yes	1D
1D_RN94E	RN94	yes	yes	1D
1D_RN94e	RN94	p.s	yes	1D
1D_flshE	flashing	yes	yes	1D
2D_flsh	flashing†	no	yes	2D
2D_RN16E	RN16	yes	yes	2D
2D_RN94E	RN94	yes	yes	2D

Table 5.1: List of models . The second column shows the treatment of the composition. The third column specifies whether the energy generation from the nuclear reactions is taken into account. p.s indicates that is switched on only in the post-shock region. The fourth column indicates whether the neutrino interactions are taken into account at $\rho < 1.2 \cdot 10^8\,{\rm g\,cm^{-3}}$. Finally, the last column states for the dimensionality of the simulations.

5.2 Impact on the dynamics

In this section we study the effects that reduced networks have on the dynamics of the explosion. We show how the different treatments of the composition lead to changes in the neutrino absorption that modify the dynamics (Section 5.2.1) and the impact of the energy released by nuclear reactions on the dynamics of the explosion in 1D (Section 5.2.2) and 2D (Section 5.2.3)

5.2.1 Composition

First, we detail the impact that the different composition treatments have on the dynamics of the explosion in the models introduced in Section 5.1.

We start comparing 1D models with different composition treatment, no $Q_\nu^{\rm LD}$, and no $\dot{E}_{\rm nuc}$ at $T < T_{\rm th}$: 1D_SFHo_no$Q_\nu^{\rm LD}$, 1D_flsh_no$Q_\nu^{\rm LD}$, 1D_RN16_no$Q_\nu^{\rm LD}$, and 1D_RN94_no$Q_\nu^{\rm LD}$. Figure 5.2 shows the evolution of the shock radius for these models (dotted lines). Without energy transfer between neutrinos and matter at low densities

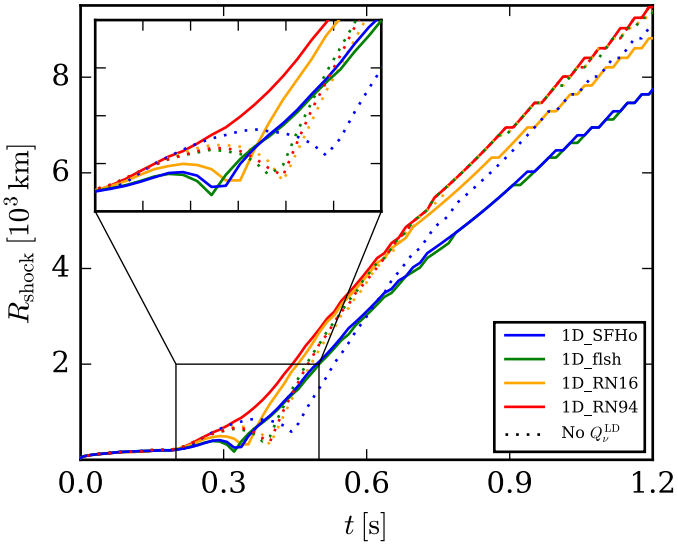

Figure 5.2: Shock evolution of the 1D models with no energy feedback from the nuclear reactions. The different colors represent each treatment of the composition. For consistency, the same color scheme is used in the next Figures. Solid lines stand for 1D models without $\dot{E}_{\rm nuc}$, e.g. 1D_RN16. Dotted lines correspond to models with no $\dot{E}_{\rm nuc}$ nor $Q_\nu^{\rm LD}$, e.g. $1{\rm D\_RN16\_noQ}_\nu^{\rm LD}$.

and temperatures, the main variation among the non-SFHo models is the composition, which is an input for the Helmholtz EOS. We note that in the relevant temperature regime the baryonic contribution is negligible and thus the way the nuclear composition is treated has no dynamical effect. Thus, the composition differences between the non-NSE models do not affect the evolution of the shock. However, $1{\rm D\_SFHo\_noQ}_\nu^{\rm LD}$ uses a different table for the leptonic contribution than the other three runs. Its slightly different pressure and internal energy modifies the evolution of the shock.

In case that Q_ν is taken into account in the entire simulation domain (models 1D_flsh, 1D_SFHo, 1D_RN16, and 1D_RN94, solid lines in Figure 5.2), the different evolution of the shock is now mainly influenced by this additional energy source term, which is dominant over the changes between different EOS. 1D_flsh and 1D_SFHo have almost identical behavior due to their very similar composition, which consists of nucleons, alphas (in case of 1D_SFHo), and a representative nucleus. This leads to a comparable amount of nucleons and, thus, similar neutrino opacities and neutrino heating. Note that $Q_\nu \propto \kappa_{\rm a} \propto n_{\rm N}\sigma_{\nu{\rm N}}$, where $\kappa_{\rm a}$ is the absorption opacity, $n_{\rm N}$ is the free nucleon density, and $\sigma_{\nu{\rm N}}$ is the neutrino-nucleon cross section.

Models 1D_RN16 and 1D_RN94 show changes in the evolution due to the different species included in the simulation, which changes the amount of nucleons and,

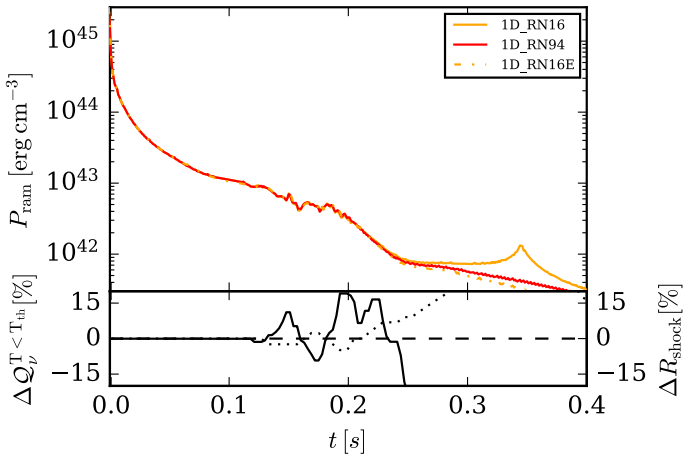

Figure 5.3: Evolution of the ram pressure for the 1D_RN94, 1D_RN16, and 1D_RN16E models in the first $350\,\mathrm{ms}$ post-bounce. Bottom panel shows the relative differences in the integrated neutrino energy deposition at $T < T_{\rm th}$, $\mathcal{Q}_\nu^{\rm T<T_{th}} = \int_{\rm T<T_{th}} Q_\nu \, {\rm d}V$, (solid line) and shock radius (dotted) of 1D_RN94 and 1D_RN16.

therefore, the neutrino absorption. The nuclei mapped into simulations employing the RN94 are different than the ones that are considered in the original progenitor[2], which provides the “aprox19" composition. For this reason, RN94 performs a readjustment where (α, p) reactions are dominant in the oxygen rich layers. This leads to a difference in the mass fractions of the neutrons of $\Delta{\rm n} \equiv \log_{10}(\frac{X_{\rm n}^{\rm RN94}}{X_{\rm n}^{\rm RN16}}) = 0.3$ and $\Delta{\rm p} = 2.3$ for protons[3], which results in an increase of the opacity in the vicinity of the shock. This translates into differences of up to $15\,\%$ in the neutrino heating in the low density regime (Figure 5.3) and in a decrease of the ram pressure in the shock, which, although small, is sufficient to modify its balance, allowing for an easier expansion in 1D_RN94.

5.2.2 Nuclear energy generation in 1D

The energy from nuclear reactions significantly changes the dynamics. Figure 5.4 shows the shock evolution for simulations performed with the RN16 and RN94 networks taking into account the three different configurations for $\dot{E}_{\rm nuc}$. The impact of $\dot{E}_{\rm nuc}$ on the dynamics depends on whether the energy is released in the progenitor shells or the post-shock region. To show it in a clear manner, we first focus on the

[2]obtained from https://2sn.org/nucleosynthesis/WH2007.shtml
[3]For more differences on nucleons, for a characteristic trajectory, see Figure 4.5 in Section 4.3.2

different evolution among the models with RN16. The absence of $\dot{E}_{\rm nuc}$ in the progenitor infalling shells in 1D_RN16 and 1D_RN16e lead to a very similar evolution of the shock and the mass shells. The shock is revived after experiencing a fall back at $t \sim 300\,\mathrm{ms}$ and gaining enough energy from the system to expand. Nevertheless, in 1D_RN16e, it expands slightly faster once the nuclear reactions are starting to feed the system with energy. This is better depicted in Figure 5.5, where the explosion energy shows that model 1D_RN16e is more than $15\,\%$ more energetic than 1D_RN16 after $500\,\mathrm{ms}$ post-bounce due to the nuclear energy released in the explosive nucleosynthesis. 1D models with nuclear energy generation also in the progenitor shells (1D_RN16E, 1D_RN94E, and 1D_flshE) experience an early expansion with no fall-back and less layers are accreted to the PNS. Initially, the Fe group rich layers absorb energy mainly through (γ,α), (n,α), and (γ,n) reactions, accelerating slightly the collapse (e.g., Couch, 2017). The energy released in outer mass shells, i.e. oxygen and silicon layers, is dominated by (α,γ) and (p,γ) reactions which produce $\dot{E}_{\rm nuc} > 0$. This heats up the infalling matter substantially (see Figure 5.6). The contribution of the nuclear reactions is larger than the one of neutrino absorption, for $T \leq T_{\rm th}$, from $t = 0.1\,\mathrm{s}$ on. Therefore, nuclear reactions supply a significant amount of energy to the infalling layers, more than $10^{50}\,\mathrm{erg\,s^{-1}}$, which is comparable to the change in internal energy ($\sim 10^{50} - 10^{51}\,\mathrm{erg\,s^{-1}}$) in the region. This becomes the dominant heating source for $T \leq T_{\rm th}$, increasing further the explosion energy. The additional energy source leads to a decrease of the ram pressure on the shock and allows it to expand easier (Figure 5.3), in agreement with Nakamura et al. (2014); Bruenn et al. (2006).

We note that in terms of the shock radius and explosion energy the evolution of model 1D_flshE proceeds similarly to models 1D_RN16E and 1D_RN94E for the first $\sim 300\,\mathrm{ms}$. During this period, the nuclear energy generation of the flashing scheme with its approximate composition of $^{28}\mathrm{Si}$ and $^{56}\mathrm{Ni}$ is not too different from that in the network models. At later times, reactions that cannot be represented by these two nuclei become more important and, consequently, the explosion energy of the flashing model starts to deviate from that of the network models (see Figure 5.5). This behavior seems to indicate that a flashing scheme with more nuclei might reproduce the evolution of the network more closely.

Despite the similar overall evolution for 1D_RN16E and 1D_RN94E, we encounter some differences in the nuclear energy production. Before the bounce, as pointed out previously, the photodisintegration reactions in the iron group absorb energy from the environment. The RN16 is not able to track efficiently these nuclei due to its simplicity. Because of that, we observe a spike of $\dot{\mathcal{E}}_{\rm nuc} > 0$, where (α,γ) reactions in the oxygen and silicon rich shells are able to release more energy than photodisintegrations absorb in the iron and nickel rich layer. In contrast, the RN94 has a broader set of nuclei in the relevant region of the nuclear chart and therefore includes a more complete set of reactions such as e.g., additional (n,γ) reactions. This leads to the observed differences. At intermediate times, between the bounce and $t \sim 500\,\mathrm{ms}$, $^{24}\mathrm{Mg}(\alpha,\gamma)$, $^{27}\mathrm{Al}(p,\gamma)$, $^{28}\mathrm{Si}(\alpha,\gamma)$, and $^{54}\mathrm{Fe}(p,\gamma)$ are the main contributors to the

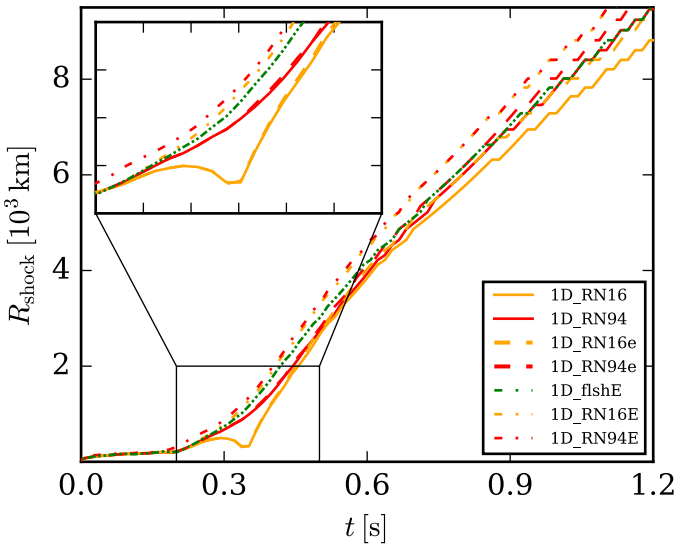

Figure 5.4: Shock evolution for the remaining 1D models, which include $\dot{E}_{\rm nuc}$. For comparison, we keep the models without it, i.e., 1D_RN16 and 1D_RN94 (solid). Dashed lines indicate the 1D_RN16e and the 1D_RN94e models. Dash-dotted lines correspond to the 1D_RN16E, the 1D_RN94E, and the 1D_flshE.

energy generation in the accreted layers. At these times, since all these reactions are included in RN16 and RN94, the energy production in both networks is comparable as shown by the fluctuations of $\Delta\dot{\mathcal{E}}_{\rm nuc}$ in Figure 5.6. Finally, from $t \sim 500\,{\rm ms}$ on, the nuclear energy is mostly produced in the post-shocked region. We observe how $\Delta\dot{\mathcal{E}}_{\rm nuc}$ stabilise around $50\,\%$. Part of this difference is due to the slightly different shock evolution, which evolves slightly faster in 1D_RN16E. The remaining discrepancy cannot be easily broken down to an individual reaction, but rather to an overall slightly different nucleosynthetic path. The different amount of included nuclei in the calculation causes the differences. While most of the main reactions contributing to $\dot{\mathcal{E}}_{\rm nuc}$ in this region are included in both networks, e.g,$^{16}{\rm O}(\alpha,\gamma)$, $^{28}{\rm Si}(\alpha,\gamma)$, $^{54}{\rm Fe}(p,\gamma)$, or $^{55}{\rm Co}(p,\gamma)$, additional available paths in RN94 allow for the inclusion of several secondary reactions which provide additional energy to the system, e.g, $^{58}{\rm Ni}(p,\gamma)$ and $^{59}{\rm Cu}(p,\gamma)$. Furthermore, a difference in the amount of nucleons and α can lead to an additional deviation of the nuclear energy.

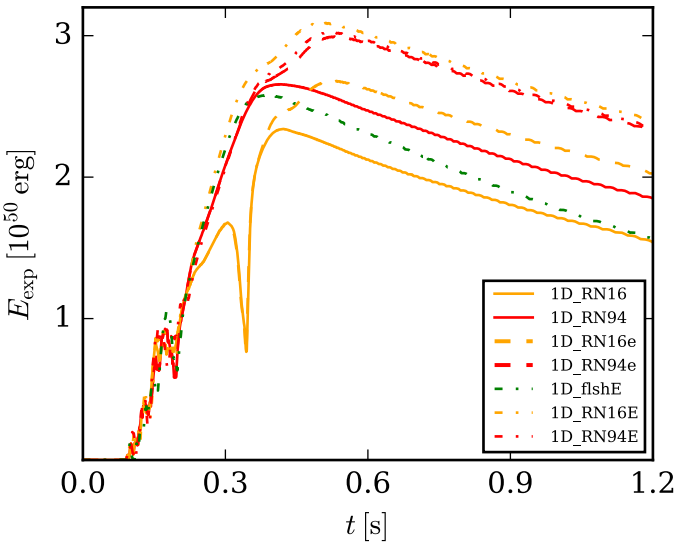

Figure 5.5: Explosion energy corresponding to the same models depicted in Figure 5.4

5.2.3 Nuclear energy generation in 2D

All of the two-dimensional models show typical supernova explosions, with explosion energies (Figure 5.7) of several 10^{50} erg and the characteristic prolate shape due to axisymmetry (Bruenn et al., 2016; Summa et al., 2016; Vartanyan et al., 2018). The nuclear energy generation also leads to changes in the morphology of the explosion in the 2D models (Figures 5.8 and 5.9). However, $\dot{E}_{\rm nuc}$ is less determinant for the onset of the explosion than in 1D, since relaxing spherical symmetry allows for non-radial deformations and convection which enhance the neutrino heating in the gain layer and trigger an easier shock expansion.

The long-term evolution, in particular the growth of the explosion energy, can differ quite significantly even between otherwise similar models. The shock waves of models 2D_flsh and 2D_RN16E expand anisotropically with a moderate north-south asymmetry at early times (Figures 5.8a and 5.8c). The comparable weakness of the shocks in one of the hemispheres allows for important accretion streams towards the PNS. These lead to a significant increase in the neutrino emission (and, therefore, in $E_{\rm exp}$) which trigger an α-rich ν-driven outflow towards the southern pole (the cone filled with high-entropy, high-velocity gas in Figure 5.8d) in 2D_RN16E and an axial outflow in 2D_flsh. In 2D_RN16E, the effect of $\dot{E}_{\rm nuc}$ on $R_{\rm shock}$ is small and contributes to accelerating it around $t \sim 800\,{\rm ms}$ after bounce. The rate at which nuclear reactions deposit energy in the wind and post-shock region is significant, comparable to the growth rate of $E_{\rm exp}$ (upper panel of Figure 5.7). This supports the outflows and leads to a more energetic explosion.

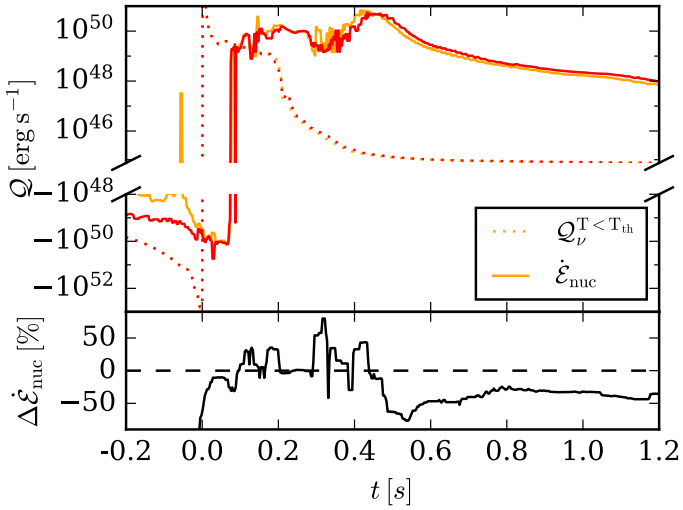

Figure 5.6: The upper panel shows the evolution of the integrated energy source terms in the $T < T_{\mathrm{th}}$ region ($\mathcal{Q}$) for the models 1D_RN94E and 1D_RN16E in red and yellow, respectively. $\mathcal{Q}_\nu^{\mathrm{T<T_{th}}} = \int_{\mathrm{T<T_{th}}} Q_\nu \,\mathrm{d}V$ and $\dot{\mathcal{E}}_{\mathrm{nuc}} = \int_{\mathrm{T<T_{th}}} \dot{E}_{\mathrm{nuc}} \,\mathrm{d}V$. The lower panel shows the relative difference in the energy released by nuclear reactions in the low density region.

The shock in 2D_RN94E, in contrast, expands more symmetrically towards higher radii initially, which we attribute to the higher amount of energy generated by nuclear reactions around $t = 100\,\mathrm{ms}$. This reduces the accretion inflows towards the PNS as a comparison of the masses indicates: $M_{\mathrm{PNS}} = 1.67$, 1.72, and $1.71\,\mathrm{M}_\odot$ for 2D_RN94E, 2D_flsh, and 2D_RN16E, respectively. Therefore, the amount of neutrinos emitted after $t \sim 500\,\mathrm{ms}$ is significantly lower, which explains the absence of $\nu-$driven winds in 2D_RN94E and the stagnation of E_{exp}, in contrast to 2D_RN16E and 2D_flsh.

At later times, downflows accreting onto the PNS squeeze its polar region, launching high velocity, neutron-rich outflows ($Y_{\mathrm{e}} \sim 0.35$) ejected from the vicinity of the PNS. This is shown for model 2D_RN94E in Figure 5.10, where we observe a neutron-rich bubble (indicated by the circle A) which moves from the center (upper left panel) to $z \sim -6000\,\mathrm{km}$ in only $150\,\mathrm{ms}$ (bottom panel), and continues evolving towards higher latitudes mixing with the surrounding material (panel c). The high v_{r}, up to $\sim 0.16\,c$, avoid excessive neutrino absorption that would, for the conditions prevailing here, increase the electron fraction. These outflows tend to be amplified by the nuclear energy generation in the already shocked areas. The predominantly polar direction of this bubble may be at least partly due to the assumed axisymmetry rather than being a general feature of such neutron-rich clumps. In fact, the presence of another such bubble (circle B in Figure 5.10) shows that they can be formed at any latitude

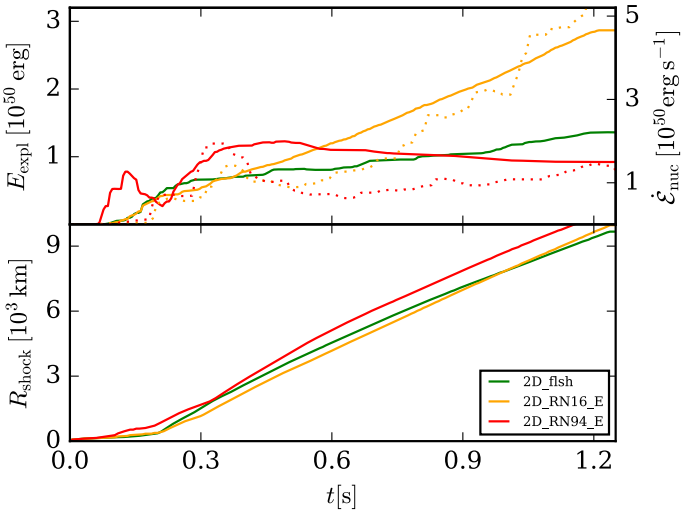

Figure 5.7: Shock and explosion energy evolution of the 2D models.

as a consequence of the random dynamics of convection and accretion streams in the vicinity of the PNS. The lower radial velocity of the equatorial outflow ($\sim 0.07\,c$) and the accretion of the upper layer prevent it from evolving towards a larger radius. Heating by nuclear energy reactions at rates around $\dot{E}_{\rm nuc} \sim 10^{20}\,{\rm erg\ g^{-1}s^{-1}}$ plays an important role in sustaining the clump. As we show in the next section, this mechanism allows for the production of more neutron rich species.

To sum up, in this section we have studied the impact of reduced networks on the dynamics of the explosion. The different nuclei included can modify the amount of nucleons and hence the neutrino absorption at $T < T_{\rm th}$. This different heating in the infalling progenitor shells has an impact on the ram pressure and therefore can change the shock evolution. Analogously, the nuclear energy released in that region allows for a decrease of the ram pressure on the shock and favors an easier expansion. In addition, nuclear reactions in the shocked region are able to increase substantially the explosion energy. The 2D_RN94 model suggests that the important nuclear energy generation in this region helps to sustain late low-$Y_{\rm e}$ outflows in the equatorial direction. Finally, RN16 and RN94 show small differences in $\dot{E}_{\rm nuc}$.

5.3 Impact on the nucleosynthesis

In this section we study the effects that reduced networks have on the composition of the ejecta at the end of the simulation, i.e., $t = 1.5\,{\rm s}$, in 1D and 2D models.

For comparison, the nucleosynthesis is additionally computed in post-processing with the full nuclear reaction network WinNet (Reichert et al., 2023) and the reduced

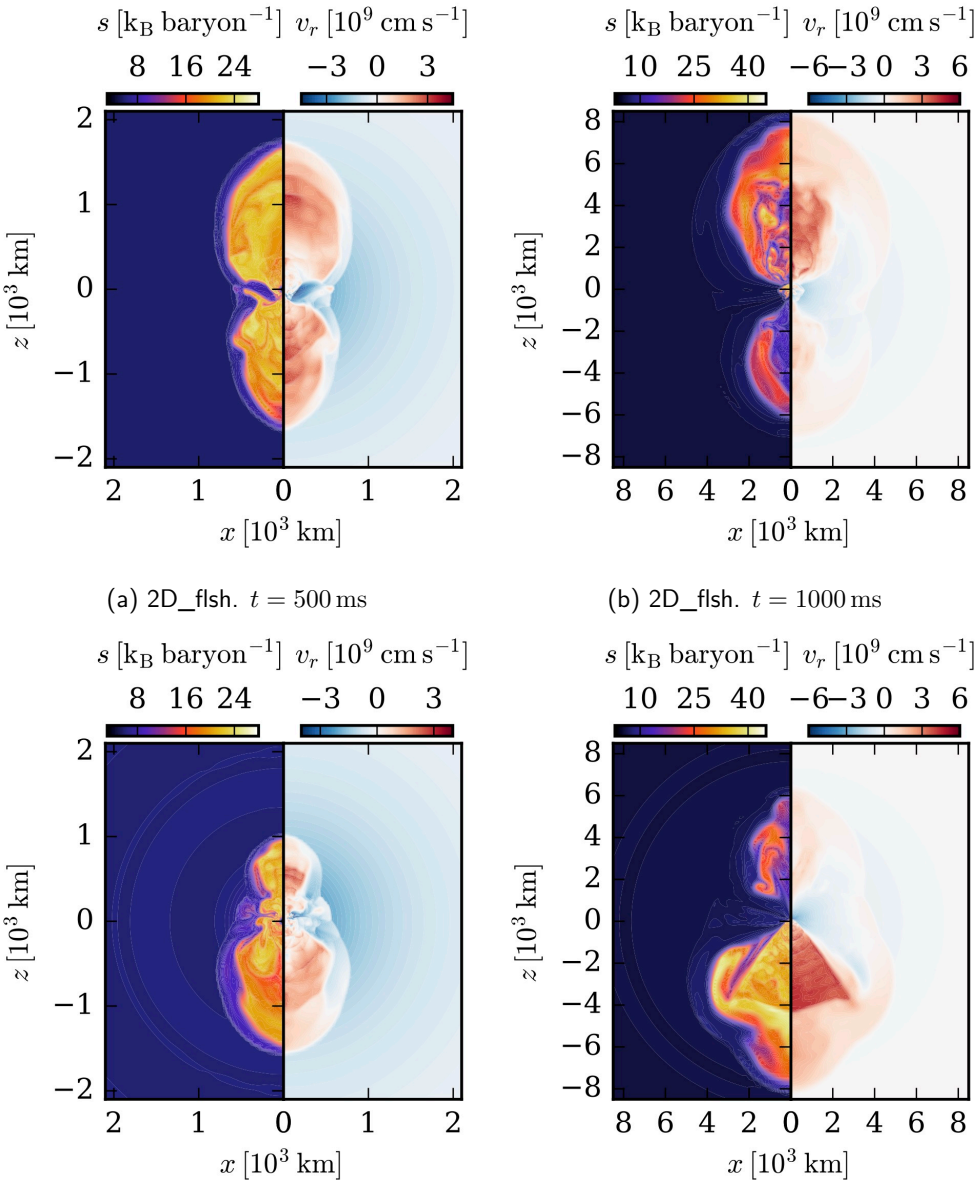

(a) 2D_flsh. $t = 500\,\mathrm{ms}$

(b) 2D_flsh. $t = 1000\,\mathrm{ms}$

(c) 2D_RN16E. $t = 500\,\mathrm{ms}$

(d) 2D_RN16E. $t = 1000\,\mathrm{ms}$

Figure 5.8: Slices of entropy and radial velocity of the 2D_flsh and the 2D_RN16E models at $500\,\mathrm{ms}$ and $1000\,\mathrm{ms}$ of simulation.

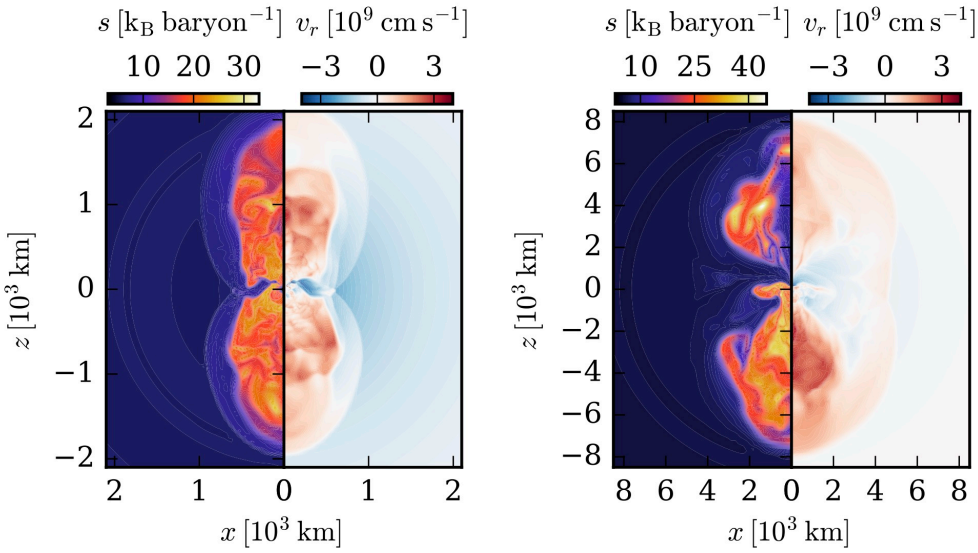

(a) 2D_RN94E. $t = 500\,\mathrm{ms}$ (b) 2D_RN94E. $t = 1000\,\mathrm{ms}$

Figure 5.9: Slices of entropy and radial velocity of the 2D_RN94E model at $500\,\mathrm{ms}$ and $1000\,\mathrm{ms}$ of simulation.

networks RN16 and RN94. We consider the unbound matter, i.e., matter with positive total energy and positive radial velocity, at the final time of the simulation ($t_\mathrm{f} = 1.5\,\mathrm{s}$). The evolution of the ejecta is followed by Lagrangian tracer particles calculated backwards in time as described in Reichert et al. (2022) (see also Sieverding et al. (2023) for an in-depth analysis of the uncertainties that can arise with this method). At the final simulation time, we place them at random positions in all cells flagged as unbound. The total mass contained in a cell is distributed equally among its tracers. Their number is set such that they have a maximum mass, $M = 10^{-4}\,\mathrm{M}_\odot$, and each cell contains at least 4 tracers. At the end, the nucleosynthesis of each tracer particle is weighted with its corresponding mass.

5.3.1 Post-processing with WinNet

First, we show the impact on abundances by computing them with the post-processing nucleosynthesis network WinNet. We compare the abundances obtained in models that include nuclear energy generation (1D_RN16E, 1D_RN94E, 2D_RN16E and 2D_RN94E) with the ones from models that do not take $\dot{E}_\mathrm{nuc}$ into account (1D_flsh and 2D_flsh), in 1D and 2D respectively.

In spherically symmetric models, $\mathrm{Y_e}$ is very close to 0.5. Therefore, species beyond the iron group are not synthesized (Figure 5.11). This also explains the only minor

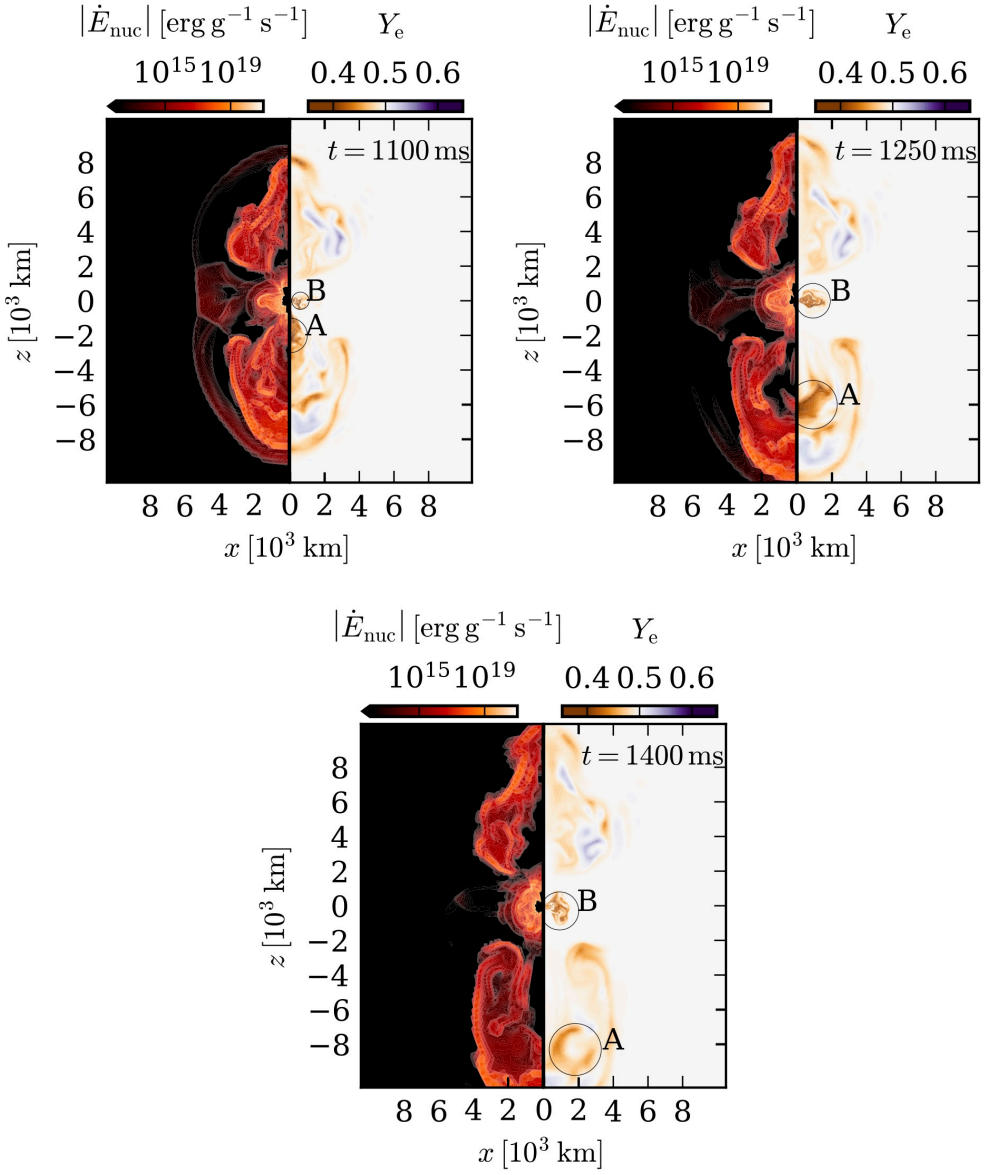

Figure 5.10: Snapshots of the magnitude of $\dot{E}_{\rm nuc}$, and $Y_{\rm e}$ of model 2D_RN94E at $t = 1100\,{\rm ms}$, $t = 1250\,{\rm ms}$, and $t = 1400\,{\rm ms}$. We highlight the different evolution of two low-$Y_{\rm e}$ clumps (A and B) ejected from the vicinity of the PNS. While A is ejected in the polar direction and eventually mixing up with external layers, B cannot overcome the accretion in the equatorial region and stagnates. Nevertheless, the high nuclear energy released in that region helps to sustain this outflow in time.

differences in the post-processing final composition with WinNet for the 1D_flsh, the 1D_RN16E, and 1D_RN94E models, despite the different dynamic evolution when the energy generation from the nuclear reactions is taken into account.

In the two-dimensional models (Figure 5.12) a larger amount of nuclei are involved due to the broader range of Y_e. The 2D_flsh and 2D_RN16E model show standard CCSN nucleosynthesis, where mainly iron group elements are formed together with lighter heavy species around $A \sim 90$ (see e.g., Eichler et al., 2017; Harris et al., 2017; Wanajo et al., 2018; Witt et al., 2021). In contrast, model 2D_RN94E produces larger amounts of heavier species. The composition obtained with WinNet shows a significant enhancement around the first r-process peak, $A \sim 80$, particularly ^{84}Ge. Also, a small amount is observed up to the second r-process peak, $A \sim 130$. This larger production of heavier species takes place in the late low-Y_e outflows, which are supported by the nuclear energy release as outlined in Section 5.2. We observe an agreement between the post-processing RN94 (ex situ) and WinNet abundances in the 2D_RN94E model until $A \sim 90$, showing that RN94 is able to reproduce the main nuclei synthesized in CCSN. There is a difference in ^{92}Mo that can be explained by the fact that it acts as a bottle neck for heavier species in RN94.

5.3.2 Ex situ vs in situ calculations

In this section we show the differences of computing the nucleosynthesis in the simulation (in situ) and in post-processing (ex situ). For the comparison, we calculate the latter with the same network employed in the hydro (RN16 or RN94, depending on the model).

In Figures 5.11 and 5.12, we also show the composition obtained in situ in the models with the networks and its respective post-processing, ex situ calculation. The goal is to analyse which differences come from evolving the network together with the hydro. The 1D_RN16E and 1D_RN94E models show very good agreement in the most abundant species, like ^{56}Ni. However, there are some discrepancies on ^{30}S, ^{34}Ar, ^{40}Ca, ^{44}Ti, ^{52}Cr, and ^{62}Zn with $\log_{10}(\Delta X) \equiv \log_{10}\left(\frac{X_{\rm in}}{X_{\rm ex}}\right) \approx 0.5 - 1$. Both Lagrangian and Eulerian methods can suffer from numerical errors, though in different ways. Lagrangian tracer particles, used to compute the composition in post-processing, are more uncertain when tracking low density ejecta and especially the products of the α-rich freeze out, as shown in Harris et al. (2017). Furthermore, accurately representing features varying on short length and time scales such as the ones arising from multi-dimensional, potentially turbulent, flows can be difficult and require an exceedingly large number of tracers. The numerical diffusivity that Eulerian methods require for stability can lead to artificial mixing of species across the grid. While its importance decreases with increasing grid resolution, much finer grids than feasible are necessary to suppress this effect. This is the origin of the systematic disagreement between in situ and ex situ calculations in our models.

In 1D, the representation of the trajectories is much more simple, and accurate,

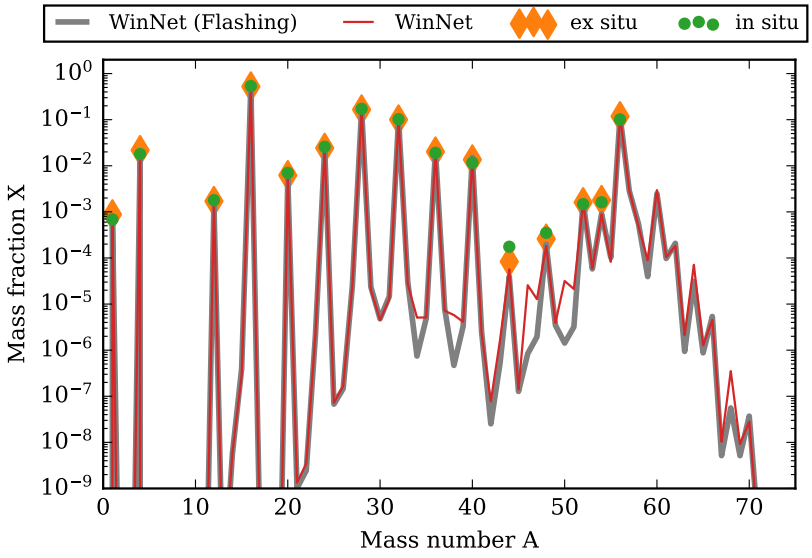

(a) 1D_RN16E

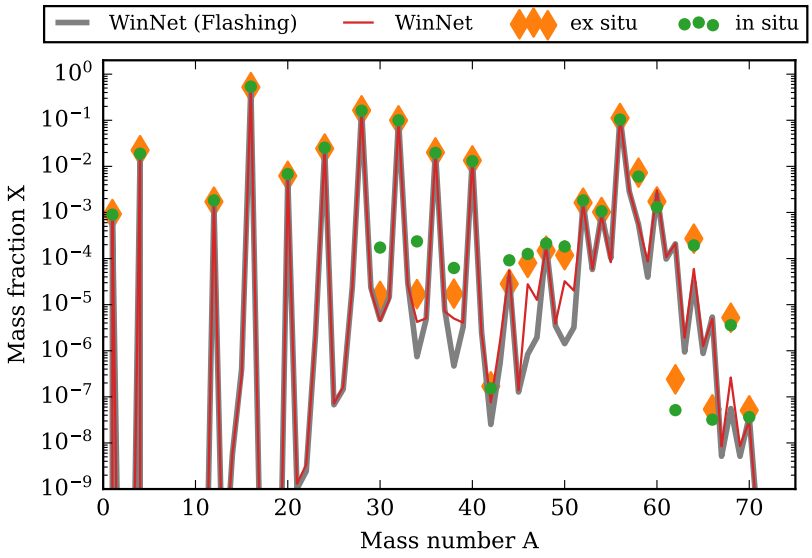

(b) 1D_RN94E

Figure 5.11: Integrated final ejecta composition of the 1D models. Red lines correspond to the composition obtained in post-processing with the full network WinNet in the 1D_RN16E (a) and 1D_RN94E (b). The post-processing results for the 1D_flsh are displayed in grey for comparison. Green dots stand for the values obtained from the network in situ, i.e. evolved in the simulation. The values obtained with the same reduced network in post-processing are depicted by orange diamonds.

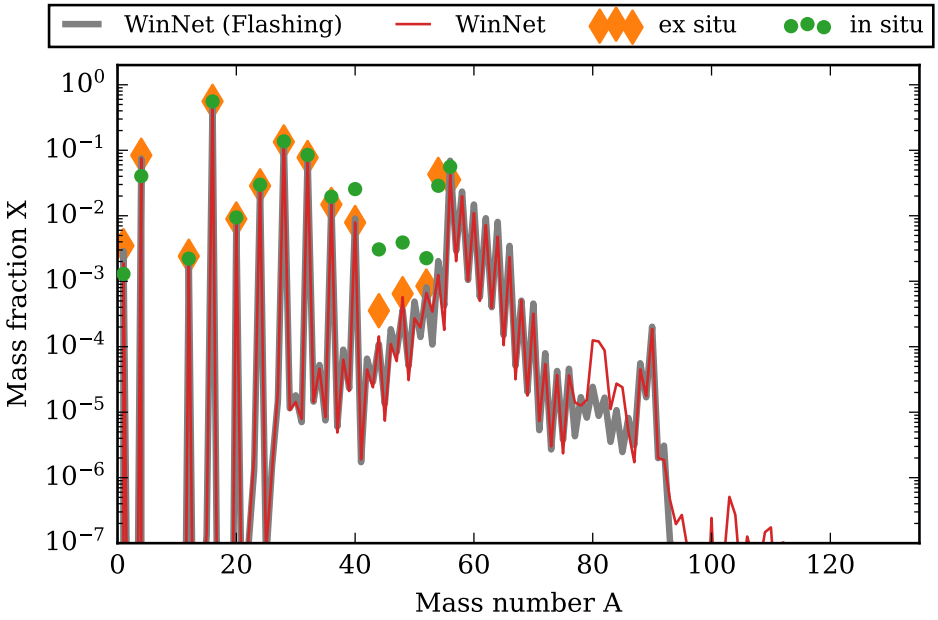

(a) 2D_RN16E

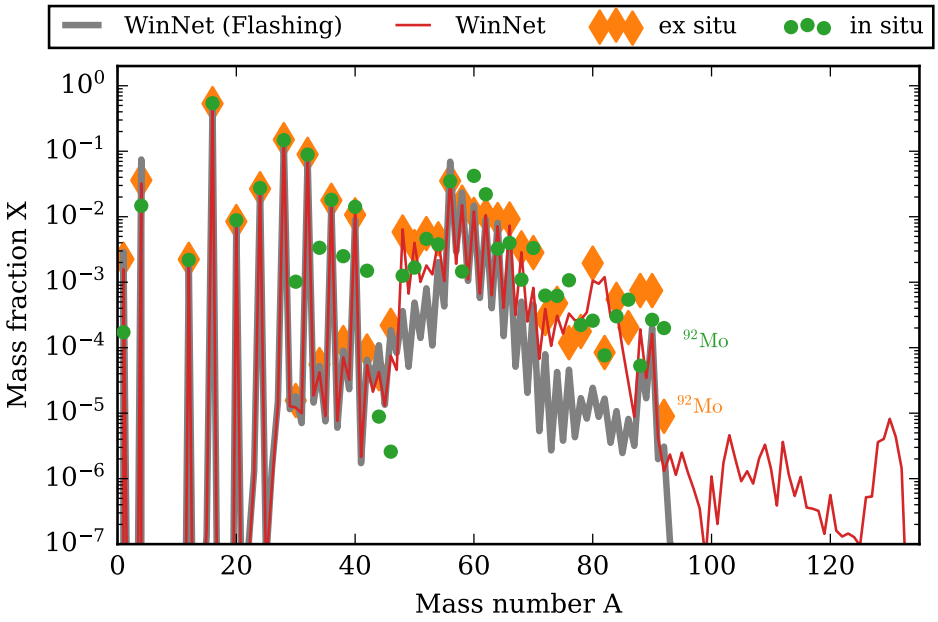

(b) 2D_RN94E

Figure 5.12: Integrated final composition of the 2D models. Analogously from Figure 5.11, the grey line corresponds to the post-processing calculation of model 2D_flsh.

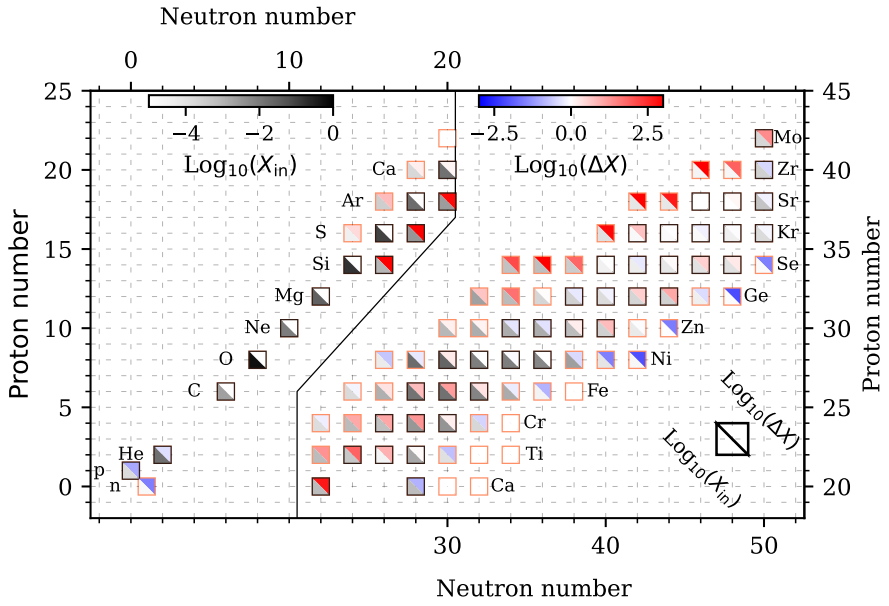

Figure 5.13: Chart with the RN94 isotopes in boxes. Orange edges indicate unstable nuclei and black stable ones. Bottom half of boxes depict in situ integrated mass fractions for 2D_RN94E at the end of the simulation. Upper half show the differences with respect to ex situ mass fraction, defined as $\Delta X = \frac{X_{\rm in}}{X_{\rm ex}}$, for species with $X_{\rm i} > 10^{-5}$.

reducing the uncertainty to that arising mainly from the aforementioned numerical diffusion. We therefore tested its impact based on the 1D_RN94E model by recalculating it with different resolutions of 500, 600, 700, and 1000 radial zones. While the ex situ abundances for all models were almost identical with maximum deviations of the order of $\sim 40\%$ for ^{42}Ti and ^{54}Ni, some elements (i.e., ^{30}S, ^{34}Ar, and ^{62}Zn) showed variations in the order of $\sim 60 - 75\%$ for the in-situ abundances. All other elements were converged also within the in-situ networks. The impact of numerical diffusion could be decreased in further studies by modifying the advection scheme of the composition (Plewa & Müller, 1999).

The 2D_RN16E model has differences of the same order as the previous ones in ^{40}Ca, ^{44}Ti, ^{48}Cr, and ^{52}Fe. The overproduction of such isotopes in situ is consistent with the explosion morphology seen in Figure 5.8. It is characterized by an extended high entropy and velocity shocked region where mainly α-rich freeze out takes place. The in situ and ex situ discrepancies in 2D_RN94E are depicted in Figure 5.13. Some differences in the overall nucleosynthesis trend can be observed by looking at the most neutron rich and deficient isotopes of Zn, Ge, Se, Kr, Sr, and Zr. The

post-processing underproduction of ^{44}Ti, ^{46}Ti, ^{48}Ti, ^{48}Cr, ^{50}Cr, ^{52}Cr, ^{54}Fe, and ^{56}Fe leads predominantly to a more neutron rich path with bottle necks in ^{80}Ge and ^{84}Se. In situ abundances show a tendency of being more neutron-deficient, starting from the aforementioned isotopes of Ti, Cr, and Fe. Figure 5.13 shows that matter accumulates at the proton-rich isotopes ^{72}Se, ^{74}Se, and ^{76}Se, suggesting that even the highly extended RN94 network still has some bottlenecks that could be better represented with an even more extended network. Finally, this more neutron-deficient path ends up producing more ^{92}Mo, $\log_{10}(\Delta X_{^{92}\mathrm{Mo}}) = 1.35$.

5.4 Summary & Conclusions

We have presented a detailed study of how the treatment of the composition within CCSN simulations impacts the explosion dynamics and nucleosynthesis.

We performed 1D and 2D CCSN simulations using the neutrino-hydrodynamics code Aenus-Alcar (Just et al., 2015; Just et al., 2018; Obergaulinger & Aloy, 2020). So far, this code included the nuclear reactions outside the NSE regime only via the simplified flashing scheme (Rampp & Janka, 2002), which assumes that the gas consists only of nucleons and a representative nucleus, for which, depending on the temperature, we use ^{28}Si or ^{56}Ni. We used the reduced network module ReNet (see Section 4.2) to replace the flashing scheme by a $16\,\alpha$-chain (RN16) and a 94 isotopes network (RN94). The latter is able to reproduce the main nucleosynthesis yields in standard CCSN explosions (e.g, Eichler et al., 2017). In addition, thanks to the 148 nuclei considered in steady state approximation, RN94 is the most extended network in the nuclear chart ever employed [4] in state-of-the-art hydrodynamic simulations. Both in-situ networks return the composition of the gas and the rate at which nuclear reactions generate or consume internal energy.

The different composition in the low-density region have an impact on the amount of nucleons, which can change the neutrino heating in the vicinity of the shock. This modifies the ram pressure outside of it and, therefore, its evolution.

We have demonstrated how the energy released in the nuclear reactions impacts the dynamics of the explosion. The energy generation in the pre-shocked collapsing matter decreases, again, the ram pressure outside the shock and allows it to expand easier, in agreement with Bruenn et al. (2006) & Nakamura et al. (2014). The nuclear energy released in the shocked region has a significant contribution, up to $20\,\%$, to the total explosion energy. The flashing scheme with ^{28}Si and ^{56}Ni is not able to reproduce the nuclear energy generation in this region, which leads 1D_flshE to a smaller explosion energy than 1D_RN16E and 1D_RN94E. Nevertheless, their overall evolution is similar. Differences between RN16 and RN94 are small regarding the nuclear energy generation, where (α, γ) and (p, γ) are the main production channels.

[4] To date of submission of the thesis. It should also be noted that in terms of the number of isotopes, the one of the Oak Ridge group (e.g., Bruenn et al., 2020) is larger, including 160 species.

While the models presented are not very energetic, we explored more energetic explosions, $E_{\rm exp} \sim 1\,\mathrm{B}$, and obtained similar impact.

Finally, we obtained the detailed nuclear yields of the models by applying the nuclear network WinNet with 6545 isotopes in an ex-situ, post-processing step to Lagrangian tracer particles tracking the fluid flow. We compared the post-processing results among different models and to the in-situ networks. In 1D, the differences are small since the $Y_{\rm e}$ involved are very similar among the models and close to 0.5. In 2D, the variation in abundances among different models get larger (Figure 5.12). The energy released in the nuclear reactions helps to sustain late neutron-rich outflows ejected from the vicinity of the PNS. The model 2D_RN94E shows how this mechanism allows weak r-process to take place. Moreover, we have compared the final composition obtained in situ and ex situ making use of RN16 and RN94. In agreement with Harris et al. (2017), we find significant discrepancies mainly in products of the α-rich freeze out, since Lagrangian tracer particles involve larger uncertainties when tracking such regions. For the in situ results, we identify the resolution-dependent numerical diffusion of species with low abundances as a factor contributing to the discrepancies. Also, we demonstrate how these uncertainties propagate, leading to variations on the nucleosynthesis path which alter the final yields.

What are the advantages and disadvantages of evolving a network in the simulations? While Lagrangian tracer methods and the ex situ results based on them are well suited for dense regions (e.g., Price & Federrath, 2010) and avoid the excess numerical diffusion that may beset grid-based Eulerian schemes and, consequently, in situ abundances, they lack mixing and are more uncertain in tracking low-density regions and their nucleosynthesis, e.g. products of the $\alpha-\mathrm{rich}$ freeze-out. This work suggests that it is necessary to employ in situ realistic networks in CCSN simulations with a fine grid resolution, or with a less numerically diffusive advection scheme, to obtain a realistic feedback of the energy generation, the neutrino opacities, and a more accurate ejecta composition. Thus, this study showed the strengths and weaknesses of employing networks in CCSN simulations and, hopefully, can help future simulations to decide depending on the goal of the study.

6 New EOSs in CCSNe

Observations of GWs (e.g., Abbott et al., 2017, 2020) and NICER (e.g., Miller et al., 2019; Riley et al., 2019; Raaijmakers et al., 2020) triggered even more interest of the community for the description of matter at high density, which has been hot for decades. Numerous constraints have been obtained from nuclear theory (for reviews see, e.g., Drischler et al., 2021; Kumar et al., 2023), experiments (e.g., Le Fèvre et al. 2016; Russotto et al. 2016; Reed et al. 2021, or, for a recent review, Kumar et al. 2023), and astrophysical observations (see, e.g., Özel & Freire, 2016; Watts et al., 2016; Baiotti, 2019, for reviews in the topic). However, there are still many uncertainties involved. Astrophysical sites like CCSNe or NSM reach extreme conditions that cannot be reproduced on earth. The dynamics and final observables of these events are critically impacted by the nuclear physics input, and hence, as already stated in previous chapters, they are considered laboratories to explore new physics.

In this chapter, we focus on the impact of different nuclear matter properties on CCSN simulations. In Section 6.1, we introduce the EOSs that we employ for our CCSN simulations, following Huth et al. (2021). In Section 6.2, we study the effects of several nuclear matter properties in CCSNe and show the preliminary results.

6.1 New EOSs

In this section we introduce the representative set of EOSs that we employ in this study. They were first presented in Huth (2023), and are built with the new parameterization of the effective mass and the EDF introduced in Huth et al. (2021).

6.1.1 Effective mass

Ab initio calculations from chiral EFT are able to compute the nuclear interaction up to $\sim 2n_0$ (for a review see, e.g., Machleidt & Entem, 2011). Carbone & Schwenk (2019) considered two- and three-body interactions from chiral EFT and employed finite-temperature self-consistent Green's function method (e.g., Dickhoff & Barbieri, 2004) to calculate the thermal effects on the EOS of dense matter. As mentioned in Section 3.3.4, the effective mass m^* (Equation (3.69)) is directly related to the thermal index $\Gamma_{\rm th}$ (see Equation (3.68)), that takes into account the thermal contribution to the EOS.

Huth et al. (2021) introduced a new parameterization of the effective mass, in order to reproduce the thermal effects from Carbone & Schwenk (2019) and to explore different scenarios at densities which ab initio calculations do not reach (i.e., beyond $\sim 2n_0$):

$$\frac{m_t^*}{m} = 1 + \left(\alpha_1 n_t + \beta_1 n_{-t} + \alpha_2 n_t^{4/3} + \beta_2 n_{-t}^{4/3} + \alpha_3 n_t^{5/3} \quad + \beta_3 n_{-t}^{5/3}\right) \frac{1}{1+e^{5n}} + \left(\epsilon_t \frac{n_t}{n} + \epsilon_{-t} \frac{n_{-t}}{n} - 1\right) \frac{1-e^{-10n}}{1+e^{-5(n-n_{\rm off})}} \,, \tag{6.1}$$

where m_t^* is the effective mass, and t indicates the isospin (p or n). The parameters $\alpha_i, \beta_i \in (1,3)$ are fit to reproduce the results of Carbone & Schwenk (2019) for PNM and SNM. They consider $\epsilon_t = \epsilon_{-t} = \epsilon$ in order for the effective mass to have the same high-density limit in PNM and SNM, and $n_{\rm off} = 0.7\,{\rm fm}^{-3}$. As mentioned previously, one of the goals of such parameterization is to investigate the thermal effects above $\sim 2n_0$. Hence, they employ three representative values in the high-density limit, $\epsilon \in \{0.7, 1.0, 1.3\}$, to encompass a wide range of possible behaviors at high densities, as shown in Figure 6.1. Notice that below $2n_0$ the behavior is the same for the three cases.

6.1.2 New energy per particle functional

In the Skyrme EDF (Equation (3.67)), the interaction part consists of a polynomial which is function of powers of the density and involves a high degree of fine-tuning. Hence, Huth et al. (2021) presented a new EDF in order to reduce the fine-tuning and to systematically produce EOSs that are constrained by nuclear physics, QCD calculations, and observations:

$$a\frac{E}{V}(n,x,T) = \sum_t \frac{\tau_t(n,x,T)}{2m_t^*(n,x)} - xn\Delta + \sum_i \left[\frac{a_i}{d_a + n^{(\delta_i-2)/3}} + \frac{4b_i x(1-x)}{d_b + n^{(\delta_i-2)/3}}\right] n^{1+\delta_i/3} \,, \tag{6.2}$$

with $i \in (1,4)$. Two different sets of density exponents δ_i are chosen:

$$\delta_{k_{\rm F}} = (3,4,5,6), \qquad \delta_n = (3,6,9,12). \tag{6.3}$$

The set of $\delta_{k_{\rm F}}$ exponents in the numerator correspond to integer powers of the Fermi momentum $k_{\rm F}$ at zero temperature (1, 4/3, 5/3, 2). With δ_n, the exponent in the numerator gets integer powers of n. The form of the denominator is chosen in order for the interaction part to be proportional to $n^{5/3}$ in the high-density limit to ensure the thermal index at this limit $\Gamma_{\rm th} \to \frac{5}{3}$ (e.g., Constantinou et al., 2015b). d_a and d_b are offset parameters to fit the EDF. Huth et al. (2021) considered $d_a = d_b = d$, and four different values that differ depending on the δ_i used:

$$d_{k_{\rm F}} \in \{1,3,5,7\}, \qquad d_n \in \{0.2, 0.4, 0.6, 0.8\}. \tag{6.4}$$

Finally, a_i and b_i are fit parameters to reproduce:

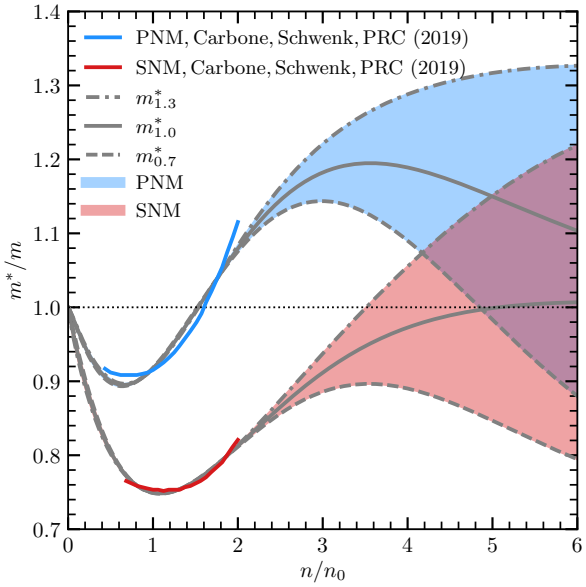

Figure 6.1: Effective mass in terms of the density for PNM and SNM. Grey solid line shows the case in which $m^*/m \to 1.0$ in the high-density limit. Grey dash-dotted line corresponds to $m^*/m \to 1.3$ case and dashed to $m^*/m \to 0.7$ case. The blue and red bands depict the region in the $m^*/m - n/n_0$ plan that the three scenarios span for PNM and SNM respectively. Blue and red solid lines show the results from Carbone & Schwenk (2019) up to $2n_0$. Figure from Huth et al. (2021)

1. Saturation density, binding energy, incompressibility, symmetry energy, and slope parameter: $(n_0, B, K, E_{\rm sym}, L)$.
2. PNM $E/A(n = 0.05\,{\rm fm}^{-3}) = 2.1\,{\rm MeV}$ (Gezerlis & Carlson, 2010).
3. $P^{\rm PNM}$ at $n \approx 8n_0$.
4. $P^{\rm SNM}$ at $n \approx 8n_0$.

The nuclear matter properties are varied within their uncertainties, and 3. and 4. are consistent with NS observations and 4. agrees with functional renormalization group (fRG) calculations (e.g., Leonhardt et al., 2020).

6.1.3 Representative set of EOSs

Huth et al. (2021) obtained a set of 16128 EOSs by combining the two different δ_i, the four different d, 12 variations of nuclear matter properties, the three different

effective mass cases, and 56 high-density fits for the pressure of PNM and SNM. Then, additional constraints were applied:

- EOS must be consistent with the theoretical PNM uncertainty band and the unitary gas bound for the energy per particle up to $0.2\,\mathrm{fm}^{-3}$
- It provides maximum NS masses of $M \gtrsim 1.965\,M_\odot$, which is the combined lower limit from the pulsar observations Antoniadis et al. (2013) and within 2σ from Cromartie et al. (2019).
- EOS must be within the 95% confidence interval of Raaijmakers et al. (2020), which constrained EOS properties with a joint analysis of NICER and LIGO/Virgo measurements.

A total of 4333 EOSs fulfilled the constrains. Among them, Huth (2023) selected only a representative set of EOSs in order to perform systematic studies by changing the nuclear matter properties individually and, therefore, allowing to study the impact of each of them on, e.g., CCSNe (see Section 6.2). The representative EOSs encompass the mass-radius (M-R) uncertainty band obtained by employing all 4333 physically motivated EOSs (see right panel of Figure 6.2). The boundary cases correspond to the soft and stiff EOS models, which produce the smallest and largest NS, respectively, among all of the EOSs, since they present the lowest and highest pressure over internal energy density (see left panel of Figure 6.2). The radii of the remaining EOS models lie between them in the M-R relation. In addition, fRG constraints to SNM have been applied to the extreme cases, resulting in the fRG soft and fRG stiff models.

In this thesis, we focus on a total of ten EOSs that can be catalogued in three different subsets, depending on the nuclear matter property that is systematically varied. All of them consider the new effective mass parametrization introduced in Section 6.1.1, and employ $m^*_{1.0}$. In a future work, we plan to study the effect of its variation.

First, we study the impact of the slope parameter L and the symmetry energy E_{sym} on the explosion and the PNS evolution. We include four different (E_{sym}, L) configurations to study the PNM characteristics (e.g. PNM_30/35):

- $(E_{\mathrm{sym}}, L)/\,\mathrm{MeV} \in \{(30, 35), (31, 55), (33, 65), (34, 55)\}$.

Furthermore, we check two different (K, n_0, B) configurations to explore SNM properties:

- $\mathrm{min} \mathrel{\widehat{=}} (K_{\mathrm{min}}, (n_0, B)_{\mathrm{max}}) = (175\,\mathrm{MeV}, 0.171\,\mathrm{fm}^{-3}, 16.43\,\mathrm{MeV})$.
- $\mathrm{central} \mathrel{\widehat{=}} (K, n_0, B)_{\mathrm{mean}} = (215\,\mathrm{MeV}, 0.164\,\mathrm{fm}^{-3}, 15.86\,\mathrm{MeV})$.

We name them SNM_min and SNM_central respectively. Finally, we explore four different combinations of the density exponents δ_i and the offset parameter d (e.g., δ_i_δ_{k_F}_$d3$). The EOS models are summarized in Table 6.1. The name of the EOS

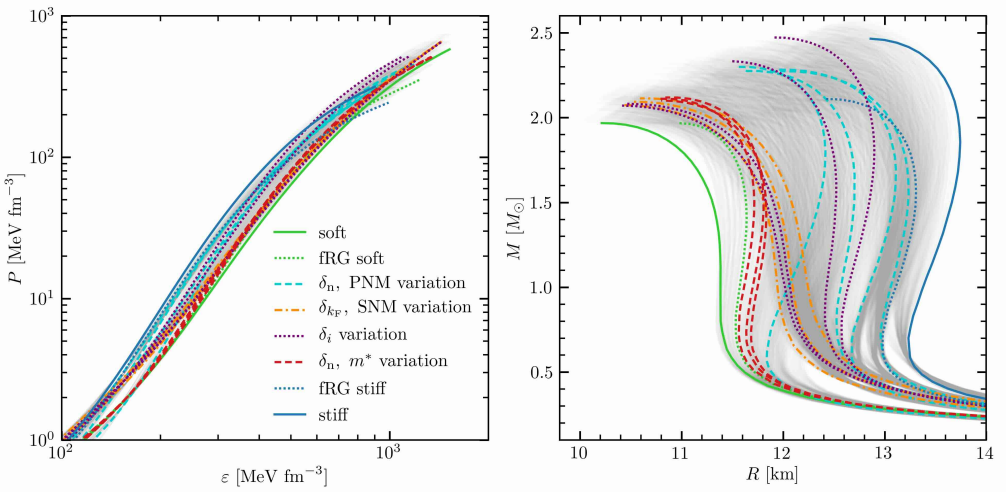

Figure 6.2: Left panel shows pressure as a function of the internal energy density for the representative EOS models. Right panel shows the M-R relation by employing each of them. In grey, the 4333 EOSs that fulfilled all constrains. Figure extracted from Huth (2023).

model indicates the nuclear property that is varied, i.e., PNM, SNM, or δ_i, and its value. For comparison, a version of the LS220 is included. All EOS tables were built by Yeunham Lim (Lim, 2012).

6.2 Impact on CCSN

In this section we study the impact of the new EOSs, introduced in Section 6.1.3, on CCSN.

We performed 1D CCSN simulations with AENUS-ALCAR for a total of $2\,\mathrm{s}$ in order to simulate beyond $1.5\,\mathrm{s}$ postbounce and the PNS to reach densities beyond $2\mathrm{n}_0$. As in Chapter 5, we consider the transition from the high-density to the low-density regime at $T_{\mathrm{th}} = 5.8\,\mathrm{GK}$, and $T_{\mathrm{inter}} = 5.0\,\mathrm{GK}$. In the latter, we use the RENET module presented in Chapter 4. In contrast to Chapter 5, in this chapter we use the same configuration at low temperatures and densities for all models. We employ the Helmholtz EOS with the RN16 network to take into account the main nuclear reactions involved and an approximate composition out of NSE. At high temperatures ($T > T_{\mathrm{th}}$) and densities, we vary the EOS table employed (see Table 6.1):

- To study the variation of PNM, we performed four simulations with the different EOSs: 1D_PNM_30/35, 1D_PNM_31/55, 1D_PNM_33/65, and 1D_PNM_34/55.
- We explore the impact of SNM properties with the models that include the

EOS	δ_i	d	n_0	B	K	$E_{\rm sym}$	L	$P^{\rm SNM}_{8n_0}$	$P^{\rm PNM}_{8n_0}$	$R_{1.4}$
PNM_30/35	δ_n	0.4	0.164	15.86	215	30	35	600	800	12.38
PNM_31/55	δ_n	0.4	0.164	15.86	215	31	55	600	800	13.05
PNM_33/65	δ_n	0.4	0.164	15.86	215	33	65	600	800	13.21
PNM_34/55	δ_n	0.4	0.164	15.86	215	34	55	600	800	12.69
SNM_min	$\delta_{k_{\rm F}}$	3	0.171	16.43	175	34	55	800	1050	11.86
SNM_centr	$\delta_{k_{\rm F}}$	3	0.164	15.86	215	34	55	800	1050	12.00
δ_i_$\delta_{k_{\rm F}}$_$d3$	$\delta_{k_{\rm F}}$	3	0.164	15.86	215	34	55	800	1000	11.72
δ_i_$\delta_{k_{\rm F}}$_$d5$	$\delta_{k_{\rm F}}$	5	0.164	15.86	215	34	55	800	1000	11.70
δ_i_δ_n_$d.4$	δ_n	0.4	0.164	15.86	215	34	55	800	1000	12.7
δ_i_δ_n_$d.6$	δ_n	0.6	0.164	15.86	215	34	55	800	1000	12.41
LS220	-	-	0.155	16.0	220	29.6	73.7	-	-	12.8

Table 6.1: EOS parameters for the set of representative EOS. The units are fm$^{(2-\delta_i)}$ for d, fm^{-3} for n_0, MeV for $B, K, E_{\rm sym}, L$, $\mathrm{MeV\,fm}^{-3}$ for the pressure of SNM and PNM at $8n_0$. The last column shows the radius, in km, obtained for a cold NS of $1.4\,M_\odot$ by employing each EOS. All EOSs, except LS220, employ the new effective mass parametrization with $m^*_{1.0}$.

different (K, n_0, B) configuration: 1D_SNM_min, and 1D_SNM_centr.

- We performed four simulations to explore the impact of δ_i and d variation: 1D_$\delta_{\rm i}$_$\delta_{\rm k_F}$_d3, 1D_$\delta_{\rm i}$_$\delta_{\rm k_F}$_d5, 1D_$\delta_{\rm i}$_$\delta_{\rm n}$_d.4, 1D_$\delta_{\rm i}$_$\delta_{\rm n}$_d.6.

- Finally, we include a model with the LS220 for comparison, 1D_LS220.

The composition at $T > T_{\rm th}$ is provided by the EOS table in the SNA approximation, which considers neutrons, protons, alpha particles and a characteristic nucleus in equilibrium. We chose a heating factor of $HF = 2.8$ to trigger the explosion, at least, for the 1D_LS220 model.

In this chapter we focus on the high-density regime of the simulation at relatively long times. Therefore, we need to resolve very well the PNS in order to avoid numerical instabilities originated in the steep density gradient present on its surface. Thus, we employ a high-resolution grid with $n_r = 1000$ cells logarithmically spaced in the radial direction and a central width of $\Delta r = 200\,\mathrm{m}$.

In Table 6.2, we list the 1D CCSN models with several explosion properties.

Model	R_{PNS}	M_{PNS}	E_{expl}	^{56}Ni	^{44}Ti
1D_PNM_30/35	17.9	1.663	1.63	2.33	4.21
1D_PNM_31/55	18.5	1.659	0.98	2.28	2.61
1D_PNM_33/65	18.7	1.658	0.96	2.43	2.20
1D_PNM_34/55	18.5	1.660	1.02	2.21	2.70
1D_SNM_min	15.7	1.813	-	-	-
1D_SNM_centr	17.7	1.625	1.83	3.82	3.92
1D_δ_{i}_$\delta_{\mathrm{k_F}}$_d3	17.5	1.625	1.83	3.81	3.92
1D_δ_{i}_$\delta_{\mathrm{k_F}}$_d5	17.5	1.623	1.88	3.81	4.21
1D_δ_{i}_δ_{n}_d.4	18.9	1.668	3.55	4.11	7.40
1D_δ_{i}_δ_{n}_d.6	18.5	1.651	1.71	2.92	4.23
1D_LS220	17.7	1.621	2.32	3.81	5.18

Table 6.2: Radius (km) and mass ($\mathrm{M}_\odot$) of the PNS, explosion energy ($10^{50}\,\mathrm{erg}$), and ^{56}Ni and ^{44}Ti ejected masses ($10^{-2}\,\mathrm{M}_\odot$ and $10^{-5}\,\mathrm{M}_\odot$, respectively) at the end of the simulation.

6.2.1 Variation of PNM properties

We first focus on the impact of the slope parameter L on the dynamics of the explosion. In Figure 6.3, we observe the behavior of the pressure as a function of the density. The pressure follows the L hierarchy. That is the expected outcome, since the PNS interior is neutron rich, and from Equation (3.66) we know that $P(\beta = 1) \propto L$. A smaller L produces a lower pressure that favors a faster contraction of the PNS (see Figure 6.4). The faster contraction increases the temperature of the PNS. Because of this, and due to $R_{\nu_e} \sim R_{\mathrm{PNS}}$, the neutrinos decouple at higher temperatures and therefore are more energetic (Figure 6.5). As a consequence, the energy deposited by neutrinos in the gain layer is larger, which leads the shock to revive and expand faster (see Figure 6.6). One may notice that the PNS contraction and, therefore, the shock expansion for the model 1D_LS220 is significantly different. It is because of the different parametrization of the effective mass, and hence, a different thermal contribution (Schneider et al., 2019; Yasin et al., 2020).

Furthermore, the lower central pressure allows more matter to accrete onto the PNS, and, thus, the PNS to reach a higher central density (upper panel of Figure 6.7). This forms a more compact and massive remnant (see Table 6.2), which is correlated with the diagnostic explosion energy and the amount of ^{44}Ti synthesized during the

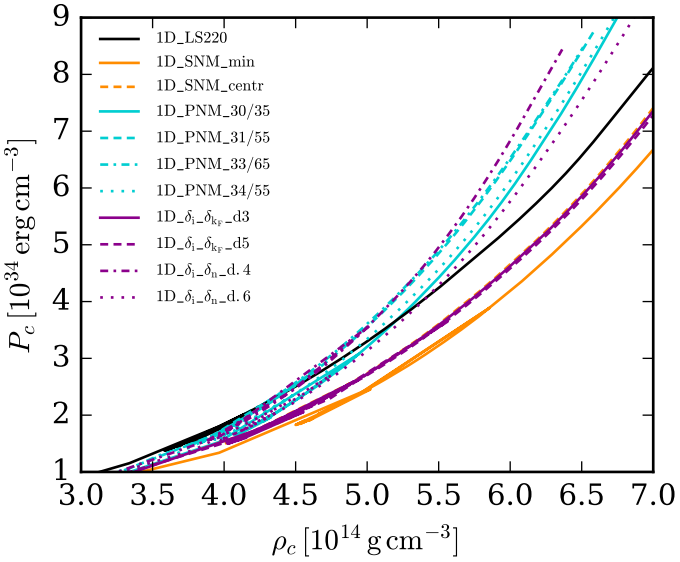

Figure 6.3: Central pressure evolution over central density reached in the simulation.

first $\sim 1.5\,\mathrm{s}$. As pointed out previously, the faster contraction increases T_c. Since the models that vary PNM properties consider the same effective masses, they have the same thermal contribution (Equation (3.68)) (e.g., Yasin et al., 2020). Therefore, the evolution of T_c is governed by the dynamic evolution of the PNS (i.e. its contraction), and, thus, it scales like ρ_c.

The central entropy, up to $\sim 0.8\mathrm{s}$ postbounce, depends mostly on the symmetry energy, in agreement with Bethe et al. (1979); Mazurek et al. (1979); Yasin et al. (2020). At later times, the entropy can be approximated to $S_c \sim m^* T_c/\rho_c^{2/3}$ by considering Fermi liquid theory (Baym & Pethick, 1991). Therefore, the entropy follows a similar trend as the temperature.

At high densities, i.e., above n_0, a higher slope parameter L leads to a larger difference between the energy per particle of PNM and SNM. Therefore, for larger L, the system has to overcome a larger energy to become more asymmetric. As a consequence, Y_{e_c} follows the L hierarchy as we show in Figure 6.7. In addition, neutrinos in the PNS interior are trapped, so the Y_{e_c} does not change significantly due to them.

At fixed L, the pressure is decreased by a larger E_{sym}, since the slope of E/A decreases to fit at the same high-density limit. We show this by comparing the central pressure of 1D_PNM_34/55 to 1D_PNM_31/55. The lower pressure leads, as discussed above, to a faster PNS contraction, a more energetic explosion and a more compact object. However, the impact of the variation of E_{sym} is much smaller than the change in L.

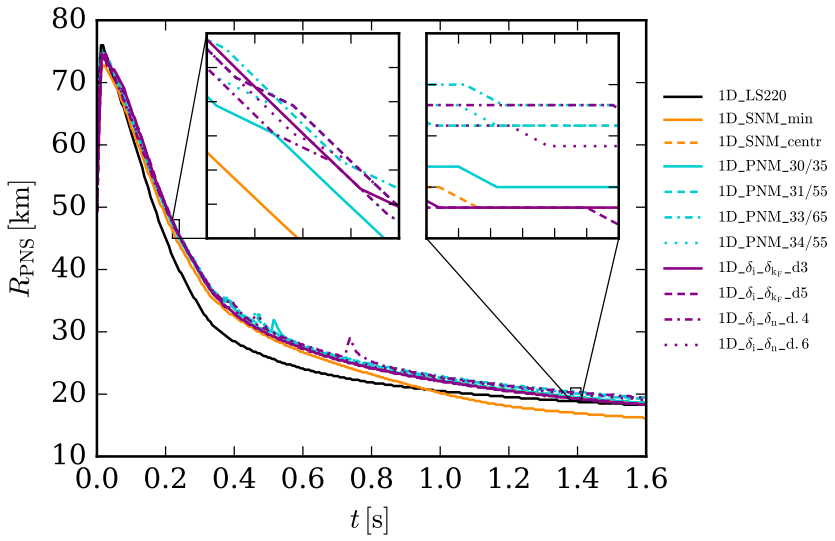

Figure 6.4: Evolution of the PNS radii.

Finally, the variation in PNM properties is also reflected in GW frequencies. We use the universal relations from Sotani & Sumiyoshi (2019); Sotani et al. (2021) and Torres-Forné et al. (2019) to compute them. The ${}^2f$, ${}^2p_1$, ${}^2p_2$, and ${}^2p_3$ modes depend on the local sound speed, that is given by the derivative of the pressure with respect to the energy density, and density inside the shock. However, the simple formulae of these relations do not consider that, and employ $R_{\rm PNS}$, $M_{\rm PNS}$, $R_{\rm shock}$, and $M_{\rm shock}$ to mimic the frequency behavior. In the case of ${}^2f$ (Sotani & Sumiyoshi, 2019; Sotani et al., 2021):

$$f_f(\mathrm{kHz}) = 0.9733 - 2.7171x + 13.7809x^2, \tag{6.5}$$

where $x \equiv \left(\frac{M_{\rm PNS}}{1.4\,M_\odot}\right)^{1/2}\left(\frac{R_{\rm PNS}}{10\,\mathrm{km}}\right)^{-3/2}$. As a consequence, the frequency evolution is directly related with the contraction of the PNS and its final compactness. Hence, even though the frequencies of the ${}^2f$ modes in the four models are very similar, they follow the inverse L hierarchy (see bottom left panel of Figure 6.7). On the other hand, ${}^2g_1$ and ${}^2g_2$ modes are produced in the PNS interior due to buoyancy, and depend mainly on the PNS surface gravity (e.g., Torres-Forné et al., 2019; Jakobus et al., 2023). For ${}^2g_1$ modes, we use the following expression (Torres-Forné et al., 2019):

$$f_{g_1}(\mathrm{Hz}) = 8.67 \cdot 10^5 x - 51.9 \cdot 10^6 x^2, \tag{6.6}$$

with $x \equiv M_{\rm PNS}/R^2_{\rm PNS}$. As expected, the ${}^2g_1$ modes present higher frequencies for smaller L (see bottom right panel of Figure 6.7). Consistently, the effect of $E_{\rm sym}$ is subdominant and only noticeable at fixed L: model 1D_PNM_34/55 present higher ${}^2g$ mode frequencies than model 1D_PNM_31/55.

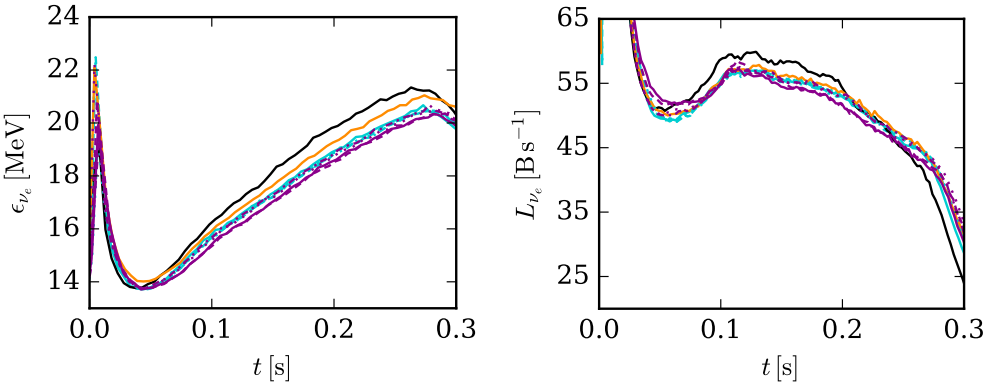

Figure 6.5: Electron flavor neutrinos mean energy (left) and luminosity (right).

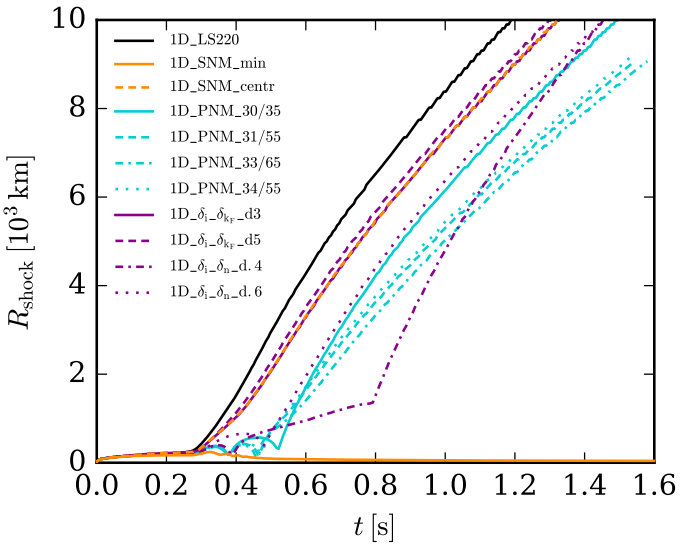

Figure 6.6: Shock evolution of the different models.

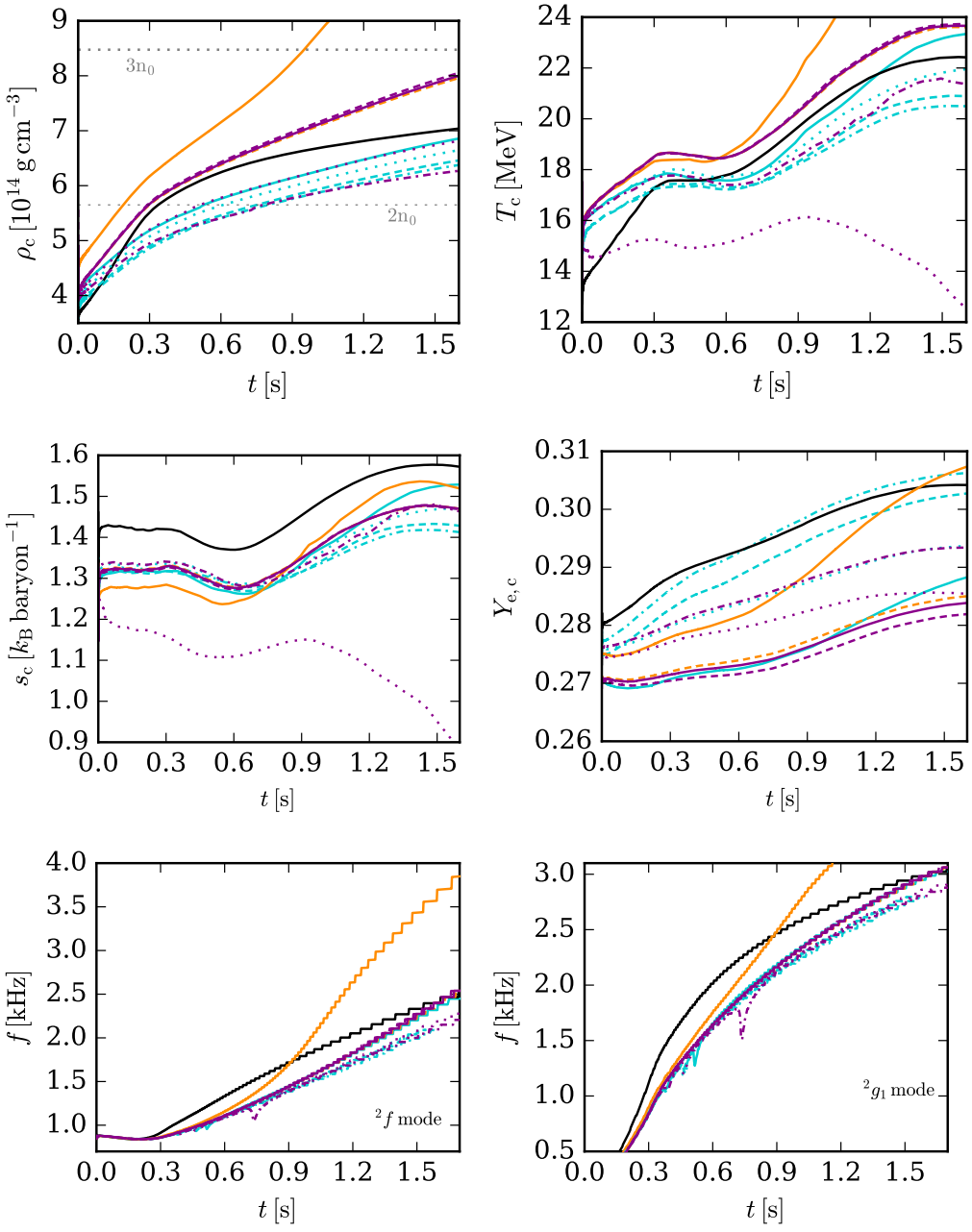

Figure 6.7: Evolution of the central density and the central temperature. Central entropy and Y_e evolution of all models. In the left panel we show the ^2f mode frequency. It is calculated employing Sotani & Sumiyoshi (2019); Sotani et al. (2021). The right panel shows the frequency evolution of the $^2g_1$ mode, computed with Torres-Forné et al. (2019).

To summarize, the postbounce explosion dynamics are quite sensitive to the slope parameter, since it is proportional to the pressure of PNM and, therefore, play a key role in the contraction of the PNS, and to the evolution of the shock.

6.2.2 Variation of SNM properties

Now we focus on the impact SNM has on CCSNe. For this purpose, we explore the two different configurations of (K, n_0, B) with the models 1D_SNM_min and 1D_SNM_centr. As we show in the following, the onset of the explosion is extremely sensitive to these properties.

SNM_min shows the lowest E/A, since it has the lowest K and the largest B. In addition, it presents the lowest pressure over density (Figure 6.3). The lowest E/A and pressure produce the fastest collapse among all models and allow for the highest central densities at bounce (Figure 6.7). The densest PNS results in a less dense gain region. Consequently, the gain region shows a lower pressure that is determinant for the non-revival of the shock. As we show in the left panel of Figure 6.8, the neutrino energy deposition in the gain layer of models 1D_SNM_centr and 1D_SNM_min is very similar, and they only start to differ when their shock evolution already significantly differs, short before $t \sim 0.3\,\mathrm{s}$. The neutrino energy deposition in model 1D_SNM_centr drops drastically since the shock revives and expands, while in model 1D_SNM_min the heating stays at the same order of magnitude because of the stagnation of the shock. However, the pressures and internal energies are significantly different. The right panel of Figure 6.8 shows the pressure differences, defined as:

$$\Delta P \equiv \frac{P^{\mathrm{1D\_SNM\_min}} - P^{\mathrm{1D\_SNM\_centr}}}{P^{\mathrm{1D\_SNM\_min}}} \cdot 100 \tag{6.7}$$

The pressures (and hence the internal energy of the fluid) in the gain region of 1D_SNM_min are $\sim 30\%$ lower, and a comparable neutrino energy deposition is not enough to revive the shock.

The failed explosion in 1D_SNM_min allows the central densities to grow up to $\rho_\mathrm{c} \sim 3.8\,n_0$ and the central temperatures up to $T_\mathrm{c} \sim 28\,\mathrm{MeV}$ at the end of the simulation. Thus, model 1D_SNM_min produces the most compact remnant of our study. This is consistent with the fact that it presents the lowest K, which translates into lower pressures when increasing the density, i.e. a softer EOS. The higher B and lower K leads to a larger energy difference between PNM and SNM in the *min* configuration than in the *central*. Therefore, the system needs a higher energy to become more asymmetric and, thus, 1D_SNM_min shows higher central Y_e.

Finally, this model shows the highest GW frequencies. As we showed in Section 6.2.1, the evolution ${}^2f$ and ${}^2g$ modes of the GWs depends mainly on the PNS contraction, its compactness, and its surface gravity (see Equation (6.6)).

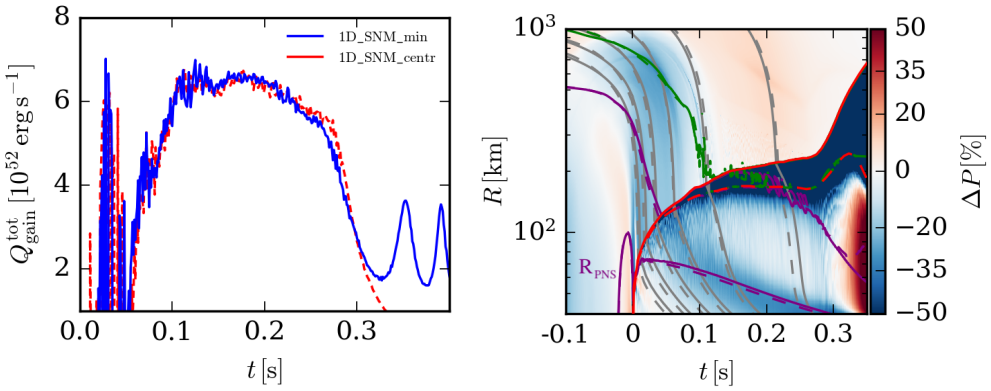

Figure 6.8: Left panel shows the integrated neutrino heating in the gain region for the 1D_SNM_min and the 1D_SNM_centr models. Right panel shows the differences in pressure of both models (defined in Equation (6.7)). Grey lines depict the mass shell evolution of 1D_SNM_centr (solid) and 1D_SNM_min (dashed). Red lines show the shock evolution. Isodensities $\rho = \{10^9, 10^{11}\}\,{\rm g\,cm^{-3}}$ are shown in purple. Finally, green lines correspond to $T = 5\,{\rm GK}$.

6.2.3 Variation of the density exponents

In this section, we focus on the impact of the choice of the different density exponent set in the EOS parametrization, $\delta_{k_{\rm F}}$ and δ_n, and the choice of different offset parameter d.

All of the models considered in this section produce successful explosions (Figure 6.6). In $1{\rm D}\_\delta_{\rm i}\_\delta_{k_{\rm F}}\_{\rm d}3$ and $1{\rm D}\_\delta_{\rm i}\_\delta_{k_{\rm F}}\_{\rm d}5$, the shock expands shortly after stalling, after $t \sim 0.3\,{\rm s}$. Although both $1{\rm D}\_\delta_{\rm i}\_\delta_{\rm n}\_{\rm d}.4$ and $1{\rm D}\_\delta_{\rm i}\_\delta_{\rm n}\_{\rm d}.6$ models experience a fallback, the shock evolution of the former is quite different. It almost stalls during $\sim 200\,{\rm ms}$, when starts to expand linearly. After $\sim 800\,{\rm ms}$, the explosion is finally triggered. The late shock revival allows for a higher neutrino energy deposition in the gain layer, and, as a consequence, this model produces the most energetic explosion and the largest production of $^{56}{\rm Ni}$ (Table 6.2). Moreover, the latest onset of the explosion allows the ^2g modes to grow in frequency since the densities involved in the gain region increase. The shock evolution of all models is consistent with the contraction of the PNS (Figure 6.4). As mentioned previously, a faster contraction leads to an emission of more energetic neutrinos that are absorbed in the gain layer and revive the shock.

The models that include the δ_n set show higher central pressures over densities than the models with $\delta_{k_{\rm F}}$ (Figure 6.3), which is consistent with the shock evolution of all of them. Furthermore, the former show to be stiffer. The impact of the offset choice

is different in the two sets of δ_i. The $\delta_{\rm i}\_\delta_{\rm n}\_{\rm d}.4$ EOS leads to higher pressures than $1{\rm D}\_\delta_{\rm i}\_\delta_{\rm n}\_{\rm d}.6$, while $\delta_{\rm i}\_\delta_{{\rm k}_{\rm F}}\_{\rm d}3$ and $\delta_{\rm i}\_\delta_{{\rm k}_{\rm F}}\_{\rm d}5$ show very similar ones, slightly higher in the latter. The evolution of the central densities and temperatures follow inversely the pressure hierarchy (Figure 6.7). However, in the preliminary results shown in this section, the model $1{\rm D}\_\delta_{\rm i}\_\delta_{\rm n}\_{\rm d}.6$ presents an unusual $T_{\rm c}$ and $S_{\rm c}$ evolution, where the PNS seem to experience a fast cooling. A further, more detailed, study of this case will be necessary. As expected, the higher pressures in the EOSs that include δ_n lead to larger remnants. Model $1{\rm D}\_\delta_{\rm i}\_\delta_{\rm n}\_{\rm d}.4$ shows the largest $R_{\rm PNS}$ at the end of the simulation.

We notice that EOSs $\delta_{\rm i}\_\delta_{\rm n}\_{\rm d}.4$ and PNM_34/55 are very similar, since they only differ in the pressure of SNM and PNM they are fit at $8n_0$. $\delta_{\rm i}\_\delta_{\rm n}\_{\rm d}.4$ is fit to higher pressures. This leads $1{\rm D}\_\delta_{\rm i}\_\delta_{\rm n}\_{\rm d}.4$ to higher pressures, and, hence, lower densities. The central Y_e in both models is identical, which is consistent with the same energy they have to employ to make the system more (or less) asymmetric. Again, the larger pressure in $\delta_{\rm i}\_\delta_{\rm n}\_{\rm d}.4$ produces a larger remnant.

Finally, SNM_centr has almost the exact same parametrization as $\delta_i\_\delta_{k_{\rm F}}\_d3$, so all of the explosion properties of the CCSN models that include them are very similar. However, the former has a slightly higher pressure of PNM at $8n_0$, while the SNM part is identical. This leads to a slightly larger PNS and a slightly higher Y_e for the model 1D_SNM_centr.

6.3 Summary & Outlook

In this chapter, we have employed the state-of-the-art EOSs tables from Huth (2023) to perform a systematic study of the effects of several nuclear matter properties on CCSNe. In particular, we have explored the variation of the slope parameter L, the symmetry energy $E_{\rm sym}$, the incompressibility K, and the density exponent of the EDF introduced in Huth et al. (2021).

Our CCSN models are consistent with the characteristics of the different EOS, that were selected to encompass a broad range in the M-R uncertainty band. Models that present a higher pressure per density lead to lower central densities (e.g., Sumiyoshi et al., 2005; Marek et al., 2009), since it counterbalance the gravity, and, therefore, produce a slower collapse and lower central densities at bounce. In addition, they exhibit a slower contraction of the PNS that leads to a later shock revival, since the neutrinos are less energetic because they decouple at lower temperatures. In contrast, softer EOSs allow for higher central densities due to the smaller pressures. These models present a faster contraction and, therefore, a faster shock expansion that usually involve a more energetic explosion and, therefore, a larger amount of ^{56}Ni and ^{44}Ti yields. At latest times, the high densities achieved due to soft EOSs produce a more compact object, as expected. In Table 6.2 we show that the mass and radius of the PNSs at the end of the simulation present the same exact hierarchy as the one

followed by the radius of a cold NS of $1.4\,M_{\odot}$.

We find that the slope parameter L has a significant impact on the explosion dynamics and the final remnant. The higher pressure per density involved for larger L leads to slower PNS contraction and shock expansion. Therefore, a smaller L leads to a more compact PNS. In addition, the Y_e follows the L hierarchy since the difference between PNM and SNM increases. The impact of E_{sym} is subdominant with respect to L.

The dynamic evolution is quite sensitive to SNM properties. The two different (K, n_0, B) values explored lead to very different evolution, in contrast to previous works that suggest that the incompressibility does not have a big impact in the shock dynamics (e.g., Swesty et al., 1994; Thompson et al., 2003). The model 1D_SNM_min presented a fast collapse that produced the densest PNS from bounce. This resulted in a less dense gain region and, therefore, lower pressures below the shock. Since the neutrino energy deposition was similar, the system did not have enough energy to revive the shock and, thus, the model showed no explosion.

Our results suggest that the impact of PNM matter properties could be subdominant with respect to the effective mass, since the evolution of the PNS contraction, the central quantities, and the GW frequency are highly impacted by it. Moreover, the 1D_LS220 model behaved significantly different from the others due to its different m^* parametrization that accounts for a different thermal contribution. This would agree with previous studies (e.g., Schneider et al., 2019; Yasin et al., 2020), that showed that these effects are dominant. Thus, in a future work, we plan to extend our study to the complete set of EOSs presented in Huth (2023), and to study the impact of the effective mass in the dynamics of the explosion with the parametrization from Huth et al. (2021); Carbone & Schwenk (2019).

7 Three-dimensional CCSN simulation

In the last decade, the first 3D CCSN simulations including state-of-the-art neutrino transport became feasible thanks to the new computational facilities (for reviews in the topic see, e.g., Janka et al., 2016; Müller, 2020; Burrows & Vartanyan, 2021). However, 3D simulations still need to employ approximations to tackle the huge computational cost. The different groups consider various approaches to compromise accuracy for performance. In Figure 7.1, we depict the strengths and weaknesses of several state-of-the-art models. With the implementation of ReNet in Aenus-Alcar, our goal is to "expand" the nucleosynthesis branch keeping the M1 neutrino treatment for the first second post-bounce. This is an important feature for a consistent nucleosynthesis calculation, since neutrinos are key to set the electron fraction of the ejecta. The Oak Ridge group, as mentioned in Chapter 5, evolve a large nuclear network in their simulations (Bruenn et al., 2020). However, Sandoval et al. (2021) only evolve the first $\sim 280\,\mathrm{ms}$ post-bounce including a sophisticated neutrino scheme and after that evolve the system substituting the PNS for an inner boundary condition. Thus, we consider that our ongoing and planned 3D models will suppose an advancement in the field.

As stated in previous chapters, non-radial deformations such convection, turbulence, and SASI are key to trigger the explosion. As a first approach 2D models allow to include these effects at a reasonable computational cost. However, the behavior of a fluid is different in 2D with respect to 3D. First, the axisymmetry imposed in such simulations drives the explosion towards the poles, as we observed in Chapter 5. 3D models, in contrast, do not have any preferred axis and hence the global expansion of the shock resembles more spherical (e.g., O'Connor & Couch, 2018), since it is dominated by asymmetries at intermediate and small scales rather than the dipolar or quadropolar morphology in 2D. Furthermore, some dynamical features of 2D models may very well be artifacts of axisymmetry. For example, 3D could presumably avoid the late-, fast-, low-Y_e outflows that we observed[1] in our 2D models in Chapter 5, consequence of the strong inflows that squeeze the polar region of the PNS.

In addition, there are effects that make 3D models harder to explode[2] than 2D (Hanke et al., 2012; Couch, 2013; Couch & O'Connor, 2014). In 3D, the (kinetic) energy in the turbulent post-shock region is transported towards smaller scales (Kolmogorov, 1941), the so-called direct energy cascade. Oppositely, in 2D, the energy is

[1] Other groups also noticed this behavior in 2D.
[2] This question is still being debated nowadays.

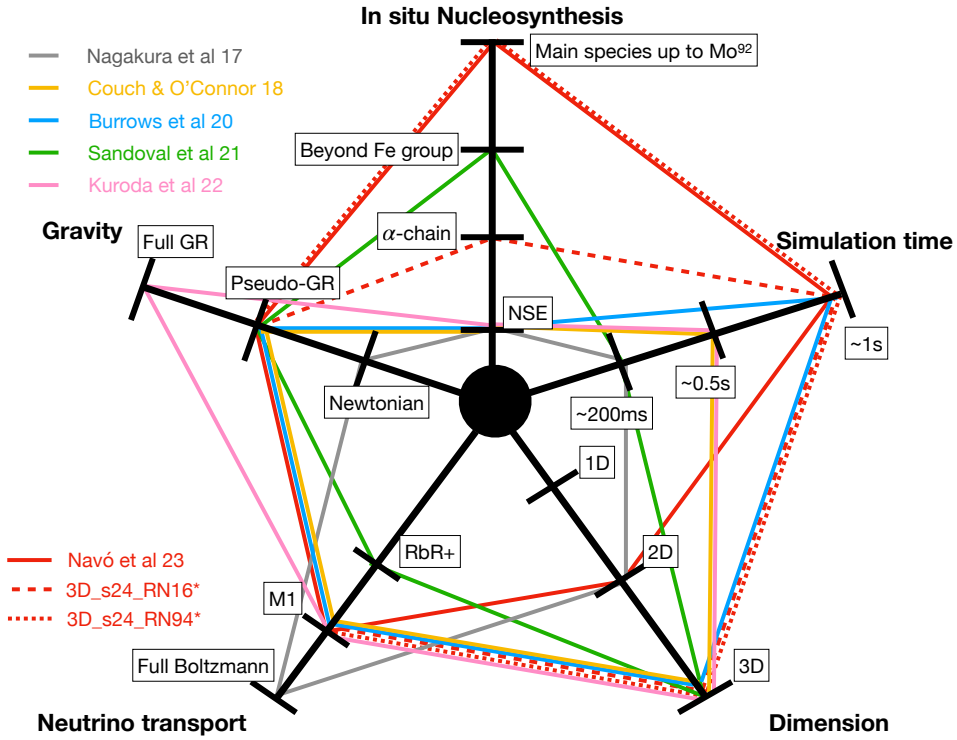

Figure 7.1: Overview of the physics included in several state-of-the art, multi-dimensional, neutrino-driven CCSN simulations. We consider the following works Nagakura et al. (2018); O'Connor & Couch (2018); Burrows et al. (2020); Sandoval et al. (2021); Kuroda et al. (2022); Navó et al. (2023). In addition, we add the ongoing 3D_s24_RN16 and the future 3D_s24_RN94 introduced in this chapter. Figure inspired and adapted from Obergaulinger & Reichert (2023).

carried from small to larger structures (inverse energy cascade (Kraichnan, 1967)), and thus, 2D models are more effective at reviving the shock. In summary, the full multi-dimensional nature of the explosion can only be captured in 3D.

In this chapter, we perform the first 3D CCSN simulation with Aenus-Alcar that includes the reduced nuclear network module, introduced in Chapter 4. The aim of this chapter is to obtain a more realistic model which, at the same time, can provide a benchmark for studies based on computationally cheaper one- and two-dimensional models. It is the natural continuation of Chapter 5. Thus, we extend our study performed in 1D and 2D to more realistic 3D CCSN models.

In Section 7.1, we introduce the model, and in Section 7.2 we present the preliminary results of the first $t_{\mathrm{pb}} = 241\,\mathrm{ms}$ of evolution.

7.1 Model

3D simulations are extremely computationally expensive due to, mostly, the neutrino transport and the high sound speeds in the PNS. The RN94 network, although improving the treatment of the composition, it is sufficiently large to slow down the simulation substantially. In contrast, the RN16 network does not show significant run time differences with the flashing scheme. Therefore, due to the limited computational resources, we employ the simpler RN16 network. Nevertheless, as shown in Chapter 5, we take into account the reactions responsible for most of the nuclear energy released in the explosion.

As in Chapter 5, we consider $T_{\rm th} = 5.8\,{\rm GK}$ and $T_{\rm inter} = 5.0\,{\rm GK}$. For $T > 5.8\,{\rm GK}$, we employ the SFHo EOS and consider NSE. When $T \leq 5.8\,{\rm GK}$, we evolve the composition with RN16. We consider the nuclear energy generation for temperatures below $T_{\rm inter} \leq 5.0\,{\rm GK}$. We employ a grid of $400 \times 64 \times 128$ zones in radial (logarithmically spaced), θ, and ϕ direction, and 12 energy bins for the neutrinos. The radial component has a central width of $\Delta = 400\,{\rm m}$ and encompasses the star up to an out radius $R_{\rm out} \simeq 9 \cdot 10^4\,{\rm km}$. This time, we choose the s24 progenitor from Woosley et al. (2002), since, in 1D, it produces especially energetic explosions (Jost, 2022) that captured our attention, and motivated us to produce a self-consistent 3D model from it. Therefore, we do not apply any artificial heating and set $HF = 1$. We do not consider rotation nor magnetic fields. We name this model 3D_s24_RN16.

We evolved the initial progenitor collapse in 1D until $16\,{\rm ms}$ post-bounce. Then, we mapped it to our 3D set up. In order to obtain the nucleosynthesis from this model, we plan to run them, at least, up to $1\,{\rm s}$ post bounce. For now, we are able to show the first $241\,{\rm ms}$ of evolution.

The scheduled model with the RN94 (3D_s24_RN94) will allow us to evolve the composition with an unprecedented accuracy in a 3D model. However, we have not been able to perform this simulation yet due to limited computational resources.

7.2 Early post-shock evolution

In this section, we show the preliminary results of the first $241\,{\rm ms}$ of evolution of 3D_s24_RN16.

In Chapter 2, we have already introduced the importance of heating and advective timescales in the gain region (see Equations (2.8) and (2.9)). When the heating timescale is shorter than the advective, the shock is more likely to successfully revive. In this chapter, we use them to predict if our model produces an explosion. Here, we employ an alternative definition of the advective timescale (e.g., Scheck et al., 2007), which essentially considers the accretion of matter into the cooling region:

$$\tau_{\rm adv} \equiv \frac{\langle R_{\rm shock} \rangle - \langle R_{\rm gain} \rangle}{\langle v_{\rm r}^{\rm gain} \rangle}. \tag{7.1}$$

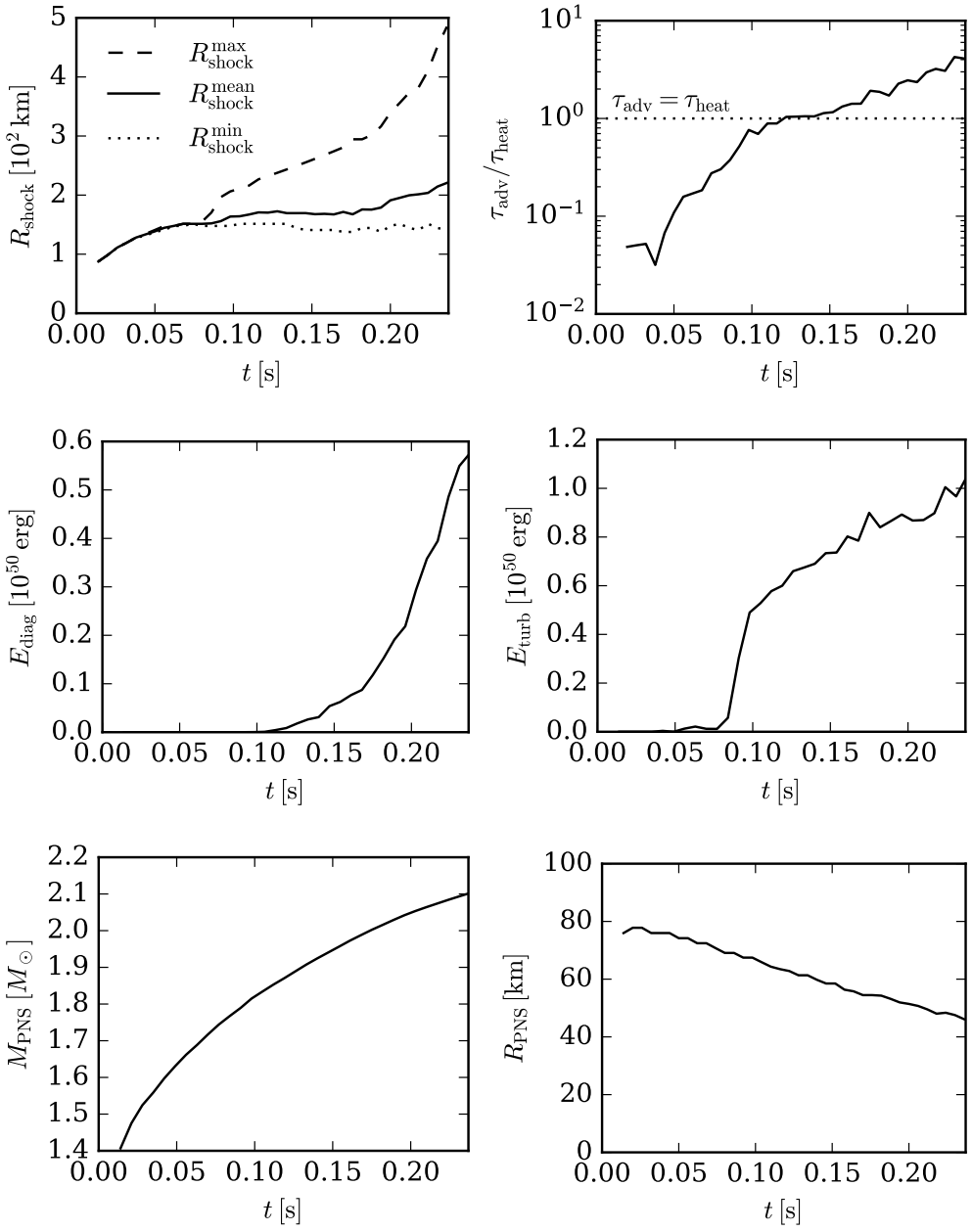

Figure 7.2: Top left panel shows the maximum (dashed), average (solid), and minimum (dotted) position of the shock. Top right panel displays the ratio of advection over heating timescales in the gain layer. Middle panels show the diagnostic (left) and turbulent (right) energy. In the bottom panels, we depict PNS mass (left) and radius (right) evolution. All panels show the evolution from the time of starting the 3D run, i.e., $t = 16\,\mathrm{ms}$

$\langle R_{\rm shock}\rangle$ is the angle averaged shock radius, $\langle R_{\rm gain}\rangle$ the angle averaged gain radius, and $\langle v_{\rm r}^{\rm gain}\rangle$ is the mean radial velocity in the gain region.

As we show in Figure 7.2, $\tau_{\rm adv}/\tau_{\rm heat} > 1$ short after $t = 100\,{\rm ms}$. At this point, the diagnostic explosion energy $E_{\rm diag}$ start to increase, and the maximum shock radius expands linearly. At the end of the simulation, $E_{\rm diag}$ and $R_{\rm shock}^{\rm max}$ are growing rapidly. The former reaches $E_{\rm diag} \simeq 0.55 \cdot 10^{50}\,{\rm erg}$, which is $25 - 50\%$ of the typical explosion energies obtained in 3D models (e.g., Burrows et al., 2020). The maximum shock radius, at the end of the simulation, is pretty developed and achieves $R_{\rm shock}^{\rm max} \simeq 500\,{\rm km}$. Thus, the evolution of all of these quantities suggest that 3D_s24_RN16 will produce a successful explosion. Obviously, the accretion into the PNS, which is rapidly contracting, is still large due to the very early stage of the event. Hence, despite the hints that make us suspect that this model will explode, it is precipitate to make a strong prediction yet. In the following, we have a closer look at the morphology evolution of the model. As we show below, it is consistent with a likely successful explosion.

In Figures 7.3 and 7.4, we highlight the evolution of the flow in the post-shock region of the model, which has a very standard CCSNe characteristics that many works have described in the literature (e.g., Müller et al., 2012). During the first $t \sim 80\,{\rm ms}$ the shape of the shock is quasi-spherical and the shock is stalled. The neutrino heating produces an entropy gradient that produces a convective layer between the PNS and the shock (e.g., Burrows & Vartanyan, 2021; Bollig et al., 2021), as the formation of plumes indicate (e.g., Murphy et al., 2013).

The post-shocked region is mostly convective up to $t \sim 80 - 100\,{\rm ms}$, when we observe the development of large buoyant plumes due to the strong neutrino heating, which present a relatively high entropy of $s \sim 14\,{\rm k_B\,baryon^{-1}}$, that start to dominate the maximum expansion of the shock, and triggers a large deformation. The growth of such big buoyant plumes is especially of interest, since 3D models are less favorable to form them due to the aforementioned energy cascade (Janka et al., 2016). Nevertheless, it is consistent with results obtained in the literature (e.g., Murphy et al., 2013; Couch & O'Connor, 2014). Simultaneously, turbulence starts to play an important role in reviving the shock (Burrows et al., 1995; Dolence et al., 2013; Couch & Ott, 2015, e.g.,). In Figure 7.2, we show the evolution of the kinetic turbulent energy of the flow. We employ Couch & Ott (2015) to compute it in the gain region:

$$E_{\rm turb} = \int_{\rm gain} \frac{1}{2}\rho[(v_r - \langle v_r\rangle)^2 + v_\theta^2 + v_\phi^2], \tag{7.2}$$

where v_r, v_θ, and v_ϕ are the three components of the velocity, and $\langle v_r\rangle$ is the angle averaged radial velocity. Note that $E_{\rm turb}$ gives information about how disordered the flow is, and it is not a diagnostic of the explosion. The turbulent motion adds an extra pressure that drives the shock further outwards, reducing the ram pressure on it. Furthermore, the turbulence causes the matter to follow non-radial trajectories, and thus it is exposed to neutrino heating for longer times. We demonstrate this effect

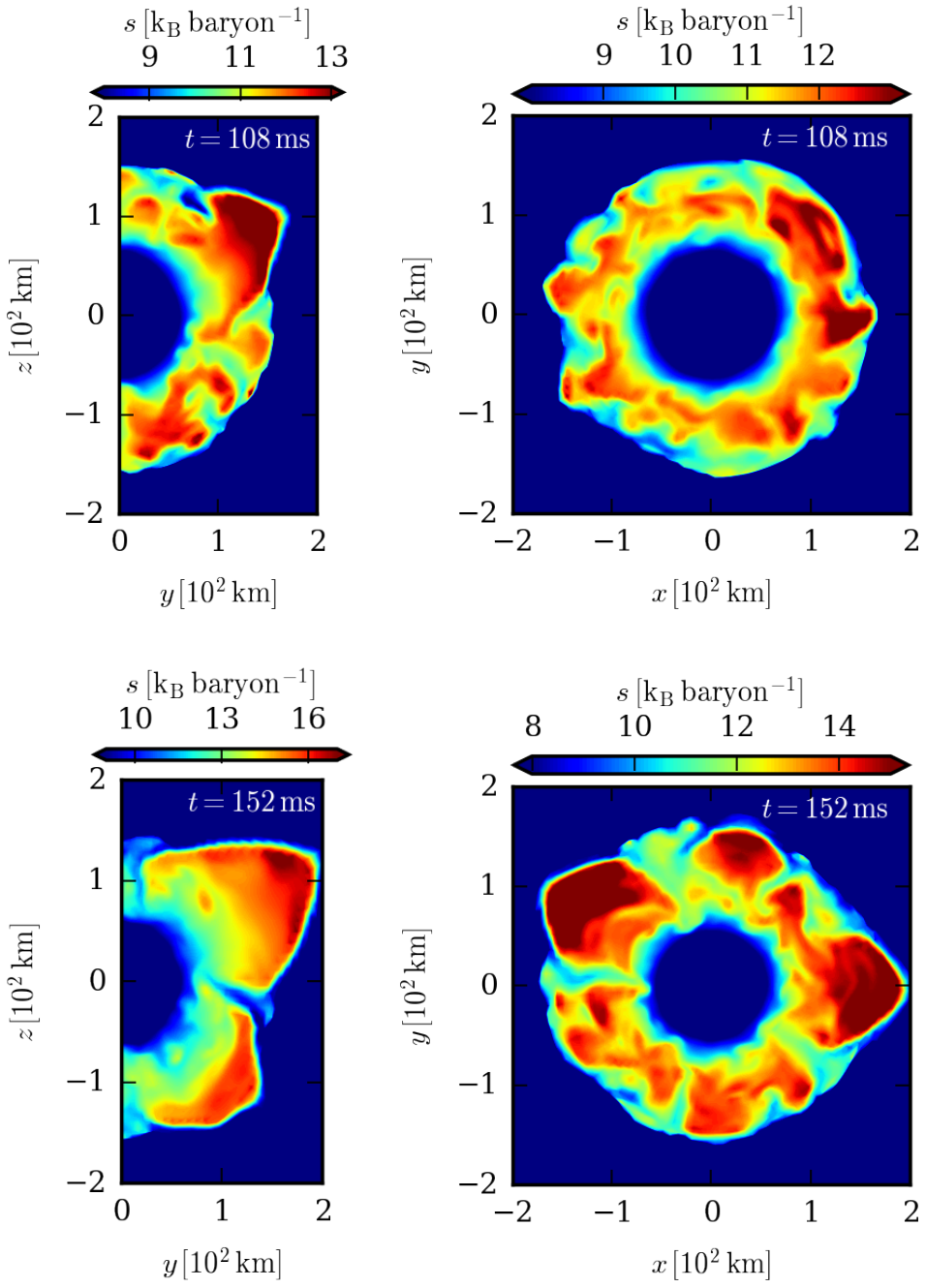

Figure 7.3: Snapshots at $x = 0$ (left) and $z = 0$ (right) of the entropy at displayed times.

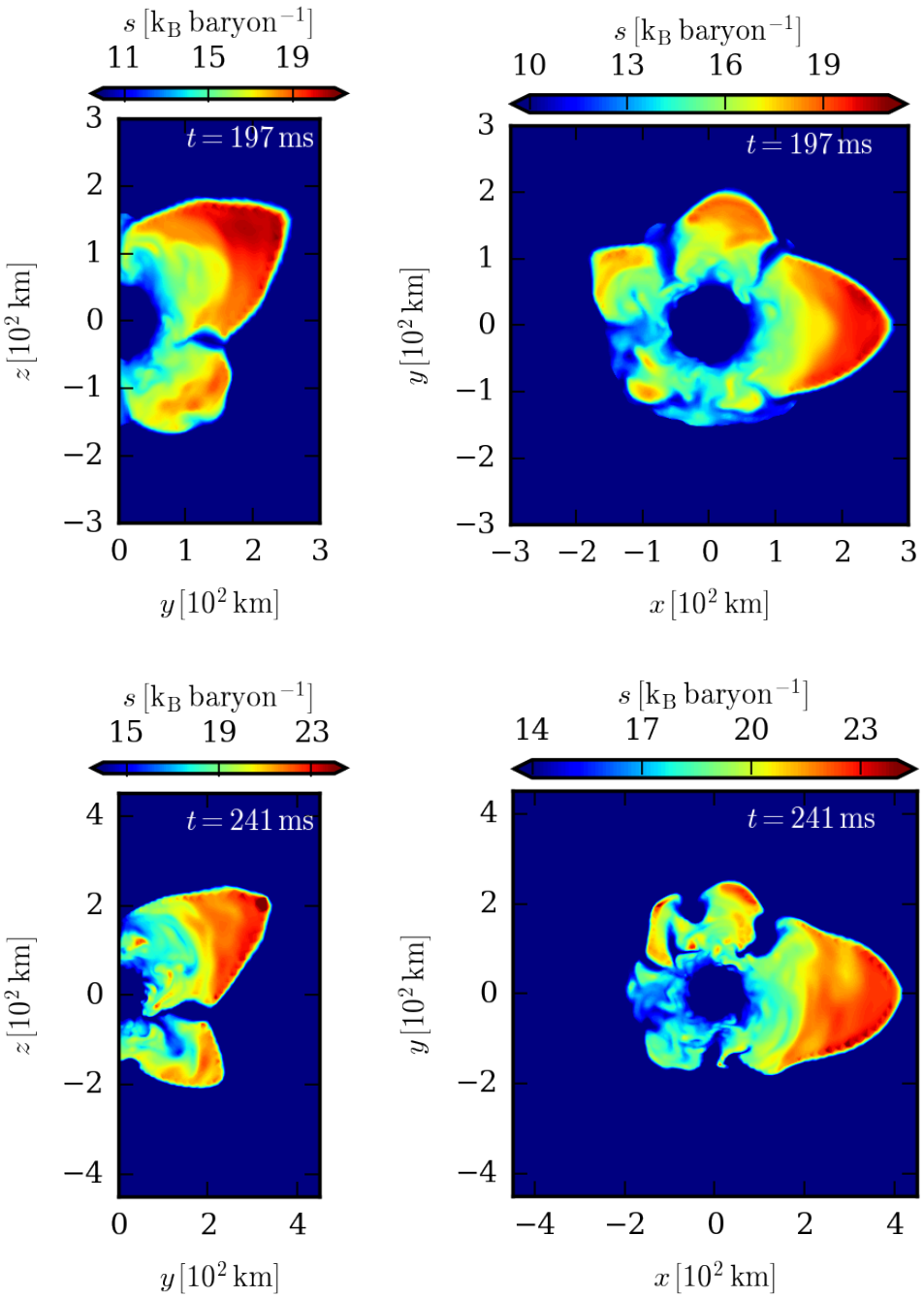

Figure 7.4: Snapshots at $x = 0$ (left) and $z = 0$ (right) of the entropy at displayed times.

by comparing the evolution of $E_{\rm turb}$ and $\tau_{\rm adv}/\tau_{\rm heat}$ in Figure 7.2. The presence of turbulence in the flow significantly increases at $t \sim 80\,{\rm ms}$, and favors the timescale of the heating to be shorter than the advection timescale. The increased time that matter experiences neutrino heating plays an important role for the development of the aforementioned big high-entropy plumes.

The plumes expand and deviate the infalling matter that is not normal to the shock towards regions where the shock is weaker, in low-entropy accretion streams (e.g., Bruenn et al., 2006; Lentz et al., 2015). The growth of the plumes drives these downflows towards more lateral directions with respect to their radial expansion, which generally prevents them from stalling. Thus, the maximum position of the shock is pushed outwards, being even more asymmetric, and increasing the amount of mass in the gain layer that eventually gets unbound, which causes $E_{\rm diag}$ to rapidly increase. Comparing the snapshots at $t \sim 197\,{\rm ms}$ and $t \sim 241\,{\rm ms}$, we notice how several big plumes eventually dissipate into smaller structures due to the already mentioned direct energy cascade. They turn into a convective, turbulent region (see bottom-left area of the $x-y$ plane in the bottom right panel in Figure 7.4), that well-mixes heterogeneous matter with different Y_e. This is well depicted in Figure 7.5, where we show volume renderings of the entropy and electron fraction at $t \sim 241\,{\rm ms}$. Very similarly to Lentz et al. (2015), the two large plumes present in 3D_s24_RN16 will likely drive shock revival.

Interestingly, the high-entropy plumes show proton-rich conditions. In Figure 7.6 we show the evolution of the Y_e and the entropy of the unbound material. Initially, the post-shock region is mainly neutron-rich due to electron captures during the collapse, with $Y_e \sim 0.35 - 0.4$. This favours positron captures and neutrino absorption on free neutrons (e.g., Perego et al., 2014), which cause Y_e to increase. The luminosity of electron neutrinos and antineutrinos is similar, and $\varepsilon_{\bar{\nu}_e} - \varepsilon_{\nu_e} < 5\,{\rm MeV}$, which increases the Y_e (see Equation (2.11)). Furthermore, the neutrino-heating increases the entropy of the material. The large high-entropy plumes that we observe at the end of the simulation experienced an extreme example of this process. They are born in neutron-rich conditions ($Y_e \sim 0.4$). The turbulent nature of the flow makes the region stay longer under a strong neutrino heating, that sets a high entropy in comparison to the surrounding material, $s \sim 14\,{\rm k_B\,baryon^{-1}}$. Then, the plumes expand outwards while strong electron neutrino absorption on free neutrons increase their entropy, up to $s \sim 25\,{\rm k_B\,baryon^{-1}}$, and their Y_e, ending up with $Y_e \sim 0.55$. Finally, the tail of low-entropy and $Y_e \sim 0.5$ matter that we observe in Figure 7.6 corresponds to the matter that has been accreted by the shock. Overall, at $t = 241\,{\rm ms}$, the neutrino-heated unbound material presents $Y_e \gtrsim 0.45$ (e.g., Arcones & Thielemann, 2023; Wanajo, 2023).

The nuclear energy generation in the accreted progenitor layers is not very dynamically relevant yet. The spherical symmetry from the 1D progenitor is mainly preserved, with the exception of a small region in the Fe-rich shell that experiences some mixing (see left panel of Figure 7.7). In this model, we are interested in the

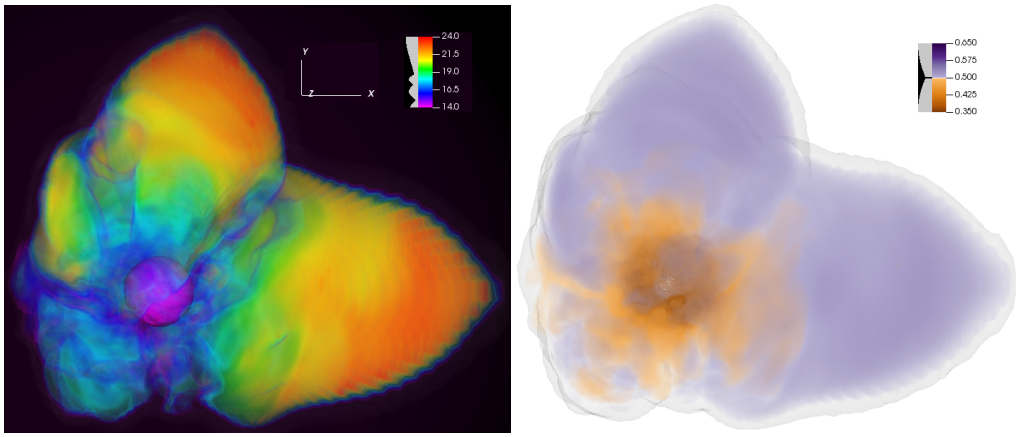

Figure 7.5: Volume rendering of entropy (left) and electron fraction (right) at the end of the simulation, i.e., $t = 241\,\mathrm{ms}$. Neutron-rich conditions are depicted in brown, and proton-rich in blue. Grey contour shows the shock.

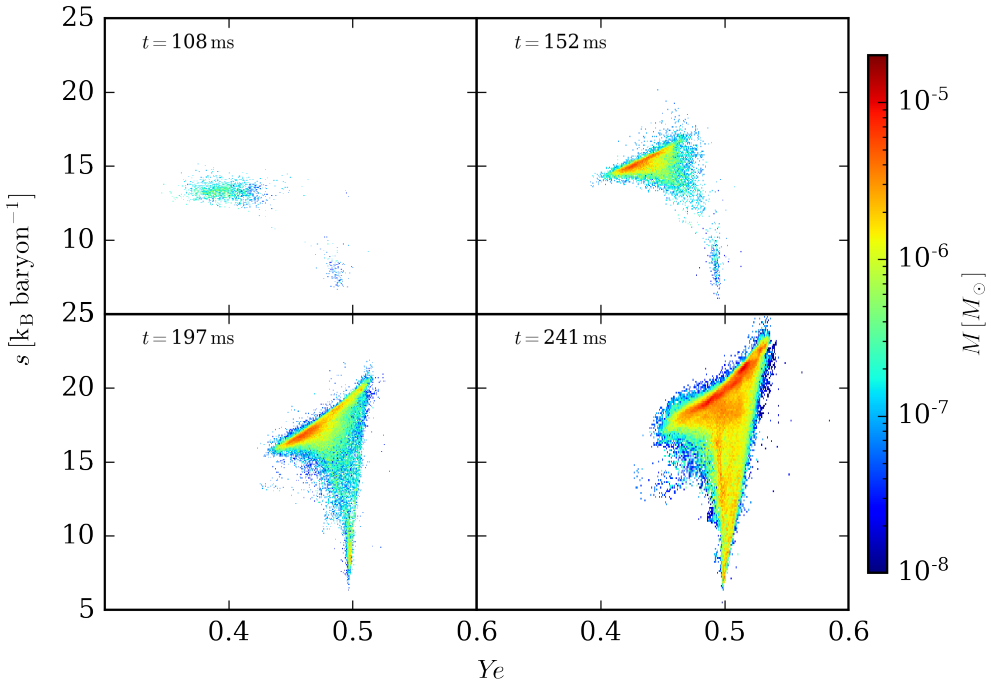

Figure 7.6: Evolution of entropy and electron fraction of unbound matter at $t = 108$, 152, 197, and 241 ms.

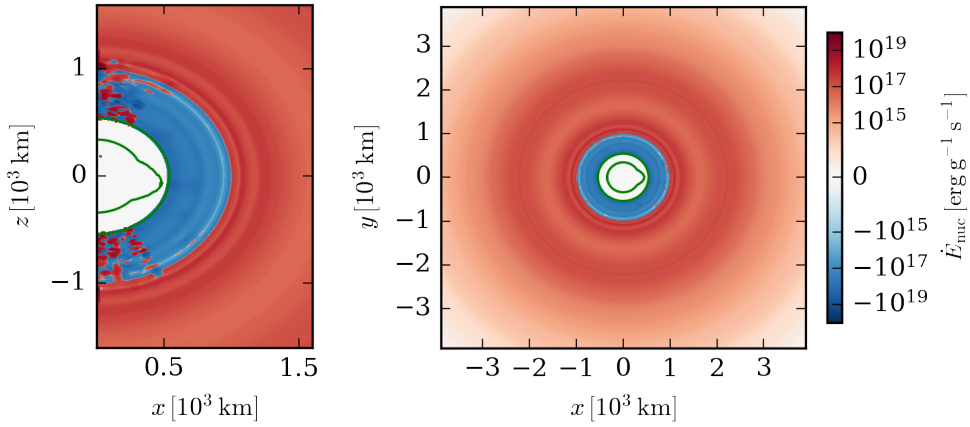

Figure 7.7: Snapshot of the nuclear energy generation at the end of the simulation, $t = 241\,\mathrm{ms}$. Left panel shows the $y = 0$ plane and right panel $z = 0$. Green contours correspond to $T_{\mathrm{th}} = 5.8\,\mathrm{GK}$ and $T_{\mathrm{inter}} = 5.0\,\mathrm{GK}$. The former is deformed by the shock.

impact the accreted heated progenitor shells have on the shock expansion. We expect, accordingly to Chapter 5, that the ram pressure on the shock is reduced and facilitates the expansion. In a future work, it will be interesting to study the effects of following a detailed composition with RN94 from a 3D progenitor. Several works have computed the last minutes of burning in the Si-O shells (e.g., Müller et al., 2017; Fields & Couch, 2021; Yoshida et al., 2021; Vartanyan et al., 2021). They have shown that convective burning in these shells sets in Rayleigh-Taylor instabilities that produce extra turbulence in the shock when they are accreted (e.g., Kifonidis et al., 2003), and, hence, also add deformations to the shock and favour its revival. However, only in Sandoval et al. (2021) the composition is evolved in a detailed manner in 3D simulations, but employing 1D progenitors.

Finally, at the end of the simulation, i.e., $t = 241\,\mathrm{ms}$, the shock is hot and, therefore, the post-shock region is still in NSE. Thus, unfortunately, we have not had the opportunity yet to follow the composition in the shocked region with the network, nor to study the impact of the nuclear energy generation in the shocked material. When the simulation reaches longer times, we will be able track the spatial distribution of ^{56}Ni and ^{44}Ti, and to study the effects of the nuclear energy generation released in the explosive nucleosynthesis.

8 Summary and Outlook

CCSN events span a large variety of thermodynamic conditions, from cold low-density regions in the accreted O- and Si-rich layers ($T \sim 2\,\mathrm{GK}$, $\rho \sim 10^5\,\mathrm{g\,cm^{-3}}$) to the hot and very dense PNS ($T \sim 400\,\mathrm{GK}$, $\rho \sim 10^{14}\,\mathrm{g\,cm^{-3}}$). In this thesis, we explored the impact of micro-physics in both density-temperature regimes.

In the first part, we had a closer look at the low-density and temperature regime, and studied the impact of the composition on the dynamics of the explosion and the nucleosynthesis (Navó et al., 2023). We implemented the nuclear reaction network ReNet (Reichert, 2016) in the state-of-the-art neutrino-hydrodynamics code Aenus-Alcar (Just et al., 2015; Obergaulinger & Aloy, 2017). This is an improvement with respect to the previously included adaptation of the approximate flashing scheme (Rampp & Janka, 2002), which only considers neutrons, protons, and a characteristic nucleus. We considered two reduced networks: a 16 α-chain (RN16) and a larger one that evolved 94 species and considered 148 in steady-state approximation (RN94). The latter, is the most extended nuclear network in the nuclear chart ever employed in a state-of-the-art, multi-dimensional, CCSN simulation, and is able to evolve the composition of the main species synthesized in the event (Navó et al., 2023).

Dealing with the transition between NSE and non-NSE regime was very delicate, since we had to deal with the interface that divided the two EOS regimes and the interface between NSE and the network. While the former considered a density criterion, the latter employed a temperature threshold. This led to undesired numerical artifacts and instabilities in the interfaces. In order to guarantee consistency and continuity across them, we unified the criteria and consider a high-density and temperature regime, where NSE is employed, and a low-density and temperature regime, in which the Helmholtz EOS is used together with the network. Finally, we apply a linear interpolation on the internal energy between the high-density EOS and the Helmholtz to ensure a smooth transition.

We performed a total of 13 one-dimensional and 3 two-dimensional simulations and conducted a systematic study. We showed that a variation of composition treatment leads to a different production of free nucleons that change the neutrino absorption in the vicinity of the shock, and modify the ram pressure outside of it. We also demonstrated the impact of the nuclear energy generation on the dynamics of the explosion. In the accreted progenitor mass shells, this heating term decreases the ram pressure of the shock, and allows it to expand easier, in agreement with Bruenn et al. (2006); Nakamura et al. (2014). In the post-shock region, the nuclear energy

released contributes significantly to the explosion energy, increasing it up to a 20%. The differences between RN16 and RN94 are small regarding the nuclear energy generation, since the reactions that mostly contribute to it are included in both networks. In addition, we showed how these effects on the dynamics impact on the nucleosynthesis. First, we compared the final composition by applying the full-network WinNet (Reichert et al., 2023) in post-processing. The significant amount of nuclear energy released in the post-shock region helps to sustain late outflows, and allow for weak r-process production. Finally, we have shown the strengths and weaknesses of evolving the composition in-situ or in post-processing with Lagrangian tracer particles, by comparing the results obtained in-situ and ex-situ with the same network. In agreement with Harris et al. (2017), we found large discrepancies in the alpha-rich freeze out products, since Lagrangian tracer particles are more uncertain when tracking low density regions. In contrast, the latter are more efficient to track high-density regions (Price & Federrath, 2010), and avoid the excess of numerical diffusion that Eulerian codes need to ensure stability (Plewa & Müller, 1999). The intrinsic differences between both methods lead to different nucleosynthesis paths that impact on the final composition of the ejecta. Thus, we concluded that employing large in-situ nuclear networks, with a less diffussive numerical scheme, are necessary to obtain a more realistic feedback of the energy generation, the neutrino absorption, and a more accurate nucleosynthesis.

At high densities, we explored the impact of different nuclear matter properties on the explosion. We performed 11 one-dimensional simulations where the explosion was artificially triggered with a heating factor. We fixed the set up for all of them and only varied the EOS of dense matter. We employed the EOSs from Huth et al. (2021), who introduced a new EDF, and performed a systematic study of the effects of the slope parameter L, the symmetry energy E_{sym}, the incompressibility K, and the density exponent of the EDF. In agreement with the literature (e.g., Sumiyoshi et al., 2005; Marek et al., 2009), models that show a lower pressure per density lead to a faster collapse and higher central densities at bounce. In addition, they show a faster R_{PNS} contraction that produces faster shock revivals and more compact remnants.

The effects of the slope parameter L are consistent with the fact that the pressure follows its hierarchy, i.e., higher pressures for higher L. Therefore, the models that present a smaller L lead to a faster contraction of the PNS and to a more energetic explosion. In addition, the Y_e also follows the L hierarchy, since the difference between the energy per particle of PNM and SNM increases and, therefore, the system needs to invest more energy to become more asymmetric. In contrast to previous works (e.g., Swesty et al., 1994; Thompson et al., 2003), our preliminary results suggest that the incompressibility K has a significant impact on the dynamics of the explosion. The model that considered a substantially lower K produced the fastest collapse and the highest central densities. This led to a less dense gain region and, thus, to lower pressures below the shock that were not able to push the shock outwards, resulting in a failed shock revival.

In a next step, we plan to study the effects of the variation in the effective mass m^* with its new parametrization (Carbone & Schwenk, 2019). Our results show notable differences between 1D_LS220 and the other models because of their distinct m^* parametrization. As demonstrated by Schneider et al. (2017); Yasin et al. (2020), the thermal contribution to the EOS are included in m^*, and have a dominant impact in the PNS contraction.

Finally, we showed the first $241\,\mathrm{ms}$ of a 3D CCSN simulation that includes RN16 and, therefore, takes into account the main reactions responsible for the nuclear energy generation. We employ the $24\,M_\odot$ from Woosley et al. (2002), since it is susceptible to produce an especially energetic explosion (Jost, 2022). We consider no rotation and neglect the effect of magnetic fields. We plan to evolve the first $1\,\mathrm{s}$ in order to perform a realistic model to provide a benchmark for systematic studies employing cheaper one- and two-dimensional simulations. Our results are consistent with numerous works in the literature (e.g., Müller et al., 2012; Murphy et al., 2013; Couch & O'Connor, 2014; Lentz et al., 2015), and show that the model will likely produce an explosion. The first $\sim 80\mathrm{ms}$, the shock is stalled and quasi-spherical. The post-shock region is mainly convective due to the negative entropy gradient caused by the neutrino heating. After that, the flow becomes more turbulent, i.e., follows non-radial trajectories, and, hence, matter is exposed to neutrinos longer times. This leads large relatively high-entropy plumes to develop and that expand outwards. At the end of the simulation, two large plumes have become very prominent, dominate shock expansion, and are likely triggering the explosion (e.g., Lentz et al., 2015).

We are eager to study the effects of the nuclear energy generation in 3D. We expect that the shock will be affected by the nuclear energy generation in a similar way as our results in 1D and 2D predict. In addition, evolving the composition in the accreted progenitor layers allows us to take into account mixing effects and perturbations that can provide extra deformations to the shock when they are accreted (e.g., Kifonidis et al., 2003). Actually, our results already showed the formation of some anisotropies in the accreted Fe-rich layer. At longer times, we will be able to track the spatial distribution of ^{56}Ni and ^{44}Ti (as in e.g., Stockinger et al., 2020; Sandoval et al., 2021), which is key for observations.

For the future, we have already scheduled a 3D simulation with the RN94. The computational costs of this model are very high, but the simulation will evolve the composition with an unprecedented accuracy in a self-consistent 3D model with state-of-the-art neutrino transport, which is important for a consistent nucleosynthesis. In order to provide an even more consistent model, it will be very interesting to employ a 3D progenitor that includes the last minutes of the O-Si convective burning (e.g., Müller et al., 2017; Fields & Couch, 2021; Yoshida et al., 2021; Vartanyan et al., 2021).

As stated many times in this thesis, the CCSN puzzle is still far from being completed. Nevertheless, an upcoming galactic event will trigger a multi-messenger signal that will provide powerful additional constraints to many open questions such as, e.g,

neutrino properties, the EOS of dense matter, explosion energy, nucleosynthesis, etc. Moreover, the development of exascale computing facilities and improvements in the physics and numerics of the models will entail a breakthrough for the production of a large amount and more accurate 3D CCSN models that will bring us the opportunity to study the mechanisms involved in the explosion and the nucleosynthesis with an unprecedented accuracy.

Bibliography

Abbott, B., Abbott, R., Abbott, T., et al. 2016, PhRvD, 94

—. 2017, PhRvL, 119

Abbott, B. P., Abbott, R., Abbott, T. D., et al. 2020, PhRvD, 101, 084002

Abbott, B. P., Abbott, R., Abbott, T. D., et al. 2020, ApJL, 892, L3

Abdikamalov, E., Pagliaroli, G., & Radice, D. 2021, in Handbook of Gravitational Wave Astronomy (Springer Singapore), 1–37

Abe, K., Adrich, P., Aihara, H., et al. 2021, ApJ, 916, 15

Abi, B., Acciarri, R., Acero, M. A., et al. 2021, EPJC, 81

Alekseev, E. N., Alekseeva, L. N., Volchenko, V. I., & Krivosheina, I. V. 1987, JETPL, 45, 589

Anderson, E., Bai, Z., Bischof, C., et al. 1999, LAPACK Users' Guide, 3rd edn. (Philadelphia, PA: Society for Industrial and Applied Mathematics)

Antoniadis, J., Freire, P. C. C., Wex, N., et al. 2013, Sci, 340, 1233232

Arcones, A., & Bliss, J. 2014, JPhG, 41, 044005

Arcones, A., Martí nez-Pinedo, G., Roberts, L. F., & Woosley, S. E. 2010, A&A, 522, A25

Arcones, A., & Thielemann, F.-K. 2012, JPhG, 40, 013201

—. 2023, A&A Rv, 31, 1

Arnett, W. D. 1980, ApJ, 237, 541

Arnett, W. D., Bahcall, J. N., Kirshner, R. P., & Woosley, S. E. 1989, ARA&A, 27, 629

Baade, W., & Zwicky, F. 1934, PhRv, 46, 76

Baiotti, L. 2019, PrPNP, 109, 103714

Balasi, K., Langanke, K., & Martínez-Pinedo, G. 2015, PrPNP, 85, 33

Barbarino, C., Dall'Ora, M., Botticella, M. T., et al. 2015, MNRAS, 448, 2312

Barker, B. L., Harris, C. E., Warren, M. L., O'Connor, E. P., & Couch, S. M. 2022, ApJ, 934, 67

Baym, G., & Pethick, C. 1991, Landau Fermi-Liquid Theory, Wiley

Bethe, H., Brown, G., Applegate, J., & Lattimer, J. 1979, NuPhA, 324, 487

Bethe, H. A., & Wilson, J. R. 1985a, ApJ, 295, 14

—. 1985b, ApJ, 295, 14

Bionta, R. M., Blewitt, G., Bratton, C. B., et al. 1987, PhRvL, 58, 1494

Bliss, J., Arcones, A., Montes, F., & Pereira, J. 2020, PhRvC, 101, 055807

Bliss, J., Arcones, A., & Qian, Y.-Z. 2018, ApJ, 866, 105

Blondin, J. M., & Mezzacappa, A. 2007, Nature, 445, 58

Blondin, J. M., Mezzacappa, A., & DeMarino, C. 2003, ApJ, 584, 971

Bollig, R., Yadav, N., Kresse, D., et al. 2021, ApJ, 915, 28

Bruenn, S. W. 1985, ApJS, 58, 771

Bruenn, S. W., Dirk, C. J., Mezzacappa, A., et al. 2006, in JPhCS, Vol. 46, 393–402

Bruenn, S. W., Lentz, E. J., Hix, W. R., et al. 2016, ApJ, 818, 123

Bruenn, S. W., Blondin, J. M., Hix, W. R., et al. 2020, ApJS, 248, 11

Bugli, M., Guilet, J., & Obergaulinger, M. 2021, MNRAS, 507, 443

Burbidge, E. M., Burbidge, G. R., Fowler, W. A., & Hoyle, F. 1957, RvMP, 29, 547

Burrows, A. 1990, ARNPS, 40, 181

Burrows, A., & Goshy, J. 1993, ApJL, 416, L75

Burrows, A., Hayes, J., & Fryxell, B. A. 1995, ApJ, 450, 830

Burrows, A., Radice, D., Vartanyan, D., et al. 2020, MNRAS, 491, 2715

Burrows, A., & Vartanyan, D. 2021, Nature, 589, 29

Butcher, J. C. 2003, Numerical Differential Equation Methods (John Wiley & Sons, Ltd), 45–121

Carbone, A., & Schwenk, A. 2019, PhRvC, 100, 025805

Carroll, B. W., & Ostlie, D. A. 2007, An Introduction to Modern Astrophysics, 2nd edn., ed. S. F. P. Addison-Wesley

Cernohorsky, J., & Bludman, S. A. 1994, ApJ, 433, 250

Cernohorsky, J., & van Weert, C. G. 1992, ApJ, 398, 190

Chadwick, J. 1932, Nature, 129, 312

Clark, D. H., & Stephenson, F. R. 1982, in NATO ASIC, Vol. 90, Supernovae: A Survey of Current Research, ed. M. J. Rees & R. J. Stoneham, 355–370

Clayton, D. 1968, Principles of stellar evolution and nucleosynthesis: with a new preface (University of Chicago Press)

Colgate, S. A., Grasberger, W. H., & White, R. H. 1961, AJ, 66, 280

Colgate, S. A., & Johnson, M. H. 1960, PhRvL, 5, 235

Colgate, S. A., & White, R. H. 1966, ApJ, 143, 626

Constantinou, C., Muccioli, B., Prakash, M., & Lattimer, J. M. 2015a, PhRvC, 92, 025801

—. 2015b, PhRvC, 92, 025801

Couch, S. M. 2013, ApJ, 775, 35

—. 2017, PTRSLA, 375, 20160271

Couch, S. M., Chatzopoulos, E., Arnett, W. D., & Timmes, F. X. 2015, ApJL, 808, L21

Couch, S. M., & O'Connor, E. P. 2014, ApJ, 785, 123

Couch, S. M., & Ott, C. D. 2015, ApJ, 799, 5

Couch, S. M., Warren, M. L., & O'Connor, E. P. 2020, ApJ, 890, 127

Courant, R., Friedrichs, K., & Lewy, H. 1928, Math. Ann., 100, 32

Cromartie, H. T., Fonseca, E., Ransom, S. M., et al. 2019, NatAs, 4, 72

Curtis, S., Ebinger, K., Fröhlich, C., et al. 2019, ApJ, 870, 2

Curtis, S., Wolfe, N., Fröhlich, C., et al. 2021, ApJ, 921, 143

Dickhoff, W., & Barbieri, C. 2004, PrPNP, 52, 377

Dolence, J. C., Burrows, A., Murphy, J. W., & Nordhaus, J. 2013, ApJ, 765, 110

Drischler, C., Holt, J., & Wellenhofer, C. 2021, ARNPS, 71, 403

Dubroca, B., & Feugeas, J. 1999, CRASM, 329, 915

Duncan, R. C., Shapiro, S. L., & Wasserman, I. 1986, ApJ, 309, 141

Eichler, M., Sayar, W., Arcones, A., & Rauscher, T. 2019, ApJ, 879, 47

Eichler, M., Nakamura, K., Takiwaki, T., et al. 2017, JPhG, 45, 014001

Fabian, A. C., Willingale, R., Pye, J. P., Murray, S. S., & Fabbiano, G. 1980, MNRAS, 193, 175

Fields, C. E., & Couch, S. M. 2021, ApJ, 921, 28

Freiburghaus, C., Rembges, J. F., Rauscher, T., et al. 1999, ApJ, 516, 381

Fröhlich, C., Martí nez-Pinedo, G., Liebendörfer, M., et al. 2006, PhRvL, 96

Gamow, G. 1930, PRSLSA, 126, 632

Gezerlis, A., & Carlson, J. 2010, PhRvC, 81, 025803

Godunov, S. K. 1959, Mat. Sb., 47(89), 271

Hanke, F., Marek, A., Müller, B., & Janka, H.-T. 2012, ApJ, 755, 138

Harris, J. A., Hix, W. R., Chertkow, M. A., et al. 2017, ApJ, 843, 2

Harten, A., Lax, P. D., & Leer, B. v. 1983, SIAMRv, 25, 35

Hebeler, K., Lattimer, J. M., Pethick, C. J., & Schwenk, A. 2013, ApJ, 773, 11

Hempel, M., Fischer, T., Schaffner-Bielich, J., & Liebendörfer, M. 2012, ApJ, 748, 70

Herant, M., Benz, W., Hix, W. R., Fryer, C. L., & Colgate, S. A. 1994, ApJ, 435, 339

Hirata, K., Kajita, T., Koshiba, M., et al. 1987, PhRvL, 58, 1490

Hix, W. R., & Meyer, B. S. 2006, NuPhA, 777, 188

Hix, W. R., Parete-Koon, S. T., Freiburghaus, C., & Thielemann, F.-K. 2007, ApJ, 667, 476

Hix, W. R., & Thielemann, F. K. 1999, JCoAM, 109, 321

Huth, S. 2023, PhD thesis, Technische Universität Darmstadt, Darmstadt

Huth, S., Wellenhofer, C., & Schwenk, A. 2021, PhRvC, 103, 025803

Iliadis, C. 2015, Nuclear Physics of Stars, Physics textbook (Wiley)

Jakobus, P., Müller, B., Heger, A., et al. 2023, arXiv e-prints, arXiv:2301.06515

Janka, H.-T. 2012, ARNPS, 62, 407

Janka, H.-T. 2017, Neutrino-Driven Explosions, ed. A. W. Alsabti & P. Murdin (Cham: Springer International Publishing), 1095–1150

Janka, H.-T., Langanke, K., Marek, A., Martínez-Pinedo, G., & Müller, B. 2007, PhR, 442, 38

Janka, H.-T., Melson, T., & Summa, A. 2016, ARNPS, 66, 341

Janka, H. T., & Mueller, E. 1995, ApJL, 448, L109

Janka, H.-T. T. 1991, PhD thesis, Munich University of Technology, Germany

Jost, F. 2022, Master's thesis, Technische Universität Darmstadt

Just, O., Bollig, R., Janka, H.-T., et al. 2018, MNRAS, 481, 4786

Just, O., Goriely, S., Janka, H.-T., Nagataki, S., & Bauswein, A. 2021, MNRAS, 509, 1377

Just, O., Obergaulinger, M., & Janka, H. T. 2015, MNRAS, 453, 3386

Kifonidis, K., Plewa, T., Janka, H. T., & Müller, E. 2003, A&A, 408, 621

Kolmogorov, A. 1941, Akademiia Nauk SSSR Doklady, 30, 301

Korobkin, O., Rosswog, S., Arcones, A., & Winteler, C. 2012, MNRAS, 426, 1940

Kotake, K., & Kuroda, T. 2017, in Handbook of Supernovae, ed. A. W. Alsabti & P. Murdin, 1671

Kraichnan, R. H. 1967, Phys. Fluids, 10, 1417

Kumar, R., Dexheimer, V., Jahan, J., et al. 2023, arXiv e-prints, arXiv:2303.17021

Kuroda, T., Arcones, A., Takiwaki, T., & Kotake, K. 2020, ApJ, 896, 102

Kuroda, T., Fischer, T., Takiwaki, T., & Kotake, K. 2022, ApJ, 924, 38

Kuroda, T., Kotake, K., & Takiwaki, T. 2012, ApJ, 755, 11

Lattimer, J. M., & Swesty, D. F. 1991, NuPhA, 535, 331

Le Fèvre, A., Leifels, Y., Reisdorf, W., Aichelin, J., & Hartnack, C. 2016, NuPhA, 945, 112

Lentz, E. J., Bruenn, S. W., Hix, W. R., et al. 2015, ApJL, 807, L31

Leonhardt, M., Pospiech, M., Schallmo, B., et al. 2020, PhRvL, 125

LeVeque, R. J. 1992, Numerical methods for conservation laws (2. ed.)., Lectures in mathematics (Birkhäuser), 1–214

—. 2002, Finite Volume Methods for Hyperbolic Problems, Cambridge Texts in Applied Mathematics (Cambridge University Press)

Levermore, C. D. 1984, JQSRT, 31, 149

Lim, Y. 2012, PhD thesis, Stony Brook U.

Lindquist, R. W. 1966, AP, 37, 487

Lippuner, J., & Roberts, L. F. 2017, ApJS, 233, 18

MacFadyen, A. I., & Woosley, S. E. 1999, ApJ, 524, 262

Machleidt, R., & Entem, D. 2011, PhR, 503, 1

Marek, A., Dimmelmeier, H., Janka, H. T., Müller, E., & Buras, R. 2006, A&A, 445, 273

Marek, A., Janka, H. T., & Müller, E. 2009, A&A, 496, 475

Martin, D., Perego, A., Arcones, A., et al. 2015, ApJ, 813, 2

Martin, D., Perego, A., Kastaun, W., & Arcones, A. 2018, CQGra, 35, 034001

Martínez-Pinedo, G., Fischer, T., Langanke, K., et al. 2016, Neutrinos and Their Impact on Core-Collapse Supernova Nucleosynthesis, ed. A. W. Alsabti & P. Murdin (Cham: Springer International Publishing), 1–37

Mazurek, T. J., Brown, G. E., & Lattimer, J. M. 1979, ApJ, 229, 713

Mezzacappa, A., Endeve, E., Messer, O. E. B., & Bruenn, S. W. 2020a, LRCA, 6, 4

—. 2020b, LRCA, 6, 4

Miller, M. C., Lamb, F. K., Dittmann, A. J., et al. 2019, ApJ, 887, L24

Minerbo, G. N. 1978, JQSRT, 20, 541

Morozova, V., Piro, A. L., Renzo, M., et al. 2015, ApJ, 814, 63

Mösta, P., Ott, C. D., Radice, D., et al. 2015, Nature, 528, 376

Müller, B. 2020, LRCA, 6, 3

Müller, B., Melson, T., Heger, A., & Janka, H.-T. 2017, MNRAS, 472, 491

Müller, E. 1986, A&A, 162, 103

Müller, E., Janka, H. T., & Wongwathanarat, A. 2012, A&A, 537, A63

Murdin, P., & Murdin, L. 1985, Supernovae (Cambridge University Press)

Murphy, J. W., Dolence, J. C., & Burrows, A. 2013, ApJ, 771, 52

Nagakura, H., Iwakami, W., Furusawa, S., et al. 2018, ApJ, 854, 136

Nakamura, K., Takiwaki, T., & Kotake, K. 2022, MNRAS, 514, 3941

Nakamura, K., Takiwaki, T., Kotake, K., & Nishimura, N. 2014, ApJ, 782, 91

NASA, ESA, CSA, et al. 2023. https://webbtelescope.org/contents/media/images/2023/121/01GWQBBY77MHGFV3M3N63KDCEJ

Navó, G., Reichert, M., Obergaulinger, M., & Arcones, A. 2023, ApJ, 951, 112

Obergaulinger, M., & Aloy, M. Á. 2017, MNRAS, 469, L43

—. 2020, MNRAS, 492, 4613

Obergaulinger, M., Just, O., & Aloy, M. A. 2018, JPhG, 45, 084001

Obergaulinger, M., & Reichert, M. 2023, Nucleosynthesis in Jet-Driven and Jet-Associated Supernovae, ed. I. Tanihata, H. Toki, & T. Kajino, 1–38

O'Connor, E., & Ott, C. D. 2011, ApJ, 730, 70

O'Connor, E. P., & Couch, S. M. 2018, ApJ, 865, 81

Oertel, M., & Providência, C. 2018, AIP Conference Proceedings, 1947, 020007

Oyamatsu, K. 1993, NuPhA, 561, 431

Özel, F., & Freire, P. 2016, ARA&A, 54, 401

Parete-Koon, S., Hix, W., & Thielemann, F. 2008, AAS Meeting Abstracts, 211, 162.10

Paxton, B., Bildsten, L., Dotter, A., et al. 2011, ApJS, 192, 3

Perego, A., Hempel, M., Fröhlich, C., et al. 2015, ApJ, 806, 275

Perego, A., Rosswog, S., Cabezón, R. M., et al. 2014, MNRAS, 443, 3134

Peters, G. J., & Hirschi, R. 2013, The Evolution of High-Mass Stars, ed. T. D. Oswalt & M. A. Barstow (Dordrecht: Springer Netherlands), 447–484

Plewa, T., & Müller, E. 1999, A&A, 342, 179

Pons, J. A., Reddy, S., Prakash, M., Lattimer, J. M., & Miralles, J. A. 1999, ApJ, 513, 780

Price, D. J., & Federrath, C. 2010, MNRAS, 406, 1659

Pruet, J., Hoffman, R. D., Woosley, S. E., Janka, H. T., & Buras, R. 2006, ApJ, 644, 1028

Qian, Y. Z., & Woosley, S. E. 1996, ApJ, 471, 331

Raaijmakers, G., Greif, S. K., Riley, T. E., et al. 2020, ApJ, 893, L21

Rampp, M., & Janka, H. T. 2002, A&A, 396, 361

Rapp, B. E. 2017, in Microfluidics: Modelling, Mechanics and Mathematics, ed. B. E. Rapp, Micro and Nano Technologies (Oxford: Elsevier), 549–593

Rauscher, T., Heger, A., Hoffman, R. D., & Woosley, S. E. 2002, ApJ, 576, 323

Reed, B. T., Fattoyev, F., Horowitz, C., & Piekarewicz, J. 2021, PhRvL, 126

Reichert, M. 2016, Master's thesis, Technische Universität Darmstadt

Reichert, M., Obergaulinger, M., Aloy, M. Á., et al. 2022, MNRAS, 518, 1557

Reichert, M., Obergaulinger, M., Eichler, M., Aloy, M. Á., & Arcones, A. 2021, MNRAS, 501, 5733

Reichert, M., Winteler, C., Korobkin, O., et al. 2023, ApJS, 268, 66

Riley, T. E., Watts, A. L., Bogdanov, S., et al. 2019, ApJ, 887, L21

Ristic, M., Holmbeck, E. M., Wollaeger, R., et al. 2022, arXiv e-prints, arXiv:2206.02273

Roberts, L. F., Ott, C. D., Haas, R., et al. 2016, ApJ, 831, 98

Russotto, P., Gannon, S., Kupny, S., et al. 2016, PhRvC, 94

Ryden, B. 2011, Radiative Gas Dynamics (Lecture notes, Ohio State University). http://www.astronomy.ohio-state.edu/~ryden/ast825/ch1-3.pdf

Sandoval, M. A., Hix, W. R., Messer, O. E. B., Lentz, E. J., & Harris, J. A. 2021, ApJ, 921, 113

Scheck, L., Janka, H.-T., Foglizzo, T., & Kifonidis, K. 2007, A&A, 477, 931

Schneider, A. S., Roberts, L. F., & Ott, C. D. 2017, PhRvC, 96, 065802

Schneider, A. S., Roberts, L. F., Ott, C. D., & O'Connor, E. 2019, PhRvC, 100

Serot, B. D., & Walecka, J. D. 1986, ANuPh., 16, 1

Shen, H., Toki, H., Oyamatsu, K., & Sumiyoshi, K. 1998, NuPhA, 637, 435

Shu, C.-W. 1998, Essentially non-oscillatory and weighted essentially non-oscillatory schemes for hyperbolic conservation laws, ed. A. Quarteroni (Berlin, Heidelberg: Springer Berlin Heidelberg), 325–432

Sieverding, A., Müller, B., & Qian, Y. Z. 2020, ApJ, 904, 163

Sieverding, A., Waldrop, P. G., Harris, J. A., et al. 2023, ApJ, 950, 34

Skyrme, T. 1958, NuPh, 9, 615

Skyrme, T. H. R. 1956, PMag, 1, 1043

Sotani, H., & Sumiyoshi, K. 2019, PhRvD, 100, 083008

Sotani, H., Takiwaki, T., & Togashi, H. 2021, PhRvD, 104, 123009

Steiner, A. W., Hempel, M., & Fischer, T. 2013, ApJ, 774, 17

Stockinger, G., Janka, H.-T., Kresse, D., et al. 2020, MNRAS, 496, 2039

Sugahara, Y., & Toki, H. 1994, NuPhA, 579, 557

Sumiyoshi, K., Yamada, S., Suzuki, H., et al. 2005, ApJ, 629, 922

Summa, A., Hanke, F., Janka, H.-T., et al. 2016, ApJ, 825, 6

Suresh, A., & Huynh, H. 1997, JCoP, 136, 83

Swesty, F. D., Lattimer, J. M., & Myra, E. S. 1994, ApJ, 425, 195

Szalai, T., Zsíros, S., Fox, O. D., Pejcha, O., & Müller, T. 2019, ApJ, 241, 38

Szczepańczyk, M. J., Zheng, Y., Antelis, J. M., et al. 2023, arXiv e-prints, arXiv:2305.16146

Tews, I., Krüger, T., Hebeler, K., & Schwenk, A. 2013, PhRvL, 110, 032504

Thielemann, F.-K., Nomoto, K., & Hashimoto, M.-A. 1996, ApJ, 460, 408

Thompson, T. A., Burrows, A., & Pinto, P. A. 2003, ApJ, 592, 434

Timmes, F. X. 1999, ApJS, 124, 241

Timmes, F. X., & Arnett, D. 1999, ApJS, 125, 277

Timmes, F. X., Hoffman, R. D., & Woosley, S. E. 2000, ApJS, 129, 377

Timmes, F. X., & Swesty, F. D. 2000, ApJS, 126, 501

Torres-Forné, A., Cerdá-Durán, P., Obergaulinger, M., Müller, B., & Font, J. A. 2019, PhRvL, 123, 051102

Varma, V., Müller, B., & Schneider, F. R. N. 2022, MNRAS, 518, 3622

Vartanyan, D., Burrows, A., Radice, D., Skinner, M. A., & Dolence, J. 2018, MNRAS, 477, 3091

Vartanyan, D., Coleman, M. S. B., & Burrows, A. 2021, MNRAS, 510, 4689

Wanajo, S. 2006, ApJ, 647, 1323

Wanajo, S. 2023, arXiv e-prints, arXiv:2303.09442

Wanajo, S., Müller, B., Janka, H.-T., & Heger, A. 2018, ApJ, 852, 40

Wang, T., & Burrows, A. 2023, ApJ, 954, 114

Watts, A. L., Andersson, N., Chakrabarty, D., et al. 2016, RvMP, 88

Weaver, T. A., Zimmerman, G. B., & Woosley, S. E. 1978, ApJ, 225, 1021

Weinberg, D. H. 2007, Radiative Gas Dynamics (Lecture notes, Ohio State University). https://www.astronomy.ohio-state.edu/weinberg.21/A825/a825.html

Winteler, C., Käppeli, R., Perego, A., et al. 2012, ApJL, 750, L22

Witt, M., Psaltis, A., Yasin, H., et al. 2021, ApJ, 921, 19

Witt, M. R. 2020, PhD thesis, Technische Universität Darmstadt, Darmstadt

Wongwathanarat, A., Janka, H.-T., Müller, E., Pllumbi, E., & Wanajo, S. 2017, ApJ, 842, 13

Woosley, S. E. 1993, ApJ, 405, 273

Woosley, S. E., & Heger, A. 2007, PhR, 442, 269

Woosley, S. E., Heger, A., & Weaver, T. A. 2002, RvMP, 74, 1015

Woosley, S. E., & Hoffman, R. D. 1992, ApJ, 395, 202

Woosley, S. E., & Weaver, T. A. 1995, ApJS, 101, 181

Woosley, S. E., Wilson, J. R., Mathews, G. J., Hoffman, R. D., & Meyer, B. S. 1994, ApJ, 433, 229

Yasin, H., Schäfer, S., Arcones, A., & Schwenk, A. 2020, PhRvL, 124, 092701

Yoshida, T., Takiwaki, T., Kotake, K., et al. 2021, ApJ, 908, 44

Yukawa, H. 1935, Proc. Phys. Math. Soc. Jpn., 17, 48

Zampieri, L. 2017, Light Curves of Type II Supernovae, ed. A. W. Alsabti & P. Murdin (Cham: Springer International Publishing), 1–32

Acknowledgements

I would like to thank all people who have supported me during these years. First, thank you Almudena Arcones for believing in me and giving me the opportunity to get into this wonderful topic, for teaching me and supervising me, and for being so supportive during some hard times.

Thank you Miguel Ángel Aloy for agreeing to be my second reviewer. Especial thanks to Martin Obergaulinger, I have learnt a lot from you. Thank you for teaching me so much, introducing me to the code, and for all the time you have spent explaining me things. Thank you Moritz Reichert for lending me your "child" and the many hours invested in me. In addition, I would like to thank my collaborators Sabrina Huth, Finia Jost, Yeunhwan Lim, and Achim Schwenk for all their work and so many discussions. I really learn a lot from you.

This thesis significantly improved thanks to the comments from Almudena, Martin, Moritz, Max, and Finia. Thank you!

I have spent great years in Darmstadt. Thanks to all the people from the group with whom we have shared time, coffees and discussions: Almudena, Federico, Finia, Giacomo, Jan, Marius, Martin, Max(s), Moritz, Takami, and Thanasis. From the beginning, I felt very welcomed, despite the global pandemic. Especial thanks to all good friends I have made here: Daniel, Giacomo, Jorge, Kevin, Max and Tatjana, Moritz, Thanasis, and Uriel. For the great evenings in Ratskeller, the chill nights in Tropical, the table tennis matches, the bike tours, etc. Danke an den SV Blau-Gelb Darmstadt für die Integration von Menschen aus so vielen verschiedenen Ländern in dieser Stadt. Danke an alle meine Mannschaftskameraden für die schönen gemeinsamen Trainings- und Spielabende.

No em voldria oblidar de donar les gràcies a Josep Maria Solanes, Josep Tous, Marc Ribó, Daniel Del Ser i Octavi Fors. Gràcies per donar-me l'oportunitat d'introduir-me en la ciència i per tot el suport durant la cerca d'un doctorat.

Moltes gràcies als meus amics i amigues Dani(s), David, Edu, Estefi, Facu, Ferri, Martí, Nico, Pablo, Paula, Sara i Valen per seguir-me fent sentir com si mai hagués marxat del poble.

Gràcies a tota la meva família. En especial, a la meva tieta Pilar, als meus tiets Josep Maria i Maria Jesús, i al Paco i la Mari Carmen per cuidar de la gent que més estimo. Gràcies als meus cosins Xavi (i Ester), David i Roger (i Laura) per estar a prop meu.

Moltes gràcies Maria per acompanyar-me en aquesta aventura. Brindem per que

siguin moltes més.

Deixo pel final a les persones a qui més agraeixo tot els esforços què han fet per mi desde que vaig néixer i que m'han donat tot. Moltes gràcies papa! Muchas gracias mama!

This work was supported by the Deutsche Forschungsgemeinschaft (DFG, German Research Foundation) - Project-ID 279384907 - SFB 1245 and the European Research Council under grant EUROPIUM-667912. The author gratefully acknowledges the computing time provided by the high-performance computer Lichtenberg at the NHR Centers NHR4CES at TU Darmstadt (Project-IDs 01527 and 01860). This is funded by the Federal Ministry of Education and Research, and the state governments participating.

Curriculum Vitae

Gerard Navó Pérez

2020 – 2023	Doctoral studies and member of the scientific staff, TU Darmstadt, Germany
2018 – 2019	Master's degree in high energy physics, astrophysics, and cosmology, Universitat Autònoma de Barcelona, Spain
2013 – 2018	Bachelor's degree in physics, Universitat de Barcelona, Spain

Erklärungen laut Promotionsordnung

§ 8 Abs. 1 lit. c PromO

Ich versichere hiermit, dass die elektronische Version meiner Dissertation mit der schriftlichen Version übereinstimmt.

§ 8 Abs. 1 lit. d PromO

Ich versichere hiermit, dass zu einem vorherigen Zeitpunkt noch keine Promotion versucht wurde. In diesem Fall sind nähere Angaben über Zeitpunkt, Hochschule, Dissertationsthema und Ergebnis dieses Versuchs mitzuteilen.

§ 9 Abs. 1 PromO

Ich versichere hiermit, dass die vorliegende Dissertation selbstständig und nur unter Verwendung der angegebenen Quellen verfasst wurde.

§ 9 Abs. 2 PromO

Die Arbeit hat bisher noch nicht zu Prüfungszwecken gedient.

Darmstadt, 16. Oktober 2023

G. Navó Perez